August 1989   UILU-ENG-89-2220

COORDINATED SCIENCE LABORATORY
College of Engineering

AD-A211 669

SPECTRAL-DOMAIN ANALYSIS OF FINITE FREQUENCY SELECTIVE SURFACES

Kim Merewether
Raj Mittra

DTIC

UNIVERSITY OF ILLINOIS AT URBANA-CHAMPAIGN

89   9   036

REPORT DOCUMENTATION PAGE

1a. REPORT SECURITY CLASSIFICATION		1b. RESTRICTIVE MARKINGS			
Unclassified		None			
2a. SECURITY CLASSIFICATION AUTHORITY		3. DISTRIBUTION/AVAILABILITY OF REPORT			
		Approved for public release; distribution unlimited			
2b. DECLASSIFICATION/DOWNGRADING SCHEDULE					
4. PERFORMING ORGANIZATION REPORT NUMBER(S)		5. MONITORING ORGANIZATION REPORT NUMBER(S)			
UILU-ENG-89-2220					
6a. NAME OF PERFORMING ORGANIZATION	6b. OFFICE SYMBOL (If applicable)	7a. NAME OF MONITORING ORGANIZATION			
Coordinated Science Lab University of Illinois	N/A	Office of Naval Research			
6c. ADDRESS (City, State, and ZIP Code)		7b. ADDRESS (City, State, and ZIP Code)			
1101 W. Springfield Ave. Urbana, IL 61801		Arlington, VA 22217			
8a. NAME OF FUNDING/SPONSORING ORGANIZATION Joint Services Electronics Program	8b. OFFICE SYMBOL (If applicable)	9. PROCUREMENT INSTRUMENT IDENTIFICATION NUMBER N00014-84-C-0149			
8c. ADDRESS (City, State, and ZIP Code)		10. SOURCE OF FUNDING NUMBERS			
Arlington, VA 22217		PROGRAM ELEMENT NO.	PROJECT NO.	TASK NO.	WORK UNIT ACCESSION NO.

11. TITLE (Include Security Classification)
Spectral-Domain Analysis of Finite Frequency Selective Surfaces

12. PERSONAL AUTHOR(S)
Kim O. Merewether and Raj Mittra

13a. TYPE OF REPORT	13b. TIME COVERED		14. DATE OF REPORT (Year, Month, Day)	15. PAGE COUNT
Technical	FROM _____	TO _____	1989 August	108

16. SUPPLEMENTARY NOTATION

17.	COSATI CODES		18. SUBJECT TERMS (Continue on reverse if necessary and identify by block number)
FIELD	GROUP	SUB-GROUP	Frequency Selective Surfaces (FSS), Truncated FSS, Radar Scattering, Spectral Domain Analysis, Non-Plane Wave Excitation

19. ABSTRACT (Continue on reverse if necessary and identify by block number)

Though frequency selective surfaces have been investigated for over two hundred years, accurate numerical analysis of these surfaces is still in its infancy. Past models assumed that the surface is periodic, infinite in extent, and illuminated by a uniform plane wave. In many practical applications, however, these assumptions may be invalid. In this thesis, the method of moments is applied in the spectral domain to model finite frequency selective surfaces, to study the effects of non-plane-wave sources, and to explore the advantages of gradually adjusting the lattice and shape of the element in a nonuniform frequency selective surface for non-plane-wave excitation.

In pursuing these goals, the following topics are discussed in some detail. First, because of the limited interest in free-standing surfaces, and because the usual cascade approach is not applicable to finite frequency selective surfaces, a general multilayer Green's function is developed in order to incorporate an arbitrary dielectric support. Second, because the analysis of finite arrays

20. DISTRIBUTION/AVAILABILITY OF ABSTRACT			21. ABSTRACT SECURITY CLASSIFICATION		
☒ UNCLASSIFIED/UNLIMITED ☐ SAME AS RPT. ☐ DTIC USERS			Unclassified		
22a. NAME OF RESPONSIBLE INDIVIDUAL			22b. TELEPHONE (Include Area Code)		22c. OFFICE SYMBOL

SECURITY CLASSIFICATION OF THIS PAGE
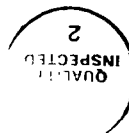
19. Abstract (continued)

can be computationally intensive, several strategies are discussed for efficiently filling the matrices generated by the application of the spectral-domain method of moments. Third, a few methods for handling the singularities of the spectral Green's function are briefly mentioned, including a comparison of several adaptive numerical integration routines for integrating functions which are singular or sharply peaked.

The effects of finite dimensions are evaluated by comparing the induced currents and reflection coefficients for the finite and periodic arrays. The effects can be classified into at least two frequency regimes. At frequencies that are near the first resonant frequency of the element, the edge plays a relatively minor role in influencing the scattered fields. At lower frequencies, however, an edge-to-edge resonance can be excited on the array, which cannot be predicted by periodic models.

SPECTRAL-DOMAIN ANALYSIS
OF FINITE FREQUENCY SELECTIVE SURFACES

by

Kim Merewether and Raj Mittra
Electromagnetic Communication Laboratory
University of Illinois
Urbana, Illinois

ABSTRACT

Though frequency selective surfaces have been investigated for over two hundred years, accurate numerical analysis of these surfaces is still in its infancy. Past models assumed that the surface is periodic, infinite in extent, and illuminated by a uniform plane wave. In many practical applications, however, these assumptions may be invalid. In this thesis, the method of moments is applied in the spectral domain to model finite frequency selective surfaces, to study the effects of non-plane-wave sources, and to explore the advantages of gradually adjusting the lattice and shape of the element in a nonuniform frequency selective surface for non-plane-wave excitation.

In pursuing these goals, the following topics are discussed in some detail. First, because of the limited interest in free-standing surfaces, and because the usual cascade approach is not applicable to finite frequency selective surfaces, a general multilayer Green's function is developed in order to incorporate an arbitrary dielectric support. Second, because the analysis of finite arrays can be computationally intensive, several strategies are discussed for efficiently filling the matrices generated by the application of the spectral-domain method of moments. Third, a few methods for handling the singularities of the spectral Green's func , . are briefly mentioned, including a comparison of several adaptive numerical integration rou   s for integrating functions which are singular or sharply peaked.

The effects of finite dimensions are evaluated by comparing the induced currents and reflection coefficients for the finite and periodic arrays. The effects can be classified into at least two frequency regimes. At frequencies that are near the first resonant frequency of the element, the edge plays a relatively minor role in influencing the scattered fields. At lower frequencies, however, an edge-to-edge resonance can be excited on the array, which cannot be predicted by periodic models.

SPECTRAL-DOMAIN ANALYSIS
OF FINITE FREQUENCY SELECTIVE SURFACES

by

Kim Merewether and Raj Mittra
Electromagnetic Communication Laboratory
University of Illinois
Urbana, Illinois

ABSTRACT

Though frequency selective surfaces have been investigated for over two hundred years, accurate numerical analysis of these surfaces is still in its infancy. Past models assumed that the surface is periodic, infinite in extent, and illuminated by a uniform plane wave. In many practical applications, however, these assumptions may be invalid. In this thesis, the method of moments is applied in the spectral domain to model finite frequency selective surfaces, to study the effects of non-plane-wave sources, and to explore the advantages of gradually adjusting the lattice and shape of the element in a nonuniform frequency selective surface for non-plane-wave excitation.

In pursuing these goals, the following topics are discussed in some detail. First, because of the limited interest in free-standing surfaces, and because the usual cascade approach is not applicable to finite frequency selective surfaces, a general multilayer Green's function is developed in order to incorporate an arbitrary dielectric support. Second, because the analysis of finite arrays can be computationally intensive, several strategies are discussed for efficiently filling the matrices generated by the application of the spectral-domain method of moments. Third, a few methods for handling the singularities of the spectral Green's function are briefly mentioned, including a comparison of several adaptive numerical integration routines for integrating functions which are singular or sharply peaked.

The effects of finite dimensions are evaluated by comparing the induced currents and reflection coefficients for the finite and periodic arrays. The effects can be classified into at least two frequency regimes. At frequencies that are near the first resonant frequency of the element, the edge plays a relatively minor role in influencing the scattered fields. At lower frequencies, however, an edge-to-edge resonance can be excited on the array, which cannot be predicted by periodic models.

TABLE OF CONTENTS

CHAPTER 1

INTRODUCTION

The problem of predicting electromagnetic scattering from periodic structures has been studied for well over a century. As early as 1786, David Rittenhouse, an American physicist, published his experiments on the diffraction of light through a periodic grating [1, 2]. Fraunhofer constructed some of the first practical diffraction gratings in 1823 to split a beam of light into its various colors. At lower frequencies, Hertz utilized a metallic grid in his experiments in 1889. Within a few years, several theoretical papers had appeared attempting to explain Hertz's experiments, the first by J. J. Thompson in 1893 [3]. From that time to the present, the problem has received intermittent attention, driven primarily by the discovery of new applications, the development of printed circuit techniques, and the advent of the high-speed digital computer. The last of these factors has permitted a wide range of complicated geometries to be treated efficiently and accurately using a handful of systematic techniques.

At microwave frequencies, the two-dimensional versions of these surfaces are generated by replicating a conducting patch or aperture in a periodic fashion along two surface coordinates, which may or may not be orthogonal. The shape of the generating patch or aperture is used, to some extent, to control the frequency response of the surface, for example, to increase the bandwidth or to make the frequency response less sensitive to incident angle. Special considerations apply to circular polarization; otherwise, the element shape is arbitrary.

As a function of frequency, electromagnetic scattering from periodic surfaces is characterized by an infinite number of alternating reflection and transmission bands. At

certain frequencies, a periodic array of printed elements can reflect an incident field as though it were a solid perfectly-conducting sheet. At other frequencies, the surface is perfectly transparent. It is this property that is most often used in satellite antenna applications, where a periodic surface is used to generate a second focus for a parabolic reflector. It is also the property that gives it the name frequency selective surface (FSS).

Nearly all of the theoretical analyses of frequency selective surfaces has been based on the assumption that the surface is infinite in extent along both coordinate axes. For plane-wave incidence, the cell currents differ only by the known progressive phase shift of the incident field; thus, the fundamental unknown is either the current density or aperture field on a single unit cell. When frequency selective surfaces are implemented in real systems, they are finite, and due to their different environments, currents flowing in the interior regions of the surface can be quite different from currents flowing near the edges. The goal of this research is to study the effects of truncating a periodic surface to a finite size.

A frequency selective surface that has been truncated to finite dimensions is not periodic. Unless otherwise indicated by the context, the term "periodic surface" will always be used to refer to the infinite planar surface, which is (infinitely) periodic in one dimension (in the case of strip gratings) or two dimensions (in the case of true two-dimensional elements). The term "dichroic surface" will be avoided, since many applications are concerned with more than two frequencies.

This thesis is written from the problem-solver's point of view. Most of the emphasis is on the formulation of the equations and on the considerations that are essential to efficiently and accurately solve those equations on the computer. Less emphasis will be placed on physical interpretation of the results. This thesis is not intended to be a survey of the theory of periodic arrays. A complete discussion of the properties of the Floquet space harmonics, surfaces that are periodic in other separable coordinate systems, the application of Babinet's principle to complementary screens, iterative solutions of the scattering

equations via the conjugate gradient method, and scattering matrices for cascading arbitrary dielectric layers and layers of printed elements are all treated elsewhere and will not be repeated here [2, 4]. The scope of this thesis includes only material that directly pertains to the analysis of finite frequency selective surfaces, or material that is not readily available elsewhere.

The thesis is organized as follows: Chapter 2 introduces the geometries considered in the body of the text, identifies the fundamental unknown in each case, and summarizes the relationships between the fundamental unknowns and the total current density in the plane of the printed surface. Chapter 3 provides a review of the spectral-Galerkin technique, with a detailed look at the derivation of the spectral-domain Green's function for an arbitrary N-layer dielectric medium. Chapter 4 highlights some of the theoretical and numerical considerations that are essential to implementing the spectral-Galerkin equation on the computer. A few representative numerical results are presented in Chapter 5, the response of frequency selective surfaces to arbitrary incident fields, such as the near field of an electromagnetic horn, is the subject of Chapter 6, and Chapter 7 summarizes the main conclusions and suggests directions for future work.

CHAPTER 2

REPRESENTATION OF FUNCTIONS IN PERIODIC AND APERIODIC DOMAINS

A few years ago, the spectral-domain formulation of the method of moments was developed and successfully applied to a number of different problems. Although the connection is not always clear, many of the formulations for predicting electromagnetic scattering from periodic surfaces that directly make use of the fact that the scattered field is composed of a discrete spectrum of plane waves are essentially equivalent to the method presented here. Some of the foundational papers, for example, Montgomery [5], Chen [6], Chen [7], and Tsao and Mittra [8], have very different points of view, terminology, and notation, but they all arrive at the same fundamental equation, and solve it using the same techniques. In the next chapter, we will take a look at the spectral-Galerkin technique as it applies to a fairly broad class of FSS-type problems, but first, in order to avoid repetition, it is necessary to review some basic concepts on representing functions in periodic and aperiodic domains

One of the most useful means of evaluating the effects of truncating a periodic surface is to compare the currents and scattered fields obtained for the finite problem with the corresponding results for the periodic problem. The amount that the two results differ is entirely due to the finite versus infinite character of the two problems. However, in order to assign all of the difference to the truncation effect, it is necessary to solve both problems, the finite problem and the periodic problem, using similar approximations, particularly if one is interested in comparing, for example, the induced currents on the two structures. For this reason, both finite and periodic surfaces will be considered, concentrating more heavily on the finite-FSS problem.

Having stated that the subject of the thesis is electromagnetic scattering from finite frequency selective surfaces, the subject matter is still too broad and varied to allow a comprehensive treatment. The problems considered here have been restricted by the following simplifying assumptions. First, partially due to the fact that the method of solution is a Fourier-transform technique, only planar geometries are considered. The problem of predicting the scattered fields from a frequency selective surface which has true two-dimensional curvature, such as a parabolic dish or hyperbolic subreflector, is still a challenging problem computationally, and one which has only been modeled using crude approximations or by relying heavily on experimental data. Cwik has discussed surfaces which are periodic in cylindrical and spherical coordinate systems [2], and he has also considered finite and periodic strip gratings on the surfaces of infinite cylinders [9]. However, the general problem, for the most part, has not been addressed – nor will it be addressed here.

Second, although the method is not limited to single layers of metallization, for the purposes of this thesis, the geometry considered is a single layer of printed elements embedded in an N-layer dielectric medium, where each layer is assumed to be uniform, homogeneous, and characterized by the complex-valued relative dielectric permittivity ε_r. Under these assumptions, the problems of interest here fall into four or five general categories, which are treated in order of their computational difficulty.

As a corollary to the uniqueness theorem, the fundamental unknown in the integral equation can be chosen as either the induced electric current density on the metallized portions of the surface or as the tangential electric field in the apertures. In the periodic problem, the choice is somewhat arbitrary, but it is usually computationally more convenient to choose as the unknown that quantity that occupies the least physical area. In the finite-array problem, the choice is more clear. In the case in which a finite array of apertures is assumed to exist in an infinite conducting sheet, the idea of representing the current density over the infinite conducting sheet does not seem to be an option. In the

same way, for a surface formed by printing a finite number of conducting patches on an infinite dielectric substrate, choosing the tangential electric field as the fundamental unknown would seem to be impractical, since this too would involve representing the unknown over an infinite area. All of the finite-FSS examples that we will consider are of the second kind, where the metallized region is assumed to be finite in some sense, and hence, the induced current density on the surface will always be taken as the fundamental unknown.

2.1 Periodic Strip Grating

The first two types of problems that are considered are strip gratings [9-12]: infinitely long layers of metallization printed on a dielectric substrate, as shown in Fig. 2.1.
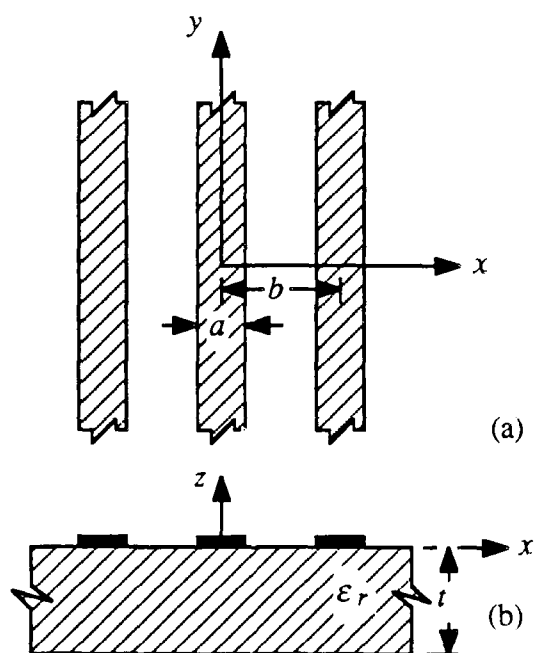

Figure 2.1. Strip grating geometry: (a) top view, (b) side view.

These are one-dimensional structures in the sense that the geometry is independent of one of the surface coordinates. As a result, they are among the simplest structures of any practical interest.

In the first case, we will consider a *periodic* grating, in which a unit strip is replicated in a periodic fashion an infinite number of times in the direction perpendicular to the strips. The metallized areas are assumed to be zero-thickness, perfectly-conducting regions of width a and periodicity b, embedded in N uniform homogeneous dielectric layers, described by complex relative permittivities ε_{r_i} and thicknesses t_i.

In order to determine how this structure scatters an incident electromagnetic field, the objective is to first write an expression for the induced current density on the entire surface in terms of the current on a single element. If the incident field is assumed to be a plane wave incident from the direction (θ_i, φ_i), derived from the magnetic and electric vector potentials $\mathbf{A}$ and $\mathbf{F}$, where

$$\mathbf{A} = \hat{z}\, e^{j(k_x x + k_y y + k_z z)}$$
$$\mathbf{F} = \hat{z}\, e^{j(k_x x + k_y y + k_z z)} \tag{2.1}$$

and,

$$k_x = k_0\, \sin\theta_i\ \cos\phi_i$$
$$k_y = k_0\, \sin\theta_i\ \sin\phi_i \tag{2.2}$$
$$k_z = k_0\, \cos\theta_i \,,$$

then the y variation of the induced surface current will have the same exponential phase dependence as the incident field. Adopting the notation of Papoulis [13], the x and y components of the total induced current density, $J_x(x,y)$ and $J_y(x,y)$, can be written in the form,

$$J_x(x,y) = \left\{ J_{x0}(x) * \sum_{m=-\infty}^{\infty} \delta(x - mb)\, e^{jk_x x} \right\} e^{jk_y y} \,,$$

$$J_y(x,y) = \left\{ J_{y0}(x) * \sum_{m=-\infty}^{\infty} \delta(x - mb)\, e^{jk_x x} \right\} e^{jk_y y} \,, \tag{2.3}$$

or in vector notation,

$$\mathbf{J}(x,y) = \left\{ \mathbf{J}_0(x) * \sum_{m = -\infty}^{\infty} \delta(x - mb)\, e^{jk_x x} \right\} e^{jk_y y} . \tag{2.4}$$

With the y dependence removed, the remainder of the total current density, in braces, is a function of x only. It can therefore be represented as a one-dimensional convolution of $\mathbf{J}_0(x)$, the current density on the center strip along the cut $y = 0$, and an infinite, periodic sequence of delta functions, which are weighted by the progressive phase shift of the incident field.

The representation given by Eqs. (2.3) and (2.4) is not unique. Another possibility would have been to factor out the phase shift due to the incident field in both x and y, leaving a periodic function of x,

$$\mathbf{J}(x,y) = \left\{ \mathbf{J}_0(x) * \sum_{m = -\infty}^{\infty} \delta(x - mb) \right\} e^{jk_x x}\, e^{jk_y y} . \tag{2.5}$$

The difference between the two representations is usually insignificant, but it is possible to imagine situations in which one representation might offer some advantages over the other.

Anticipating the need for the Fourier transform of $\mathbf{J}(x,y)$, which is defined as

$$\tilde{\mathbf{f}}(\alpha,\beta) = \int_{-\infty}^{\infty} \int_{-\infty}^{\infty} \mathbf{f}(x,y)\, e^{-j\alpha x}\, e^{-j\beta y}\, dx\, dy , \tag{2.6}$$

from Eq. (2.4),

$$\tilde{\mathbf{J}}(\alpha,\beta) = \frac{4\pi^2}{b} \tilde{\mathbf{J}}_0(\alpha) \sum_{m = -\infty}^{\infty} \delta(\alpha - \alpha_m)\, \delta(\beta - k_y), \tag{2.7a}$$

$$\alpha_m = \frac{2\pi m}{b} + k_x , \tag{2.7b}$$

where $\tilde{\mathbf{J}}_0(\alpha)$, with a single argument, denotes a Fourier transform with respect to x only, and the tilde "~" is used to denote a Fourier-transformed quantity. Equation (2.7a) illustrates a common feature of all periodic surfaces: when a periodic surface is illuminated

by an incident plane wave, the spectrum of its induced current is discrete. As a consequence, the only scattered fields above and below the surface that satisfy the boundary conditions in the plane of the strips are plane waves whose transverse wave numbers are equal to α_m and k_y. Note that we have incidentally derived the Floquet space harmonics – an orthogonal set of plane-wave fields whose transverse phase constants α_m are given by Eq. (2.7b).

2.2 Finite Strip Grating

Much of what has already been said about the periodic strip grating applies equally well to the finite strip grating. The emphasis, therefore, will be on the main differences between the two problems. The geometry is illustrated in Fig. 2.1, where a finite number of strips is assumed to exist at regular intervals along the x axis. In this case, the representation describing the relationship between $J(x,y)$ and $J_0(x,y)$ is trivial, but it is still necessary to observe the distinction between the two functions. For the plane wave described by Eqs. (2.1) and (2.2),

$$J(x,y) = J_0(x)\, e^{jk_y y} , \qquad (2.8)$$

where $J_0(x)$ is the current density on the entire surface along the cut $y = 0$. Unlike the previous case, the currents flowing on the strips are no longer related by a simple phase shift, and in general, the current on each strip must be treated as unknown.

Taking the Fourier transform of Eq. (2.8) leads to

$$\tilde{J}(\alpha,\beta) = 2\pi\, \tilde{J}_0(\alpha)\; \delta(\beta - k_y), \qquad (2.9)$$

where, as before, $\tilde{J}_0(\alpha)$ with a single argument denotes a Fourier transform with respect to x only.

2.3 Periodic Two-Dimensional Structures

In Section 2.1, a one-dimensional structure was defined to be one in which the surface geometry is independent of one of the surface coordinates. Next, the treatment is extended to include two-dimensional surfaces, i.e., those, such as the one shown in Fig. 2.2, which are functions of both of the surface coordinates.
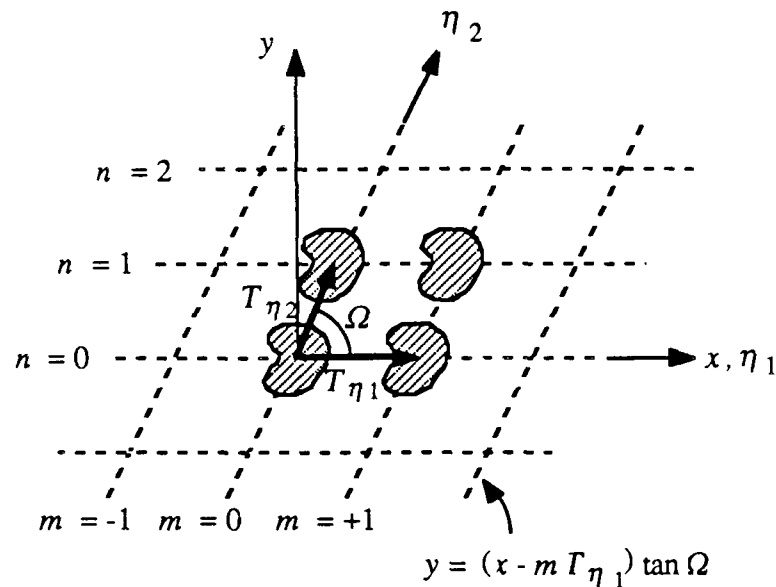

Figure 2.2. A two-dimensional periodic surface.

In the general case, the surface is considered to be periodic in skewed coordinates, with periodicities T_{η_1} and T_{η_2} along the η_1 and η_2 axes, respectively. A *unit cell* can be defined as the region $-T_x/2 \leq x \leq T_x/2$, $-T_y/2 \leq y \leq T_y/2$, as in the simple brick arrangement of Fig. 2.3. The unit cell is the minimum area of the FSS that can be reproduced in a periodic fashion to generate the entire FSS, including both aperture and patch regions inside the rectangular boundary.

The unit cell is not unique and may be chosen to suit the particular geometry of interest. However, it is not always possible to choose the unit cell such that exactly one element is enclosed within its boundaries. The two surfaces shown in Fig. 2.4 are common examples of this situation: parts of at least three elements must be enclosed within

the unit cell, and care must be taken to ensure that the currents are continuous across these fictitious mathematical boundaries.
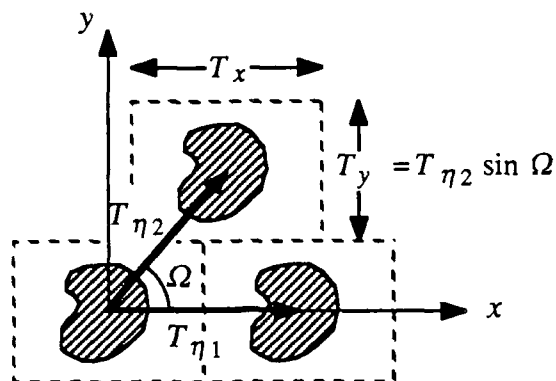
Figure 2.3.   Simple brick arrangement where each unit cell contains exactly one element.
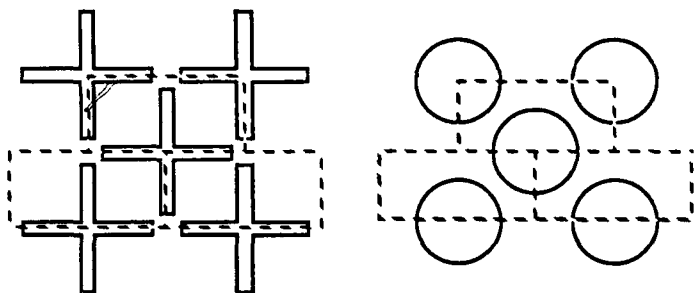
Figure 2.4.   Common geometries for which the unit cell encloses parts of at least three elements.

Although the concept of a unit cell is general enough to describe any periodic surface of the type shown in Fig. 2.2, it is much too restrictive a notion in practice. There is nothing inherent to the problem that requires defining a unit cell. For isolated elements, such as those shown in Figs. 2.2 - 2.4, it is always possible to represent the current density on the entire surface in terms of the current on a single element of the array. In this case, the terminology "unit cell" is sometimes used (very loosely) to denote a single element. The context will usually indicate the meaning.

It is always possible to choose the x axis of a Cartesian coordinate system along the η_1 axis of the FSS. Then the diagonal lines in Fig. 2.2, $m = 0, \pm1, \pm2$, etc., are given by

$$y = (x - mT_{\eta_1}) \tan \Omega.$$

Assuming that the incident field is a plane wave described by Eqs. (2.1)-(2.2), the induced current density $J(x,y)$ on the entire surface can be written in the form,

$$\mathbf{J}(x,y) = \mathbf{J}_0(x,y) * \left\{ \sum_{m=-\infty}^{\infty} \delta(x - y \cot\Omega - mT_{\eta_1})e^{jk_x x} \sum_{n=-\infty}^{\infty} \delta(y - nT_{\eta_2}\sin\Omega)e^{jk_y y} \right\},$$

$$(2.10)$$

where $\mathbf{J}_0(x,y)$ is the current density on a single element of the surface. Except for the phase-shift terms, the quantity in braces is a two-dimensional array of Dirac delta functions located at the points of intersection of the lines $m,n = 0, \pm1, \pm2, \ldots \infty$ in Fig. 2.2. Hence, Eq. (2.10) indicates that the current density on the entire surface can be constructed by convolving the fundamental unknown $\mathbf{J}_0(x,y)$ with a two-dimensional array of delta functions, appropriately modified by the phase shift of the incident field.

As shown in Section 2.1, this type of representation is not unique. The phase shift of the incident field could have been factored out beforehand, as follows:

$$\mathbf{J}(x,y) = \left\{ \mathbf{J}_0(x,y) * \left[\sum_{m=-\infty}^{\infty} \delta(x - y \cot\Omega - mT_{\eta_1}) \sum_{n=-\infty}^{\infty} \delta(y - nT_{\eta_2}\sin\Omega) \right] \right\} e^{jk_x x} e^{jk_y y}.$$

$$(2.11)$$

Because of the difference between the two representations, (2.10) and (2.11), the two currents $\mathbf{J}_0(x,y)$ are different as well. Under certain conditions, there may be advantages to using the second type of representation, viz., for electrically long elements or for currents that flow outside of unit-cell boundaries. However, the first type of representation is more convenient from the point of view of reconstructing $J(x,y)$ from $\mathbf{J}_0(x,y)$. The current on the patch at the origin is equal to $\mathbf{J}_0(x,y)$, and the current on any other patch is equal to

$J_0(x,y)$ times a constant. Neither of these statements is true for the second type of representation, as is evident from Eq. (2.11).

Anticipating that the Fourier transform of $J(x,y)$ will be needed later, the Fourier transform is defined as

$$\tilde{f}(\alpha,\beta) = \int_{-\infty}^{\infty} \int_{-\infty}^{\infty} f(x,y) \, e^{-j\alpha x} \, e^{-j\beta y} \, dx \, dy \ . \tag{2.12}$$

The Fourier transform of Eq. (2.10) is therefore

$$\tilde{J}(\alpha,\beta) = \tilde{J}_0(\alpha,\beta) \, \frac{2\pi}{T_{\eta_1}} \frac{2\pi}{T_{\eta_2} \sin\Omega} \sum_{m=-\infty}^{\infty} \sum_{n=-\infty}^{\infty} \delta(\alpha - \alpha_m) \, \delta(\beta - \beta_{mn}), \tag{2.13}$$

where

$$\alpha_m = \frac{2\pi m}{T_{\eta_1}} + k_x \tag{2.14a}$$

$$\beta_{mn} = \frac{2\pi n}{T_{\eta_2} \sin\Omega} - \frac{2\pi m}{T_{\eta_1}} \cot\Omega + k_y \ . \tag{2.14b}$$

Again, the spectrum of the current is discrete and is represented mathematically as a two-dimensional sequence of delta functions whose locations are the phase constants α_m and β_{mn} of the Floquet space harmonics. The only scattered fields that can exist above and below the surface are plane waves whose transverse wave numbers are equal to α_m and β_{mn}.

2.4 Finite Two-Dimensional Surfaces

In progressing from periodic to finite frequency selective surfaces, the problem becomes much more difficult computationally. For a periodic surface, the total current density on the surface can be represented in terms of the current density on a single unit cell; thus, it is only necessary to work with the equivalent of a single element of the array. In addition, since the spectrum of the current is discrete, the moment-method matrix generated by applying the spectral-Galerkin technique is filled by summing samples of the

Green's function, basis, and testing functions, in the Fourier-transform domain, at locations corresponding to the transverse wave numbers of the Floquet space harmonics.

In contrast to this, for a surface which is finite in two dimensions, the currents on each cell are, in general, different, and one is forced to treat the current on each individual cell as unknown. In the context of the method of moments, the number of unknown weight coefficients for an $N \times N$-element FSS is N^2 times the number of coefficients in the periodic problem for the same accuracy. In addition to being more numerous, the elements of the matrix are also more difficult to compute. The spectrum of the current is now continuous rather than discrete, and the moment matrix must be computed by numerically integrating the product of the Green's function, and basis and testing functions, in the spectral domain, over the infinite $\alpha-\beta$ plane.

As an intermediate step between the periodic and the two-dimensional finite surface, it is expedient to consider first a surface which is finite only in one dimension, permitting the surface to remain periodic in the other. In this case, a finite number of uniformly-spaced elements along the x axis are replicated in a periodic fashion along the line $y = x \tan\Omega$ (see Fig. 2.2). The currents on a given row of elements are no longer simply related; however, assuming that the incident field is a plane wave, the currents on any row of elements are related to the currents on any other row through the phase shift of the incident field. As a result, if the incident field is derived from the electric and magnetic vector potentials (2.1)-(2.2), then the induced current density on the entire surface can be represented by a convolution of $\mathbf{J}_0(x,y)$, the current density on a unit row of elements, and an infinite periodic sequence of Dirac delta functions, appropriately phase-shifted to account for the effect of the incident field:

$$\mathbf{J}(x,y) = \mathbf{J}_0(x,y) * \left\{ \sum_{n=-\infty}^{\infty} \delta(y - nT_{\eta_2}\sin\Omega) \, \delta(x - y\cot\Omega) \, e^{jk_x x} \, e^{jk_y y} \right\} . \quad (2.15)$$

The sequence of delta functions used here to construct the total current from $J_0(x,y)$ is the sequence of delta functions in Fig. 2.2 corresponding to $m = 0$.

Taking the Fourier transform of (2.15) leads directly to

$$\tilde{J}(\alpha,\beta) = \tilde{J}_0(\alpha,\beta) \frac{2\pi}{T_{\eta_2} \sin\Omega} \sum_{n=-\infty}^{\infty} \delta(\beta - \beta_n(\alpha)),\qquad(2.16)$$

where

$$\beta_n = \frac{2\pi n}{T_{\eta_2}\sin\Omega} - (\alpha - k_x)\cot\Omega + k_y \ .\qquad(2.17)$$

Except for the special case $\Omega = 90°$, the phase constants β_n will be functions of α.

As stated previously, for a frequency selective surface which is finite in two dimensions, there is no general relationship between the current on the entire surface and the current on any part of the surface. In the notation of this section,

$$J(x,y) = J_0(x,y),$$

where $J_0(x,y)$ is the current density on the entire two-dimensional surface.

In summary, the Fourier transform of the total induced current density $\tilde{J}(\alpha,\beta)$ can be expressed as the product of $\tilde{J}_0(\alpha,\beta)$, the Fourier transform of the current density on a subsection of the surface, times a periodicity function $\tilde{\Pi}(\alpha,\beta)$, which is either a constant, or a one- or two-dimensional array of Dirac delta functions,

$$\begin{bmatrix} \tilde{J}_x \\ \tilde{J}_y \end{bmatrix} = \begin{bmatrix} \tilde{J}_{x0} \\ \tilde{J}_{y0} \end{bmatrix} \tilde{\Pi}(\alpha,\beta) \ .\qquad(2.18)$$

CHAPTER 3

THE SPECTRAL-GALERKIN TECHNIQUE

3.1 Derivation of the Spectral-Domain Green's Function

One of the main reasons for choosing the spectral-domain formulation is the ability to derive the spectral-domain Green's function – a transform relationship between the scattered electric field in any transverse plane, due to the surface current **J** in any other plane.

$$
\begin{bmatrix} \tilde{E}_{x'}(\alpha,\beta) \\ \tilde{E}_{y'}(\alpha,\beta) \end{bmatrix} = \begin{bmatrix} \tilde{G}_{x'x'}(\alpha,\beta) & \tilde{G}_{x'y'}(\alpha,\beta) \\ \tilde{G}_{y'x'}(\alpha,\beta) & \tilde{G}_{y'y'}(\alpha,\beta) \end{bmatrix} \begin{bmatrix} \tilde{J}_{x'}(\alpha,\beta) \\ \tilde{J}_{y'}(\alpha,\beta) \end{bmatrix} . \tag{3.1}
$$

Here we have followed the convention of using the tilde to indicate a Fourier-transformed quantity, with the Fourier transform defined as

$$
\tilde{f}(\alpha,\beta) = \int_{-\infty}^{\infty} \int_{-\infty}^{\infty} f(x,y) \, e^{-j\alpha x} \, e^{-j\beta y} \, dx \, dy \ .
$$

Interpreting the elements of $\tilde{\mathbf{G}}$ from Eq. (3.1), $\tilde{G}_{x'x'}$, for example, is the Fourier transform of $E_{x'}$, the x' component of the scattered electric field in the plane $z' = 0$, divided by the Fourier transform of an infinite planar current sheet $J_{x'}(x',y') = e^{j(\alpha x' + \beta y')}$.

There are very few practical situations in which the printed surface can be considered as free-standing – in the absence of any supporting dielectric layers. Most often, the properties of the layers are fixed by mechanical constraints, i.e., because of weight limitations, or requirements for temperature stability, shape and rigidity, FSS support structures constructed with alternate layers of honeycomb and thin film are common in FSS applications. Optimization techniques have also been applied in order to design dielectric

layers to modify the electromagnetic properties of frequency selective surfaces [14]. The interest in free-standing surfaces is therefore limited, and it is essential that the FSS be considered in an environment consisting of a number of arbitrary dielectric layers.

The usual method of incorporating the effects of the dielectric support is the scattering-matrix approach [4, 15, 16]. If a plane-wave field is incident on a periodic surface, the scattered field is composed of an infinite number of discrete plane waves, whose wave numbers α_m, β_{mn} are the transverse phase constants of the Floquet space harmonics. If any one of these plane-wave fields is now incident upon another surface having the same periodicity, the scattered fields will consist of the same set of Floquet harmonics. In general, then, if a multilayered structure is composed only of uniform homogeneous dielectric layers and printed periodic surfaces having the same lattice ($T_{\eta 1}$, $T_{\eta 2}$, Ω), then the fields existing throughout the region can be represented exactly by a doubly-infinite set of plane-wave fields called the the Floquet space harmonics. In a lossless medium, a finite number of these plane-wave fields will be propagating, and the plane-wave fields corresponding to higher values of m and n will eventually be insignificant in comparison to the dominant terms. It is therefore only necessary to consider a finite number of Floquet harmonics in order to obtain an accurate representation for the fields in each layer.

Scattering from a given layer can now be described in terms of a matrix, whose elements relate the amount of power in a given scattered plane-wave field due to an incident plane wave from another direction. A scattering matrix is computed individually for each layer, and the matrices are cascaded to predict the scattered fields from the composite structure.

Because there is nothing analogous to the scattering-matrix approach for cascading *finite* frequency selective surfaces, it is desirable to develop the spectral-domain Green's function from a point of view which is general enough to be able to handle the geometry shown in Fig. 3.1, which is typical in practice [14, 17]. Here, it is assumed that a single

layer of metallization is embedded in an N-layer stratification, where each material is assumed to be an infinite, uniform, homogeneous dielectric layer of complex relative dielectric permittivity ε_r and magnetic permeability μ_0.

protective film

dielectric substrate

dielectric honeycomb structure

2 protective layers

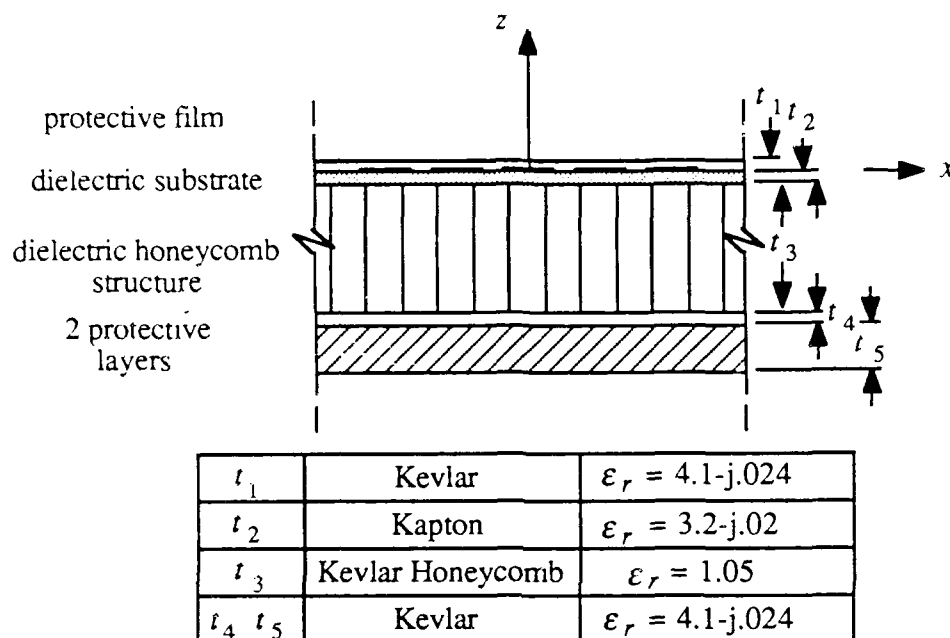| t_1	Kevlar	$\varepsilon_r = 4.1\text{-}j.024$
t_2	Kapton	$\varepsilon_r = 3.2\text{-}j.02$
t_3	Kevlar Honeycomb	$\varepsilon_r = 1.05$
$t_4 \; t_5$	Kevlar	$\varepsilon_r = 4.1\text{-}j.024$

Figure 3.1. Typical dielectric support used in FSS applications.

The derivation of the spectral Green's function is substantially the method of Itoh [18], which is based on the transmission-line analogy for a plane stratified medium. For completeness, and for the benefit of a different point of view, a detailed derivation of the spectral Green's function is provided below.

The transmission-line analogy is based on the following field properties: (1) any arbitrary field in a homogeneous source-free region can be expressed as the sum of a TE and a TM field; and (2) a plane wave propagating in a plane stratified medium, polarized either TE or TM with respect to the surface normal, will remain TE or TM throughout each layer of the stratification. Because of the similarity between the two-dimensional Fourier transforms of Maxwell's equations and the transmission-line equations, for each

polarization. a length of transmission line can be assigned to each layer of the structure and the transmission-line theory can be used to derive the Green's function.

In general, an arbitrary current sheet $J_{x'}(x',y')$ or $J_{y'}(x',y') = e^{j(\alpha x' + \beta y')}$ produces both TE and TM fields. Therefore, in order to apply the equivalent transmission-line analogy, the fields must be separated into their TE and TM components. To do this, it is advantageous to perform a rotation of the coordinate axes [18] in order to simplify the association between the field quantities E and H and the scalar quantities V and I.

The particular rotation of coordinates that achieves this simplification is determined by the following considerations: in order for the phases of the fields to match at every point on the boundary planes, the fields set up in each region due to the current sheet must be plane waves. Furthermore, the phase constants α and β of the assumed current distribution must be the x and y components, respectively, of the wave vectors of those plane-wave fields. The desired simplification results if the coordinate system is rotated about the z' axis until TE and TM with respect to z' are also TE and TM with respect to the plane of the wave vectors. In the new system, both E and H will have exactly one tangential component at the boundary planes, regardless of polarization. Equally as important, this coordinate transformation has the property that when the current sheet $J_{x'}$ or $J_{y'}$ is represented in the new coordinate system, one of its components will give rise to a field which is TE to z' and the other component will give rise to a field which is TM to z'.

The rotation of coordinates obtained by rotating the original ~· through an angle φ about the z' axis satisfies all of the conditions necessary to make a simple transition between the fields problem and the transmission-line problem. In the next section, however, it will be desirable to have the incident field propagating in the $+z$ direction to agree with the usual transmission-line conventions. Therefore, the final coordinate system is obtained by reversing the z' axis. The result is shown in Fig. 3.2, where, as long as it is necessary to make a distinction between the two, the original coordinate system will be

designated by the primed coordinates x', y', z' and the new coordinate system by the unprimed coordinates x, y, z;

$$\begin{bmatrix} \hat{x} \\ \hat{y} \end{bmatrix} = \begin{bmatrix} \cos\phi & \sin\phi \\ \sin\phi & -\cos\phi \end{bmatrix} \begin{bmatrix} \hat{x}' \\ \hat{y}' \end{bmatrix}$$

$$\begin{bmatrix} \hat{x}' \\ \hat{y}' \end{bmatrix} = \begin{bmatrix} \cos\phi & \sin\phi \\ \sin\phi & -\cos\phi \end{bmatrix} \begin{bmatrix} \hat{x} \\ \hat{y} \end{bmatrix} \qquad (3.2)$$

$$\hat{z} = -\hat{z}'.$$
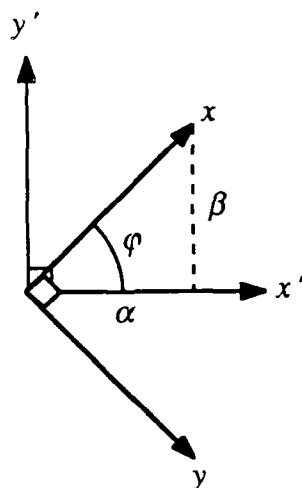
Figure 3.2. Coordinate transformation defined for the equivalent transmission-line analogy.

An arbitrary N-layer medium is shown in Fig. 3.3, with its corresponding equivalent transmission-line system, where the polarization p refers to TE or TM. In the ith layer, if the z-dependence of the fields traveling in the $+z$ direction is of the form $e^{-\gamma_i z}$, then the propagation constants γ_i are given by

$$\gamma_i = \sqrt{\alpha^2 + \beta^2 - \varepsilon_{ri} k_0^2}, \qquad (3.3)$$

where k_0 is the free-space wave number. The characteristic impedances of the equivalent transmission lines are defined as the wave impedances of the plane waves propagating (or attenuating) in the +z direction in each medium. From Maxwell's curl equations,

$$Z_{0i}^{TE} = \frac{-E_y}{H_x} = \frac{j\omega\mu_0}{\gamma_i} \qquad (3.4a)$$

$$Z_{0i}^{TM} = \frac{E_x}{H_y} = \frac{\gamma_i}{j\omega\varepsilon_{ri}\varepsilon_0} \qquad (3.4b)$$

With the equivalent transmission lines defined by (3.3) and (3.4), the problem can now be solved using a handful of highly-developed, systematic techniques.
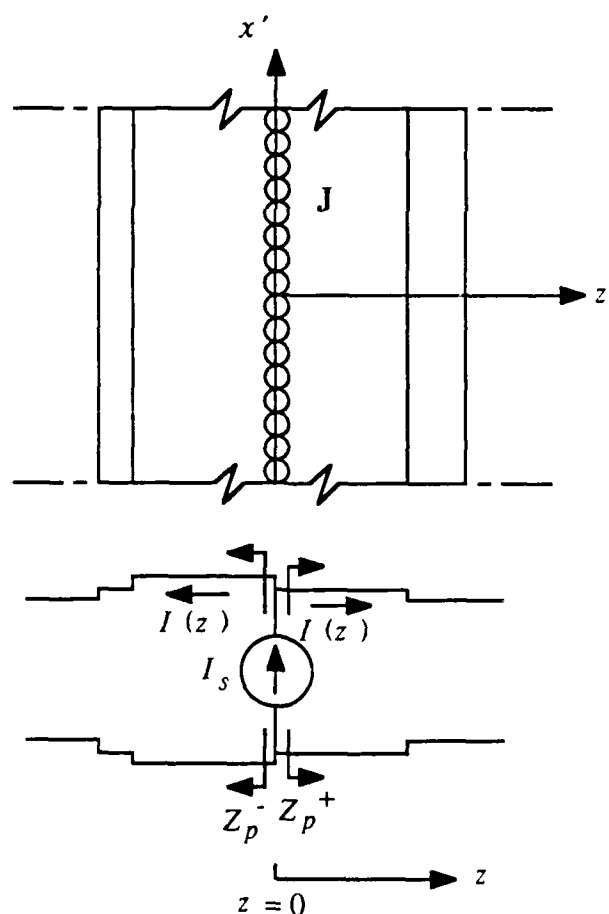

Figure 3.3. *N*-layer dielectric support and its equivalent transmission-line network.

In a given length of transmission line, the general solution to the telegrapher's equations can be expressed as a superposition of a +z-directed and a -z-directed wave,

$$V(z) = V^+e^{-\gamma z} + V^-e^{+\gamma z} = V^+(z) + V^-(z)$$
$$I(z) = \frac{1}{Z_0}[V^+e^{-\gamma z} - V^-e^{+\gamma z}],$$

where V^+ and V^- are arbitrary constants. If the generalized reflection coefficient $\Gamma(z)$ is defined as the reflected-wave voltage divided by the incident-wave voltage, i.e.,

$$\Gamma(z) = \frac{V^-(z)}{V^+(z)},$$

then the voltage and current on the line can be expressed in the form,

$$V(z) = V^+(z)[1 + \Gamma(z)] \tag{3.5a}$$
$$I(z) = \frac{1}{Z_0}V^+(z)[1 - \Gamma(z)]. \tag{3.5b}$$

Taking the ratio of the voltage and current leads to an expression for the impedance $Z(z)$,

$$Z(z) = \frac{V(z)}{I(z)} = Z_0\frac{1 + \Gamma(z)}{1 - \Gamma(z)}, \tag{3.6}$$

or, rewriting this in terms of $\Gamma(z)$,

$$\Gamma(z) = \frac{Z_n(z) - 1}{Z_n(z) + 1}, \tag{3.7}$$

where $Z_n(z)$ is the normalized impedance $Z(z)/Z_0$. Since $V^+(z) = V^+e^{-\gamma z}$ and $V^-(z) = V^-e^{+\gamma z}$, it follows that

$$\Gamma(z_1) = \Gamma(z_2)\, e^{2\gamma(z_1 - z_2)} \tag{3.8}$$

for any two points z_1 and z_2 on a section of uniform transmission line.

This brief review suggests the following strategy [19]: working from the load end to the source end of the transmission line, in any uniform section of line, (1) normalize the impedance at the load end by the characteristic impedance of the section, (2) calculate the reflection coefficient at the load end, (3) rotate the reflection coefficient toward the source using Eq. (3.8), (4) compute the normalized impedance at the source end, (5) unnormalize,

and (6) advance to the next section. The operations are highly repetitive and are efficiently implemented on a digital computer.

Once the input impedance seen by the source has been determined by the above procedure, the remaining steps are independent of the specifics of the problem. The boundary conditions satisfied by the fields $\mathbf{E}(z)$ and $\mathbf{H}(z)$ at $z = 0$ are

$$\hat{\mathbf{z}} \times [\, \mathbf{E}(0^+) - \mathbf{E}(0^-) \,] = 0 \tag{3.9a}$$

$$\hat{\mathbf{z}} \times [\, \mathbf{H}(0^+) - \mathbf{H}(0^-) \,] = \mathbf{J}, \tag{3.9b}$$

or, expanding Eq. (3.9) in Cartesian coordinates,

$$J_y = (\, H_x(0^+) - H_x(0^-) \,) \tag{3.10a}$$

$$J_x = - (\, H_y(0^+) - H_y(0^-) \,) \, . \tag{3.10b}$$

Assuming for the moment $\mathbf{J}(x',y') = \hat{\mathbf{x}}' e^{j(\alpha x' + \beta y')}$, then, according to the coordinate transformation,

$$\mathbf{J} = [\, \hat{\mathbf{x}} \cos\phi + \hat{\mathbf{y}} \sin\phi \,] \, e^{j\alpha x' + j\beta y'}. \tag{3.11}$$

The boundary condition satisfied by the magnetic field at the source plane is that the discontinuity in $\mathbf{H}_{\text{tan}}$ is equal to the surface current density $\mathbf{J}$. Since the tangential magnetic field is analogous to the current, symbolized by the notation $\mathbf{H}_{\text{tan}} \leftrightarrow I$, a discontinuity in $\mathbf{H}_{\text{tan}}$ corresponds to a shunt current source in the equivalent transmission line model. For the TE fields (E_y, H_x, H_z) and their corresponding transmission-line system, the appropriate boundary condition on $\mathbf{H}_{\text{tan}}$ and Kirchoff's current law at the source are (Fig. 3.4)

$$\text{KCL: } I_s = I(0^+) - [\, -I(0^-) \,] \tag{3.12}$$

$$\text{BC: } J_y = H_x(0^+) - H_x(0^-) \, . \tag{3.13}$$

Comparing (3.11), (3.12), and (3.13), the value of the equivalent current source $I_s = \sin\varphi$, and, since $V = I_s Z_{in}^{TE}$ and $E_y^{TE} \leftrightarrow -V$ (Eq. (3.4)),

$$E_y^{TE} = -Z_{in}^{TE} \sin\phi \, e^{j\alpha x' + j\beta y'} = E_{y0}^{TE} \, e^{j\alpha x' + j\beta y'}. \tag{3.14}$$
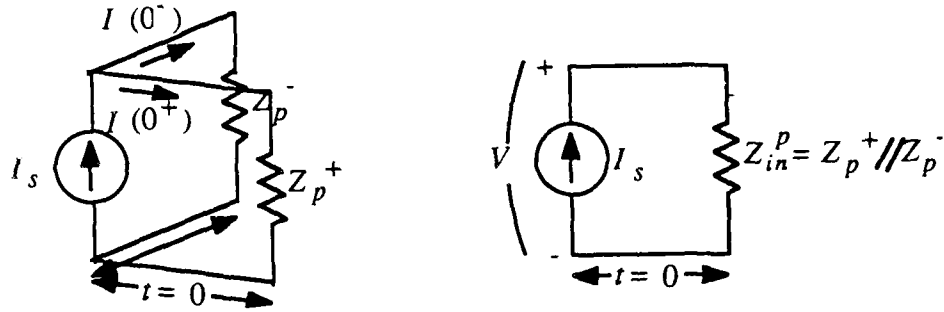
Figure 3.4. Equivalent circuits at the source terminals for the transmission-line system of Fig. 3.3.

For TM polarization (H_y, E_x, E_z),

$$\text{KCL: } I_s = I(0^+) - [\,-I(0^-)\,] \tag{3.15}$$

$$\text{BC: } -J_x = H_y(0^+) - H_y(0^-)\,. \tag{3.16}$$

Again, comparing (3.11), (3.15), and (3.16), $I_s = -\cos\varphi$, and, since $V = I_s Z_{in}^{\text{TM}}$ and $E_x^{\text{TM}} \leftrightarrow +V$ (Eq. (3.4)),

$$E_x^{\text{TM}} = -Z_{in}^{\text{TM}} \cos\phi\; e^{j\alpha x' + j\beta y'} = E_{x0}^{\text{TM}}\; e^{j\alpha x' + j\beta y'}. \tag{3.17}$$

In the remaining steps, the fields are converted back to the original coordinate system, and the TE and TM components are superposed to obtain the total field,

$$E_{x'} = [\, E_{y0}^{\text{TE}} \sin\phi + E_{x0}^{\text{TM}} \cos\phi \,]\; e^{j\alpha x' + j\beta y'} = -\,[\, Z_{in}^{\text{TE}} \sin^2\phi + Z_{in}^{\text{TM}} \cos^2\phi \,]\; e^{j\alpha x' + j\beta y'} \tag{3.18a}$$

$$E_{y'} = [\, -E_{y0}^{\text{TE}} \cos\phi + E_{x0}^{\text{TM}} \sin\phi \,]\; e^{j\alpha x' + j\beta y'} = +\,[\, Z_{in}^{\text{TE}} - Z_{in}^{\text{TM}} \,]\; \sin\phi \cos\phi\; e^{j\alpha x' + j\beta y'} \tag{3.18b}$$

or, from the definition of $\widetilde{G}$ (Eq. (3.1)),

$$\widetilde{G}_{x'x'} = \frac{\widetilde{E}_{x'}}{\widetilde{J}_{x'}} = -\,[\, Z_{in}^{\text{TE}} \sin^2\phi + Z_{in}^{\text{TM}} \cos^2\phi \,] \tag{3.19a}$$

$$\widetilde{G}_{y'x'} = \frac{\widetilde{E}_{y'}}{\widetilde{J}_{x'}} = +\,[\, Z_{in}^{\text{TE}} - Z_{in}^{\text{TM}} \,]\; \sin\phi \cos\phi\,. \tag{3.19b}$$

Sinφ and cosφ are related to α and β by the following relations:

$$\sin\phi = \frac{\beta}{\sqrt{\alpha^2 + \beta^2}} \qquad (3.20a)$$

$$\cos\phi = \frac{\alpha}{\sqrt{\alpha^2 + \beta^2}} \qquad (3.20b)$$

as is evident from Fig. 3.2. A similar procedure can be used to derive $\tilde{G}_{x'y'}(\alpha,\beta)$ and $\tilde{G}_{y'y'}(\alpha,\beta)$. Only the results are summarized below:

$$\tilde{G}_{x'y'} = \frac{\tilde{E}_{x'}}{\tilde{J}_{y'}} = + [\, Z_{in}^{TE} - Z_{in}^{TM} \,] \sin\phi \cos\phi \qquad (3.21a)$$

$$\tilde{G}_{y'y'} = \frac{\tilde{E}_{y'}}{\tilde{J}_{y'}} = - [\, Z_{in}^{TE} \cos^2\phi + Z_{in}^{TM} \sin^2\phi \,] \,. \qquad (3.21b)$$

As an important special case of the above, the free-space Green's function can be written immediately by recognizing that

$$Z_{in}^{TE} = Z_{00}^{TE} // Z_{00}^{TE} = \frac{j\omega\mu}{2\gamma_0} \qquad (3.22a)$$

$$Z_{in}^{TM} = Z_{00}^{TM} // Z_{00}^{TM} = \frac{\gamma_0}{2j\omega\varepsilon_0} \,, \qquad (3.22b)$$

where Z_{00}^{TE} and Z_{00}^{TM} are the characteristic impedances for the TE and TM plane-wave fields propagating in free-space, and γ_0 is the free-space propagation constant, as defined by Eq. (3.3) with $\varepsilon_r = 1$. From (3.19) and (3.21),

$$\tilde{\mathbf{G}}(\alpha,\beta) = \frac{1}{2j\omega\varepsilon_0\gamma_0} \begin{bmatrix} k_0^2 - \alpha^2 & -\alpha\beta \\ -\alpha\beta & k_0^2 - \beta^2 \end{bmatrix} . \qquad (3.23)$$

As a second example, the Green's function for a two-layer dielectric support is derived, where the current sheet is assumed to be embedded between two layers characterized by complex relative dielectric permittivities ε_{r1}, ε_{r2} and thicknesses t_1, t_2 as shown in Fig. 3.5. When the two transmission lines extending to $z = \pm\infty$ are replaced by

their characteristic impedances, the impedances Z_p^+ and Z_p^- as viewed in the $+z$ and $-z$ directions, respectively, are written,

$$Z_p^+ = Z_{02}^p \frac{1 + \dfrac{Z_{00}^p - Z_{02}^p}{Z_{00}^p + Z_{02}^p}e^{-2\gamma_2 t_2}}{1 - \dfrac{Z_{00}^p - Z_{02}^p}{Z_{00}^p + Z_{02}^p}e^{-2\gamma_2 t_2}} = Z_{02}^p \frac{Z_{02}^p + Z_{00}^p \coth\gamma_2 t_2}{Z_{00}^p + Z_{02}^p \coth\gamma_2 t_2}$$

$$Z_p^- = Z_{01}^p \frac{1 + \dfrac{Z_{00}^p - Z_{01}^p}{Z_{00}^p + Z_{01}^p}e^{-2\gamma_1 t_1}}{1 - \dfrac{Z_{00}^p - Z_{01}^p}{Z_{00}^p + Z_{01}^p}e^{-2\gamma_1 t_1}} = Z_{01}^p \frac{Z_{01}^p + Z_{00}^p \coth\gamma_1 t_1}{Z_{00}^p + Z_{01}^p \coth\gamma_1 t_1} .$$

The total input impedance Z_{in}^p seen by the source is the parallel combination of Z_p^+ and Z_p^-,

$$Z_{in}^p = \frac{Z_{01}^p Z_{02}^p [Z_{02}^p + Z_{00}^p \coth\gamma_2 t_2][Z_{01}^p + Z_{00}^p \coth\gamma_1 t_1]}{Z_{02}^p [Z_{00}^p + Z_{01}^p \coth\gamma_1 t_1][Z_{02}^p + Z_{00}^p \coth\gamma_2 t_2] + Z_{01}^p [Z_{01}^p + Z_{00}^p \coth\gamma_1 t_1][Z_{00}^p + Z_{02}^p \coth\gamma_2 t_2]} .$$

$$(3.24)$$

The Green's function is then given by Eqs. (3.19) and (3.21).

3.2 Asymptotic Behavior of the Green's Function

Asymptotic expressions for the spectral Green's function are easily found. If $k_\rho^2 \gg |\varepsilon_{ri}|k_0^2$ and $k_\rho t_i > \pi$ for each finite-thickness layer, then asymptotically

$$\gamma_i \to k_\rho \tag{3.25}$$

$$\coth\gamma_i t_i \to 1. \tag{3.26}$$

The characteristic impedances of the equivalent transmission lines are, therefore,

$$Z_{0i}^{TE} \to \frac{j\omega\mu}{k_\rho} \tag{3.27a}$$

$$Z_{0i}^{TM} \to \frac{k_\rho}{j\omega\varepsilon_{ri}\varepsilon_0} . \tag{3.27b}$$
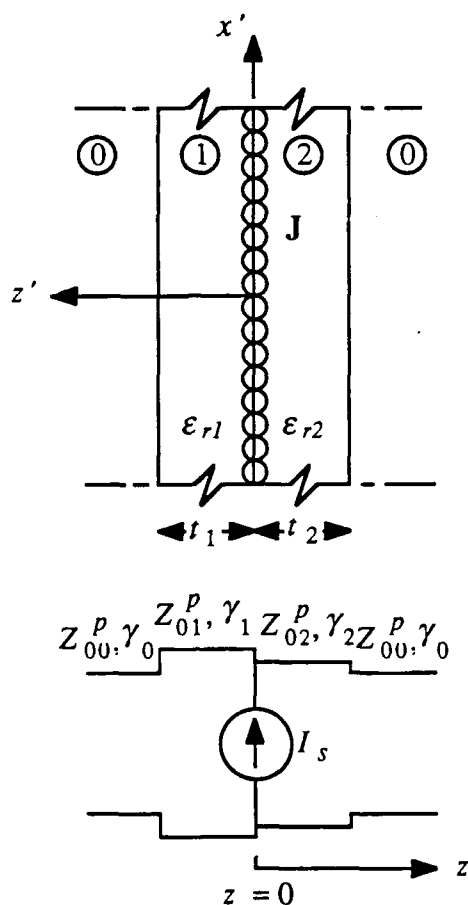
Figure 3.5. Geometry of two-layer dielectric support and its equivalent transmission-line system.

According to Eq. (3.27), the characteristic impedances for the TE transmission-line system are independent of the parameters of the layers. The characteristic impedances of the TM transmission line system differ only by a multiplicative constant. As a result, the input impedance Z_{in}^{TE} is the parallel combination of two terms of the form $j\omega\mu/k_\rho$,

$$Z_{in}^{TE} \rightarrow \frac{j\omega\mu}{2k_\rho} . \tag{3.28}$$

Furthermore, it is not difficult to verify that under the approximations (3.24)-(3.27) the input impedance Z_{in}^{TM} depends only on the dielectric constants of the layers nearest the source,

$$Z_{in}^{TM} \rightarrow \frac{k_\rho}{j\omega\varepsilon_0(\varepsilon_{r+} + \varepsilon_{r-})} , \tag{3.29}$$

where ε_{r+} and ε_{r-} are the relative permittivities of the two layers adjacent to the current sheet. Substituting the asymptotic formulas (3.28) and (3.29) into Eqs. (3.19) and (3.21), the Green's function becomes

$$\tilde{G}_{xx} \rightarrow \frac{-1}{j\omega\varepsilon_0\sqrt{\alpha^2 + \beta^2}} \left[\frac{-k_0^2\beta^2}{2(\alpha^2 + \beta^2)} + \frac{\alpha^2}{(\varepsilon_{r+} + \varepsilon_{r-})} \right] \tag{3.30a}$$

$$\tilde{G}_{xy} \rightarrow \frac{-\alpha\beta}{j\omega\varepsilon_0\sqrt{\alpha^2 + \beta^2}} \left[\frac{k_0^2}{2(\alpha^2 + \beta^2)} + \frac{1}{(\varepsilon_{r+} + \varepsilon_{r-})} \right] \tag{3.30b}$$

$$\tilde{G}_{yy} \rightarrow \frac{-1}{j\omega\varepsilon_0\sqrt{\alpha^2 + \beta^2}} \left[\frac{-k_0^2\alpha^2}{2(\alpha^2 + \beta^2)} + \frac{\beta^2}{(\varepsilon_{r+} + \varepsilon_{r-})} \right] . \tag{3.30c}$$

These results are useful for several reasons. First, since the Green's function appears in the product $\tilde{\mathbf{j}}_i^\dagger(\alpha,\beta)\tilde{\mathbf{G}}(\alpha,\beta)\tilde{\mathbf{j}}_j(\alpha,\beta)$, the asymptotic form of the Green's function determines the minimum rate of decay necessary in the Fourier transforms of the basis and testing functions in order for the inner products to converge. If, in polar coordinates, the product $\tilde{\mathbf{j}}_i^\dagger\tilde{\mathbf{G}}\tilde{\mathbf{j}}_j$ does not decay faster than $1/k_\rho$, the inner product will not converge, and a smoother set of basis and testing functions must be chosen. Second, since the asymptotic forms are considerably simpler than the general forms, it is possible, for a judicious choice of basis and testing functions, to perform the asymptotic integrations exactly [20]. This would offer advantages in terms of both speed and accuracy. However, even if the inner products cannot be evaluated exactly using the asymptotic form of the Green's function, the asymptotic form requires considerably less computational effort than the general form. Numerical experiments have shown that significant savings in computation time can be achieved by using the asymptotic form when k_ρ becomes sufficiently large.

3.3 Singularities of the Spectral Green's Function

The spectral-domain Green's function for sources in a lossless plane stratified medium has singularities of two different types. First, since the propagation constants γ_i are defined in terms of the square root function, which is a multivalued function, there are branch points at the locations $k_\rho^2 = \varepsilon_{ri}k_0^2$, where $k_\rho^2 = \alpha^2 + \beta^2$. At these points the derivative of the Green's function is undefined. There are also nonintegrable singularities caused by zeros in the denominators of the input impedances Z_{in}^{TE} and Z_{in}^{TM} which correspond to guided modes in the dielectric-slab waveguide.

Beyond this, very little can be said about the singularities without considering a specific example. Returning to the two-layer example discussed in Sec. 3.1, if the substrate and superstrate are identical, such that $\varepsilon_{r1} = \varepsilon_{r2} = \varepsilon_r$, $t_1 = t_2 = t$, and $\gamma_1 = \gamma_2 = \gamma$, then the denominators Δ_{TE}, Δ_{TM} of the impedances Z_{in}^{TE} and Z_{in}^{TM}, respectively, are given by

$$\Delta_{TE} = \frac{(-j\omega\varepsilon_0)^2}{\gamma_0^2\gamma^4} 2\varepsilon_r\gamma(\varepsilon_r\gamma_0 + \gamma\coth\gamma t)(\varepsilon_r\gamma_0\coth\gamma t + \gamma) \tag{3.31a}$$

$$\Delta_{TM} = \left(\frac{-1}{j\omega\mu_0}\right)^3 2\gamma(\gamma + \gamma_0\coth\gamma t)(\gamma\coth\gamma t + \gamma_0) . \tag{3.31b}$$

If pole-zero cancellation does not occur, then the non-branch-type singularities of the Green's function will be solutions of

$$(\varepsilon_r\gamma_0 + \gamma\coth\gamma t) = 0 \tag{3.32a}$$

$$(\varepsilon_r\gamma_0\coth\gamma t + \gamma) = 0 \tag{3.32b}$$

$$(\gamma + \gamma_0\coth\gamma t) = 0 \tag{3.32c}$$

$$(\gamma\coth\gamma t + \gamma_0) = 0 . \tag{3.32d}$$

Since γ_i is a function of k_ρ^2 only, i.e., since γ_i is not a function of the polar angle, the singularities of Z_{in}^{TE} and Z_{in}^{TM} lie on concentric circles about the origin in the $\alpha-\beta$ plane. Since Eqs. (3.32a-d) are transcendental equations, the locations of the singularities can only be determined numerically. However, if the dielectrics are lossless, the following

general observations can be made. First, the number and locations of the singularities depend on frequency, the relative dielectric constants, and thicknesses of the layers. If any two of these parameters are held constant while the other is varied, higher frequencies, higher dielectric constants and greater thicknesses all tend to produce more singularities in the Green's function. Second, for $k_\rho > \sqrt{\varepsilon_{r_{max}}}k_0$, where $\varepsilon_{r_{max}}$ is the maximum of ε_{r_i}, γ_i is real and positive, $\coth\gamma_i t$ is real and positive, and each term in Eqs. (3.32a-d) is the sum of two nonzero positive numbers. In such a case, Eqs. (3.32a-d) have no real solutions. Recalling that the branch-type singularities occur at $k_\rho = \sqrt{\varepsilon_{r_i}}k_0$, there can be no singularities of either type in the region $k_\rho > \sqrt{\varepsilon_{r_{max}}}k_0$. Likewise, for $k_\rho < k_0$, a similar argument holds. Therefore, all of the singularities lie somewhere in the annular region $k_0 \leq k_\rho \leq \sqrt{\varepsilon_{r_{max}}}k_0$. Figure 3.6 is a plot of the Green's function for a structure with two identical layers, characterized by $\varepsilon_r = 4.0$, $t = \lambda_0/6$ along the radial line $\alpha = \beta$. Eventually, $\tilde{G}_{xx}(\alpha,\beta)$ and $\tilde{G}_{yy}(\alpha,\beta)$ increase linearly with k_ρ, becoming unbounded at ∞.
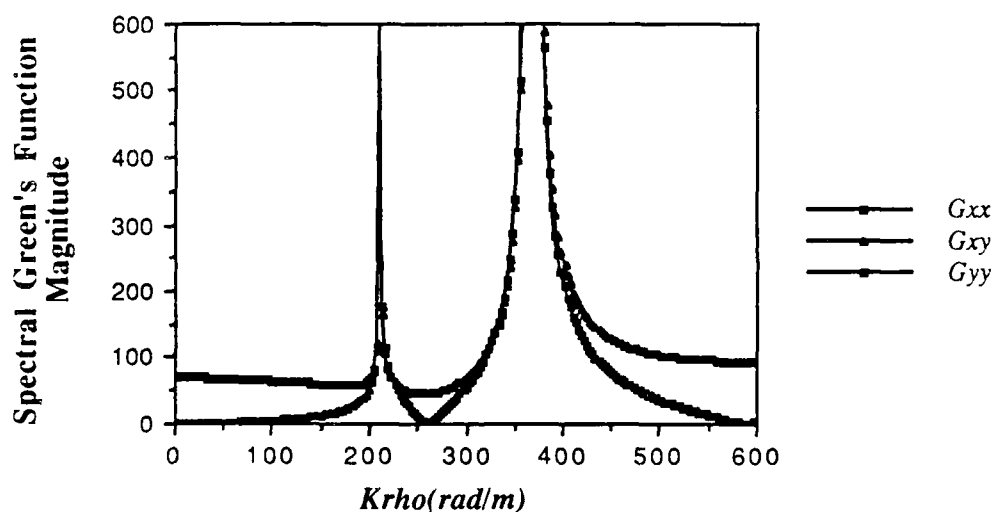

Figure 3.6. Spectral Green's function for the fields at the center of two identical layers of permittivity $\varepsilon_r = 4.0$ and thickness $t = \lambda_0/6$ (frequency = 10 GHz).

3.4 The Spectral-Galerkin Equation

As was shown in Sec. 3.1, the general relationship between the scattered electric field and an arbitrary surface current **J** radiating in the presence of a number of infinite, homogeneous dielectric layers can be written in the form

$$
\begin{bmatrix} \tilde{E}_x(\alpha,\beta) \\ \\ \tilde{E}_y(\alpha,\beta) \end{bmatrix} = \begin{bmatrix} \tilde{G}_{x'x'}(\alpha,\beta) & \tilde{G}_{x'y'}(\alpha,\beta) \\ \\ \tilde{G}_{y'x'}(\alpha,\beta) & \tilde{G}_{y'y'}(\alpha,\beta) \end{bmatrix} \begin{bmatrix} \tilde{J}_x(\alpha,\beta) \\ \\ \tilde{J}_y(\alpha,\beta) \end{bmatrix}.
$$

The current density **J** is now interpreted as the induced current on a printed frequency selective surface (whether finite or periodic), given by one of the representations (2.4), (2.8), (2.10), or (2.15). Except for one or two special cases [10], the current $J_0(x,y)$ cannot be determined analytically, and numerical techniques must be used in order to compute it.

The spectral-domain method of moments proceeds as follows. Choosing a suitable set of linearly-independent basis functions $\{\mathbf{j}_j\}$, the current J_0 is expanded in the form,

$$
\begin{bmatrix} \tilde{J}_{x0} \\ \\ \tilde{J}_{y0} \end{bmatrix} = \sum_{j=1}^{I} c_j \begin{bmatrix} \tilde{j}_{xj} \\ \\ \tilde{j}_{yj} \end{bmatrix}, \tag{3.33}
$$

where $\{c_j\}$ is a set of complex-valued weight coefficients which are yet to be determined. There are four main considerations involved in choosing an appropriate set of basis functions in the spectral-domain method of moments. First, as with any moment-method solution, the basis functions must be linearly independent. If any one basis function could be represented in terms of a linear combination of two other basis functions, for example, then one column of the moment matrix would be representable in terms of two others, and the matrix would be singular. Second, since the method of solution is a transform-domain technique, the basis and testing functions must be Fourier transformable. This is not a serious limitation, since all, or nearly all, basis functions used in practice are Fourier transformable. A third consideration, which is especially significant for the analysis of

finite frequency selective surfaces, is that the basis must be capable of representing the fundamental unknown with a small number of terms. This is because the matrix size is proportional to N^2 for an $N \times N$-element array. For example, for the entire-domain basis set of Orta, Tascone, and Zich [21], about twelve basis functions per arm are necessary to accurately represent the current on a particular tripole element. At 36 basis functions per element, even a small 10×10 array would require filling and storing a 3600×3600-element matrix. A fourth consideration that must be observed in choosing a basis is the requirement that the basis and testing functions together have sufficient smoothness to guarantee that the integrals and summations generated by the spectral method of moments converge. It is also desirable that the basis functions model, at least approximately, the known physical behavior of the current. For example, the current flowing parallel to the edge of a printed element exhibits an edge singularity proportional to $1/\sqrt{x - x_0}$, where $(x - x_0)$ is the distance from the edge.

Substituting for $\tilde{\mathbf{J}}$ and $\tilde{\mathbf{J}}_0$, the scattered electric field is of the form

$$\begin{bmatrix} E_x^s \\ E_y^s \end{bmatrix} = \frac{1}{4\pi^2} \sum_{j=1}^{I} c_j \int_{-\infty}^{\infty} \int_{-\infty}^{\infty} \begin{bmatrix} \tilde{G}_{xx} & \tilde{G}_{xy} \\ \tilde{G}_{yx} & \tilde{G}_{yy} \end{bmatrix} \begin{bmatrix} \tilde{j}_{xj} \\ \tilde{j}_{yj} \end{bmatrix} \tilde{\Pi}(\alpha,\beta) \, e^{j\alpha x + j\beta y} d\alpha d\beta . \quad (3.34)$$

Next, an inner product is defined satisfying properties (1-2)-(1-4) of Harrington [22],

$$\langle \mathbf{f}, \mathbf{g} \rangle = \int_{-\infty}^{\infty} \mathbf{f}^T(x) \, \mathbf{g}(x,y) dx , \quad \text{(strip grating)} , \quad (3.35a)$$

$$\langle \mathbf{f}, \mathbf{g} \rangle = \int_{-\infty}^{\infty} \int_{-\infty}^{\infty} \mathbf{f}^T(x,y) \, \mathbf{g}(x,y) dx dy , \quad \text{(two–dimensional element)} , \quad (3.35b)$$

where the superscript "T" signifies transpose. Choosing the testing functions to be the complex conjugates of the basis functions [23], and forming the inner product of Eq. (3.34) with each testing function lead to a system of I equations in I unknowns

$$\langle \mathbf{j}_i^*, \mathbf{E}^s \rangle = \frac{1}{4\pi^2}\sum_{j=1}^{I} c_j \iint \iint \mathbf{j}_i^\dagger(x,y)\, e^{j\alpha x + j\beta y}dxdy \;\; \tilde{\mathbf{G}}(\alpha,\beta)\, \tilde{\mathbf{j}}_j(\alpha,\beta)\tilde{\Pi}(\alpha,\beta)\, d\alpha d\beta \,,$$

(3.36)

where the dagger "$\dagger$" signifies complex conjugate transpose. The double integral over x and y can be recognized as a Fourier-transform-type integral, which can be done analytically, resulting in the equation

$$\frac{-1}{4\pi^2}\sum_{j=1}^{I} c_j \int_{-\infty}^{\infty}\int_{-\infty}^{\infty} \tilde{\mathbf{j}}_i^\dagger(\alpha,\beta)\, \tilde{\mathbf{G}}(\alpha,\beta)\, \tilde{\mathbf{j}}_j(\alpha,\beta)\tilde{\Pi}(\alpha,\beta)\, d\alpha d\beta \;=\; \langle \mathbf{j}_i^*, \mathbf{E}^{inc} \rangle, \;\; i = 1,\, 2,\, ...,\, I\,.$$

(3.37)

As a result of testing with $\mathbf{j}_i$, the equation has been restricted to the surfaces of the conductors. The boundary condition has therefore been enforced by replacing the scattered field with the negative of the incident field on the right-hand side. The specific form of Eq. (3.37) will depend on the specifics of the problem, but for the five general types of problems discussed in Chapter 2, the spectral-Galerkin equation is summarized below:

1. Periodic Strip Grating (Fig. 2.1):

$$\tilde{\Pi}(\alpha,\beta) = \frac{4\pi^2}{b}\sum_{m=-\infty}^{\infty} \delta(\alpha - \alpha_m)\, \delta(\beta - k_y)\,, \quad \alpha_m = \frac{2\pi m}{b} + k_x\,, \qquad (3.38)$$

$$\frac{-1}{b}\sum_{j=1}^{I} c_j \sum_{m=-\infty}^{\infty} \tilde{\mathbf{j}}_i^\dagger(\alpha_m)\, \tilde{\mathbf{G}}(\alpha_m,k_y)\, \tilde{\mathbf{j}}_j(\alpha_m)e^{jk_y y} = \int_{x=-\infty}^{\infty} \mathbf{j}_i^\dagger(x)\, \mathbf{E}^{inc}(x,y)\, dx\,, \;\; i = 1,\, 2,\, ...,\, I\,.$$

(3.39)

2. Finite Strip Grating (Fig. 2.1):

$$\tilde{\Pi}(\alpha,\beta) = 2\pi\, \delta(\beta - k_y)\,, \qquad (3.40)$$

$$\frac{-1}{2\pi}\sum_{j=1}^{I} c_j \int_{-\infty}^{\infty} \tilde{\mathbf{j}}_i^\dagger(\alpha)\, \tilde{\mathbf{G}}(\alpha,k_y)\, \tilde{\mathbf{j}}_j(\alpha)e^{jk_y y}d\alpha = \int_{x=-\infty}^{\infty} \mathbf{j}_i^\dagger(x)\, \mathbf{E}^{inc}(x,y)\, dx\,, \;\; i = 1,\, 2,\, ...,\, I\,.$$

(3.41)

3. Periodic Two-Dimensional Surfaces (Fig. 2.2):

$$\tilde{\Pi}(\alpha,\beta) = \frac{2\pi}{T_{\eta_1}} \frac{2\pi}{T_{\eta_2}\sin\Omega} \sum_{m=-\infty}^{\infty} \sum_{n=-\infty}^{\infty} \delta(\alpha - \alpha_m)\, \delta(\beta - \beta_{mn}),$$
(3.42)

$$\alpha_m = \frac{2\pi m}{T_{\eta_1}} + k_x \,,$$
(3.43a)

$$\beta_{mn} = \frac{2\pi n}{T_{\eta_2}\sin\Omega} - \frac{2\pi m}{T_{\eta_1}} \cot\Omega + k_y \,,$$
(3.43b)

$$\frac{-1}{T_{\eta_1} T_{\eta_2}\sin\Omega} \sum_{j=1}^{I} c_j \sum_{m=-\infty}^{\infty} \sum_{n=-\infty}^{\infty} \tilde{\mathbf{j}}_i^{\dagger}(\alpha_m,\beta_{mn})\, \tilde{\mathbf{G}}(\alpha_m,\beta_{mn})\, \tilde{\mathbf{j}}_j(\alpha_m,\beta_{mn})$$

$$= \int_{-\infty}^{\infty} \int_{-\infty}^{\infty} \mathbf{j}_i^{\dagger}(x,y)\, \mathbf{E}^{inc}(x,y)\, dxdy \,, \quad i = 1, 2, ..., I$$
(3.44)

4. Finite-Width Two-Dimensional Surfaces (Fig. 2.2):

$$\tilde{\Pi}(\alpha,\beta) = \frac{2\pi}{T_{\eta_2}\sin\Omega} \sum_{n=-\infty}^{\infty} \delta(\beta - \beta_n(\alpha)) \,,$$
(3.45)

$$\beta_n(\alpha) = \frac{2\pi n}{T_{\eta_2}\sin\Omega} - (\alpha - k_x)\cot\Omega + k_y \,,$$
(3.46)

$$\frac{-1}{2\pi T_{\eta_2}\sin\Omega} \sum_{j=1}^{I} c_j \sum_{n=-\infty}^{\infty} \int_{-\infty}^{\infty} \tilde{\mathbf{j}}_i^{\dagger}(\alpha,\beta_n)\, \tilde{\mathbf{G}}(\alpha,\beta_n)\, \tilde{\mathbf{j}}_j(\alpha,\beta_n)d\alpha$$

$$= \int_{-\infty}^{\infty} \int_{-\infty}^{\infty} \mathbf{j}_i^{\dagger}(x,y)\, \mathbf{E}^{inc}(x,y)\, dxdy \,, \quad i = 1, 2, ..., I \,.$$
(3.47)

5. Surfaces That Are Finite in Two-Dimensions (Fig. 2.2):

$$\tilde{\Pi}(\alpha,\beta) = 1 \,,$$
(3.48)

$$\frac{-1}{T_{\eta_1} T_{\eta_2} \sin\Omega} \sum_{j=1}^{I} c_j \int_{-\infty}^{\infty} \int_{-\infty}^{\infty} \tilde{\mathbf{j}}_i^{\dagger}(\alpha,\beta) \; \tilde{\mathbf{G}}(\alpha,\beta) \; \tilde{\mathbf{j}}_j(\alpha,\beta) d\alpha d\beta$$

$$= \int_{-\infty}^{\infty} \int_{-\infty}^{\infty} \mathbf{j}_i^{\dagger}(x,y) \; \mathbf{E}^{inc}(x,y) \; dxdy \; , \quad i = 1, 2, ..., I \; . \tag{3.49}$$

From this summary, it is possible to see that the difficulty involved in computing the moment matrix ranges from performing a summation over samples of the Green's function, basis, and testing functions at the discrete values α_m, β_{mn} to a complete two-dimensional integration over the infinte α–β plane.

3.5 Incident Field

The spectral-Galerkin equation derived in the previous section is written in terms of the quantity $\mathbf{E}^{inc}$, defined as the electric field reaching the plane of the printed conducting surface with the conductors removed, i.e., in the presence of the dielectric support. For plane-wave incidence, the tangential field $\mathbf{E}_t^{inc}$ is of the form,

$$\mathbf{E}_t^{inc} = [\; \hat{\mathbf{x}}' E_{x'0} + \hat{\mathbf{y}}' E_{y'0} \;] e^{jk_x x' + jk_y y'}, \tag{3.50}$$

where $E_{x'0}$ and $E_{y'0}$ are complex constants. When combined with the testing functions, the inner product (3.28) becomes

$$\langle \mathbf{j}_i^{\dagger}, \mathbf{E}_t^{inc} \rangle = \int\!\!\int [\, j_{ix'}^*(x',y') \quad j_{iy'}^*(x',y') \,] \begin{bmatrix} E_{x0} \\ E_{y0} \end{bmatrix} e^{jk_x x' + jk_y y'} dx' dy' \; . \tag{3.51}$$

This can be recognized as a Fourier-transform type of operation, allowing the integration to be done analytically, resulting in

$$\langle \mathbf{j}_i^{\dagger}, \mathbf{E}_t^{inc} \rangle = E_{x'0}[\, \tilde{j}_{ix'}(k_{x'},k_{y'}) \,]^* + E_{y'0}[\, \tilde{j}_{iy'}(k_{x'},k_{y'}) \,]^* \; . \tag{3.52}$$

For the strip grating,

$$\langle \mathbf{j}_i^{\dagger}, \mathbf{E}_t^{inc} \rangle = \int_{x'=-\infty}^{\infty} \mathbf{j}_i^{\dagger}(x') \mathbf{E}_t^{inc}(x',y') dx' = \{ E_{x'0} \tilde{j}_{ix'}^*(k_{x'}) + E_{y'0} \tilde{j}_{iy'}^*(k_{x'}) \} e^{jk_y y'} \; . \tag{3.53}$$

In order to find the constants $E_{x'0}$ and $E_{y'0}$, we will again make use of the transmission-line analogy and rotation of coordinates defined in the derivation of the

Green's function. In passing, we note that the fields in a plane stratified medium can also be determined by writing a representation for the fields in each region and matching the tangential components of **E** and **H** at the interfaces to solve for the unknown constants. For two layers, there are six unknown constants to be determined by solving a sixth-order system of equations. While this is a valid means of proceeding, the derivation is lengthy and difficult, and it is impractical for three layers or more.

For a plane wave polarized either TE or TM with respect to the surface normal and propagating along the line defined by the spherical angles (θ_i, φ_i), the field anywhere in an N-layer dielectric medium can be derived by the following steps. First, rotate the coordinate axes so that the incident propagation vector is in the x-z plane of the new coordinate system. The incident angle φ_i is equal to the φ of Fig. 3.2. If the incident field is derived from the unit vector potentials **A** and **F**, then the plane-wave fields propagating in a free-space region in the absence of scatterers are given by Harrington [24],

$$\mathbf{E}_{t0}^{TE+} = [-\hat{\mathbf{x}}'jk_{y'} + \hat{\mathbf{y}}'jk_{x'}]e^{j(k_x x' + k_y y') + \gamma_0 z'} , \qquad (3.54a)$$

$$\mathbf{E}_{t0}^{TM+} = \frac{\gamma_0}{j\omega\varepsilon_0}[\hat{\mathbf{x}}'jk_{x'} + \hat{\mathbf{y}}'jk_{y'}]e^{j(k_x x' + k_y y') + \gamma_0 z'} . \qquad (3.54b)$$

Applying the coordinate transformation (Eq. (3.2)),

$$\mathbf{E}_{t0}^{TE+} = \hat{\mathbf{y}} [-jk_{y'} \sin\phi - jk_{x'} \cos\phi]e^{jk_x x - \gamma_0 z} , \qquad (3.55a)$$

$$\mathbf{E}_{t0}^{TM+} = \hat{\mathbf{x}} \frac{\gamma_0}{j\omega\varepsilon_0}[jk_{x'} \cos\phi + jk_{y'} \sin\phi]e^{jk_x x - \gamma_0 z} , \qquad (3.55b)$$

where

$$k_x = k_x \cos\phi + k_y \sin\phi ,$$

$$k_y = 0 .$$

As before, the primed variables x', y', z' refer to the original coordinate system, and the unprimed variables x, y, z refer to the rotated coordinate system. Second, translate the fields problem into an equivalent transmission-line problem by assigning a characteristic

impedance Z_{0i}^p and propagation constant γ_i to each layer, where the polarization $p = $ TE or TM.

$$\gamma_i = \sqrt{\alpha^2 + \beta^2 - \varepsilon_{ri} k_0^2} \ ,$$

$$Z_{0i}^{\text{TE}} = \frac{-E_y}{H_x} = \frac{j\omega\mu_0}{\gamma_i} \ ,$$

$$Z_{0i}^{\text{TM}} = \frac{E_x}{H_y} = \frac{\gamma_i}{j\omega\varepsilon_{ri}\varepsilon_0} \ .$$

Third, alternating between $\Gamma(z)$ and $Z(z)$ from the load end of the transmission line to the source end, calculate the generalized reflection coefficient at each interface. Remember that although $V(z)$, $I(z)$, and $Z(z)$ are continuous at the interfaces, $\Gamma(z)$ is not. For the two-layer example introduced in Sec. 3.1,

$$Z_p^+ = Z_{02}^p \frac{Z_{02}^p + Z_{00}^p \coth\gamma_2 t_2}{Z_{00}^p + Z_{02}^p \coth\gamma_2 t_2} \ ,$$

$$Z_{in}^p = Z_{01}^p \frac{Z_{01}^p + Z_p^+ \coth\gamma_1 t_1}{Z_p^+ + Z_{01}^p \coth\gamma_1 t_1} \ ,$$

$$\Gamma_1^p(0) = \frac{Z_p^+ - Z_{01}^p}{Z_p^+ + Z_{01}^p} \ ,$$

$$\Gamma_1^p(-t_1) = \frac{Z_{in}^p - Z_{01}^p}{Z_{in}^p + Z_{01}^p} \ ,$$

$$\Gamma_0^p(-t_1) = \frac{Z_{in}^p - Z_{00}^p}{Z_{in}^p + Z_{00}^p} \ .$$

Since $E_y^{\text{TE}} \leftrightarrow -V$ and $E_x^{\text{TM}} \leftrightarrow +V$, the complex amplitude of the incident voltage wave V_0^+ is given by

$$V_0^{\text{TE}+} = jk_{y'}\sin\phi + jk_{x'}\cos\phi \ , \qquad (3.56a)$$

$$V_0^{\text{TM}+} = \frac{\gamma_0}{j\omega\varepsilon_0}[jk_{x'}\cos\phi + jk_{y'}\sin\phi] \ . \qquad (3.56b)$$

Fourth, compute the voltage in each region beginning at the source end of the transmission line. For the two-layer example, in region 0,

$$V^p(-t_1) = V_0^{p+}e^{\gamma_0 t_1}[\ 1 + \Gamma_0^p(-t_1)\ ] \ . \qquad (3.57)$$

In region 1,

$$V_1^{p+} = \frac{V^p(-t_1)e^{-\gamma_1 t_1}}{1 + \Gamma_1^p(-t_1)} \ , \qquad (3.58)$$

$$V^p(0) = V_1^{p+}[\ 1 + \Gamma_1^p(0)\ ] \ . \qquad (3.59)$$

Fifth, make the association from voltage back to the electric field,

$$E_{y0}^{\text{TE}} = -V^{\text{TE}}(0) \ , \qquad (3.60a)$$

$$E_{x0}^{\text{TM}} = +V^{\text{TM}}(0) \ , \qquad (3.60b)$$

and sixth, rotate back to the original coordinate system:

$$\mathbf{E}_t^{inc}(x',y') = [\ \hat{\mathbf{x}}'\sin\phi - \hat{\mathbf{y}}'\cos\phi]E_{y0}^{\text{TE}}\ e^{j(k_x x' + k_y y')}, \ \ \text{TE inc.,} \qquad (3.61a)$$

$$\mathbf{E}_t^{inc}(x',y') = [\ \hat{\mathbf{x}}'\cos\phi + \hat{\mathbf{y}}'\sin\phi]E_{x0}^{\text{TM}}e^{j(k_x x' + k_y y')}, \ \ \text{TM inc.} \qquad (3.61b)$$

This completes the derivation of the incident field.

CHAPTER 4

THEORETICAL AND NUMERICAL CONSIDERATIONS

Before the equations developed in the previous chapter can be implemented on the computer, there are a number of points that must be considered.

4.1 General Characteristics of the Inner Products Arising in the Analysis of Finite Frequency Selective Surfaces

If a function $\mathbf{j}_{j0}(x,y)$ is shifted relative to the origin by an amount (x_j,y_j), where $\mathbf{j}_j(x,y) = \mathbf{j}_{j0}(x-x_j,y-y_j)$, then the Fourier transforms of the two functions are related by the translation property of the Fourier transform. Modifying the notation slightly so that $\tilde{\mathbf{j}}_{j0}(\alpha,\beta)$ is real, the Fourier transform of $\mathbf{j}_j(x,y)$ can be expressed in the form,

$$\tilde{\mathbf{j}}_j(\alpha,\beta) = K_j \tilde{\mathbf{j}}_{j0}(\alpha,\beta)\, e^{-j\alpha x_j} e^{-j\beta y_j}\,, \tag{4.1}$$

where K_j is a complex constant. If the original function was either real and even or real and odd, $\tilde{\mathbf{j}}_{j0}(\alpha,\beta)$ will be either real and even or real and odd. This is true for the vast majority of basis and testing functions used in practice, one exception being the traveling-wave expansion used in the analysis of electrically-large bodies.

If the current density on a finite-width two-dimensional surface, for example, is discretized using entire-domain basis functions, such that $y_j = 0$ for all j, then substituting representation (4.1) into Eq. (3.47), the matrix element Z_{ij} is given by

$$Z_{ij} = \frac{-K_i^* K_j}{2\pi T_y} \sum_{n=-\infty}^{\infty} \int_{-\infty}^{\infty} \tilde{\mathbf{j}}_{i0}^{\mathrm{T}}(\alpha,\beta_n)\, \tilde{G}(\alpha,\beta_n)\, \tilde{\mathbf{j}}_{j0}(\alpha,\beta_n)\, e^{j\alpha x_{ij}} d\alpha \tag{4.2}$$

where $x_{ij} = x_i - x_j$, and the superscript "T" signifies transpose. Since $\tilde{\mathbf{j}}_{i0}(\alpha,\beta)$ is real, the complex conjugate appears only on the complex constant K_i and on the phase shift term $e^{-j\alpha x_i}$.

If $\varphi(\alpha)$ is defined as the product $\tilde{\mathbf{j}}_{i0}^T(\alpha,\beta)\tilde{\mathbf{G}}(\alpha,\beta_n)\tilde{\mathbf{j}}_{j0}(\alpha,\beta_n)$, which is a complex-valued, scalar function of α, except for isolated singularities due to the Green's function (which is the subject of the next section), $\varphi(\alpha)$ is relatively smooth. The term $e^{j\alpha x_{ij}}$, on the other hand, which depends on the separation between the basis and testing functions, can be highly-oscillatory, and in general, the greater the distance between a pair of basis and testing functions, the higher the oscillation. A plot of the integrand is shown in Fig. 4.1 for a finite strip grating whose current density flowing perpendicularly to the strips has been discretized with triangular basis functions with a half width Δ of $\lambda/10$.
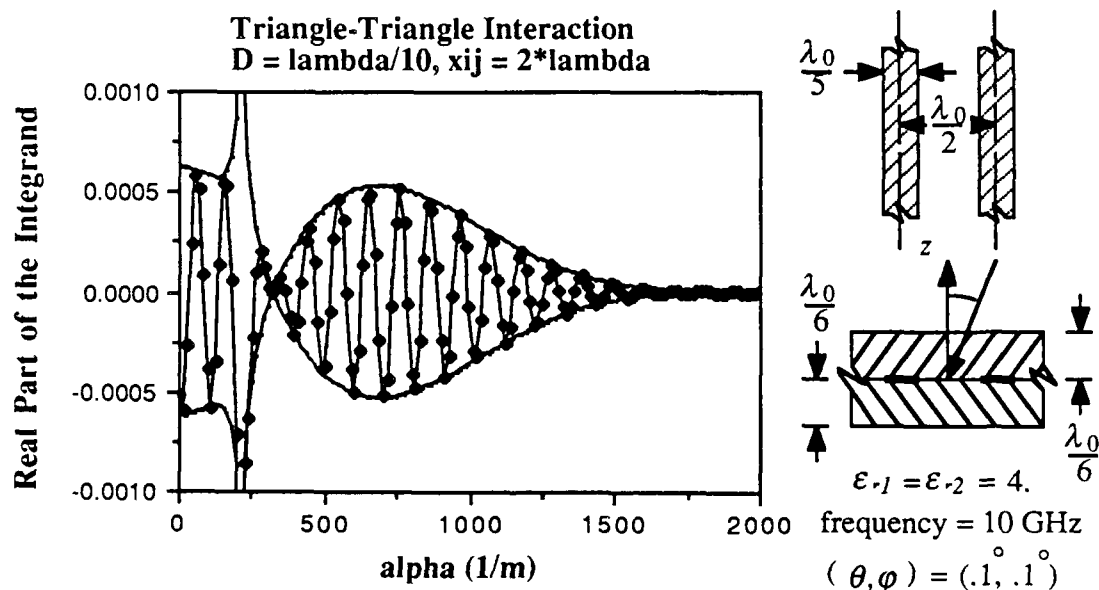

Figure 4.1. Plot of the integrand representing the mutual coupling between two x-directed triangular currents separated by $2\lambda_0$.

If the rate of oscillation is high enough relative to the variation of $\varphi(\alpha)$, in the integral, each positive half cycle of the integrand will cancel an adjacent negative half cycle of the function, making the result zero, or nearly zero. This intuitive observation is stated

mathematically in the Riemann-Lebesgue Lemma [13], which says, if $\varphi(\alpha)$ is absolutely integrable on an interval (a,b), then

$$\lim_{x_{ij}\to\infty} \int_a^b \phi(\alpha)\, e^{-j\alpha x_{ij}} d\alpha = 0 \,,$$

where a and b are finite or infinite constants. It is not necessary for $\varphi(\alpha)$ to have a bounded derivative for the above result to hold.

A sufficient condition to guarantee that $\varphi(\alpha)$ is absolutely integrable is that each dielectric layer be slightly lossy. Otherwise, the integrand will contain non-integrable singularities corresponding to unattenuated guided modes in the dielectric-slab waveguide.

The following conclusions are deducible from the above premises. (1) If the dielectric layers have some loss, however small, the mutual coupling between FSS elements will become negligibly small as their separation increases. This suggests, (2) that beyond a certain separation, it will be possible to neglect the direct mutual coupling between two elements in the array. In very large arrays, it is only necessary to calculate the mutual coupling between one element and a finite number of its nearest neighbors. The remaining terms will be negligible by comparison and may be set to zero without introducing significant error.

The coupling distance, or maximum separation for which direct mutual coupling must be taken into account, depends on the parameters of the dielectric support. If the dielectrics are extremely lossy, for example, the fields produced by one element will attenuate rapidly away from the source and will have little direct effect on the currents induced on a distant element of the array. If the elements are part of a free-standing surface, numerical experiments have shown that if the x and y periodicities are roughly equal to $\lambda/2$, significant mutual coupling exists only between elements that are less than about seven periods apart. For surfaces supported by dielectric layers, or backed by perfectly-conducting ground planes, the coupling distance will be somewhat higher.

A third conclusion deducible from the above premises is the following: for distant interactions, the dominant coupling mechanism is the guided modes in the dielectric layers. If x_{ij} is large but not infinite, over intervals where $\varphi(\alpha)$ is relatively smooth, as already shown, the factor $e^{j\alpha x_{ij}}$ will cause cancellation to occur in the evaluation of the integrals. For large distances x_{ij}, therefore, significant contributions to the inner products will occur when $\varphi(\alpha)$ is singular or sharply peaked. These features are associated with the guided modes in the dielectric-slab waveguide.

4.2 Singularities of the Spectral Green's Function

The analysis of periodic structures by the spectral-domain method calls for sampling the product of the Green's function, basis, and testing functions, in the Fourier-transform domain, at the transverse wave numbers α_m, β_{mn} of the Floquet space harmonics. These are represented graphically by the intersections of the grid lines in the reciprocal lattice of Fig. 4.2. Since the frequency, permittivities, thicknesses, periodicities, and incident angles are chosen independently, it is unlikely that the Green's function will be sampled at one of its singular points, represented by the concentric circles in Fig. 4.2. However, in the unlikely event that this does happen, any of the above parameters, for example the incident angles, can be adjusted by a small amount to shift either the locations of the singularities or the locations of the sample points (α_m, β_{mn}) to avoid sampling directly on a singularity of the Green's function.

For a frequency selective surface of finite width, the formulation calls for a number of integrations to be performed along the diagonal lines $\beta_n = \dfrac{2\pi n}{T_{\eta 2}\sin\Omega} - (\alpha - k_x)\cot\Omega + k_y$, labeled $n = 0, \pm 1, \pm 2, \ldots$ in Fig. 4.2. For free-standing surfaces, the free-space Green's function will contribute an integrable singularity to the integrand at $k_\rho^2 = k_0^2$. In this case, the function can be integrated with a judicious choice of a numerical integration routine. If the printed surface is deposited on the surface of one or more lossless dielectric layers, for
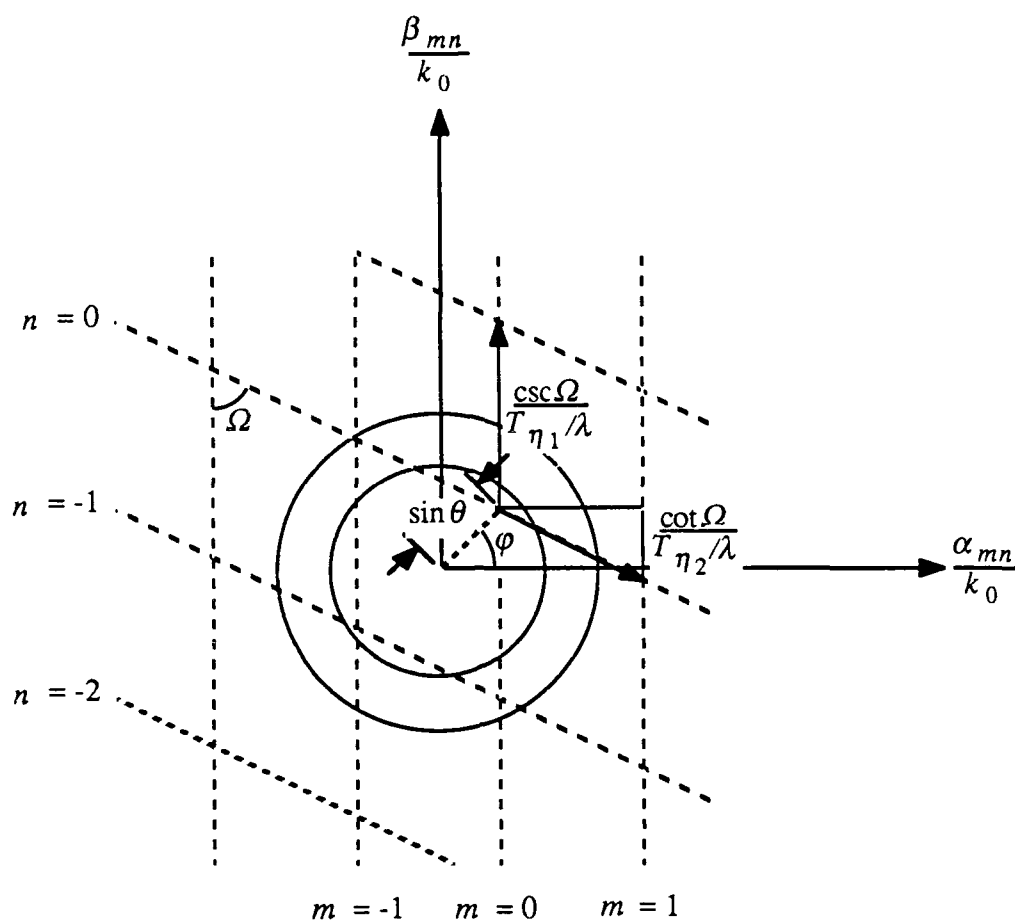
Figure 4.2. Reciprocal lattice for periodic surfaces.

α real, at least one integration will pass through a non-integrable singularity of the Green's function. Viewing the situation in the complex-α plane, the path of integration is along the real-α axis, where a number of singularities are encountered for a small number of integrations around $n = 0$ (Fig. 4.3(a)).

There are at least two methods of handling the singularities [25]. If the dielectric layers are assumed to be slightly lossy, the singularities migrate off the path of integration as shown in Fig. 4.3(b), and there is no longer any theoretical difficulty in performing the integrations. This is not usually an inconvenience, since all physical materials have some loss. However, the lossless situation can be considered in the limit as the loss tends to
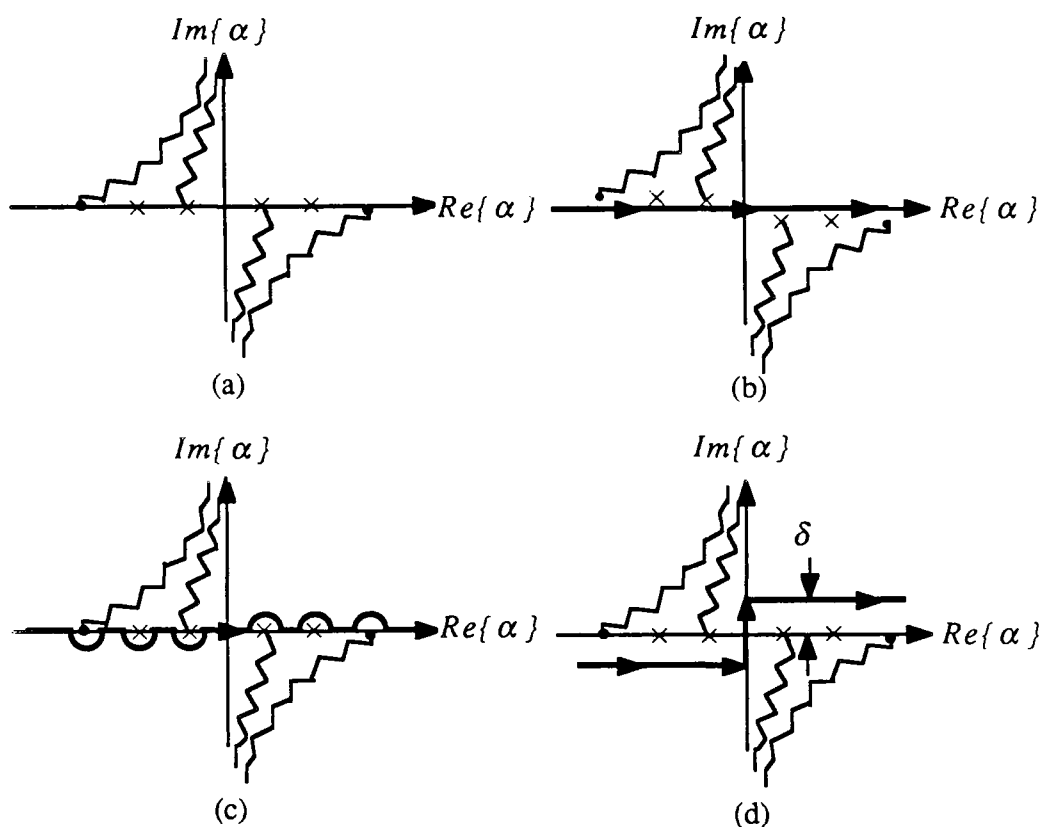
Figure 4.3. Complex-α plane:

(a) singularities of the spectral Green's function for a lossless dielectric, assuming one guided mode is supported in the dielectric (time convention: $e^{j\omega t}$).

(b) locations of the singularities assuming the dielectric has a small amount of loss.

(c) contour of integration obtained by considering the lossless case as the zero-loss limit of (b),

(d) rectilinear path obtained by deforming the contour of (c).

zero, as long as the contour of integration is defined in such a way as to encircle the singularities in a manner which is consistent with the lossy case (Fig. 4.3 (c)). However, since the locations of the singularities can only be determined numerically, and since the contour can be deformed through any analytic region of the function, it is more convenient to integrate along a rectilinear path as shown in Fig. 4.3 (d).

Both of these methods were found to be successful means of handling the singularities. Contour integration may offer some advantages in terms of efficiency. If the distance δ from the path of integration to the singularities is varied as a parameter, then the greater the distance, the smoother the integrand, and the fewer number of points are required to integrate the function to the same accuracy. In Table 4.1, a typical integral arising in the study of the finite strip grating is evaluated by the contour integration method, for various values of δ. The current density flowing parallel to the axis of the strips has been discretized using pulse basis functions. The dominant self-interaction term is evaluated using an adaptive numerical integration routine that automatically adjusts the sampling rate in order to accommodate for changes in the smoothness of the function. Table 4.1 shows the number of function evaluations required to achieve the same relative accuracy of 0.1 per cent. As indicated in the table, the least number of function evaluations is exactly one third of the greatest number.

Table 4.1. Number of function evaluations required to integrate a function to the same relative accuracy using the contour integration method.

$\dfrac{-W^2}{2\pi}\displaystyle\int_{\frac{-4\pi}{W}-j\delta}^{\frac{+4\pi}{W}+j\delta}\widetilde{G}_{yy}(\alpha,k_y)\,\mathrm{sinc}^2(\frac{\alpha W}{2})d\alpha$	δ	NPTS
$(0.29138 - j0.39950)*10^{-1}$	$0.01k_0$	1140
$(0.28941 - j0.39567)*10^{-1}$	$0.05k_0$	820
$(0.28835 - j0.39399)*10^{-1}$	$0.10k_0$	420
$(0.29077 - j0.39677)*10^{-1}$	$0.20k_0$	380

frequency = 5.625 GHz $(\theta,\varphi) = (0.5°,0.5°)$
pulse width $W = 0.029775\lambda_0$
two identical dielectric layers: $t_1,t_2 = 0.09375l_0$ $\varepsilon_{r1},\varepsilon_{r2} = (4 - j0)$

The results of Table 4.1 suggest that it may be possible to find an optimum path which would require a minimum of computational effort. Kong and Shen [26], to find the fields of an antenna submerged in a dissipative dielectric medium, define vertical branch cuts which are actually the steepest-descent paths for a particular configuration of transmitting and receiving antennas. Since the integrand is exponentially decaying in the direction perpendicular to the real-α axis, it can be integrated using only a few evaluations of the function.

The finite FSS will require considerably more integration time, but the considerations are identical to those in this case.

4.3 Numerical Integration

As was shown in previous chapters, the spectral-domain formulation of the method of moments applied to the analysis of finite frequency-selective surfaces leads to a number of integrals involving the Fourier transforms of the Green's function, basis, and testing functions. Because of the complexity of the integrands, the integrals cannot be evaluated exactly and some method of numerical integration must be employed.

An intelligent choice of a numerical integration scheme depends on the nature of the integrand. Integrals with special difficulties such as infinite ranges of integration, singularities, or highly-oscillatory integrands should be treated in special ways, developing specific automatic routines tailored for each type of difficulty. "The programmer," according to Davis and Rabinowitz, is "in the position of the sportsman who has given up worms but now must know which fly to use to catch his fish" [27]. A poor choice could lead to excessive computation time or give erroneous results.

The integrands encountered in the spectral-domain method of moments have all of the above difficulties associated with them. First, in the lossless limit, for $k_\rho^2 \leq \varepsilon_{rmax} k_0^2$, the integrands have a number of isolated singularities. There are branch points where the phases of the propagation constants γ_i are discontinuous and singularities caused by zeros

in the denominators of the input impedances Z_{in}^{TE} and Z_{in}^{TM}. Even if the singularities are avoided either by introducing a small loss into each region or by deforming the path of integration into the complex plane, the integrands will still vary rapidly in the vicinities of the singularities. Second, interactions between basis and testing functions which are separated by a few periods are characterized by highly-oscillatory integrands. As the distance between a pair of basis and testing functions increases, the rate of oscillation increases proportionately. Third, the limits of integration are infinite.

Of the three, the singularities are considered to be the most serious difficulty. The oscillation is manageable for arrays with moderate dimensions, while for large arrays, the integrations can be confined to the regions around the poles. If the integrand has a certain minimum asymptotic rate of decay, the limits of integration can be truncated to finite values and the integral evaluated over the finite interval.

The sampling rate in numerical integration is determined by the number of points necessary to represent the integrand in a given region. For $k_\rho^2 \leq \varepsilon_{rmax} k_0^2$, the sampling rate is dominated by the presence of the singularities. Outside this region, the oscillatory behavior of the integrand dominates. Because the integrand has two regions dominated by different behaviors, because the integrand contains a number of singularities, and because the locations of these singularities can only be determined numerically, an adaptive numerical integration routine that automatically adjusts the sampling rate to accommodate for changes in the smoothness of the integrand is a natural choice.

The advantage of such a scheme is that the integrand is sampled heavily only in regions where the function is varying most rapidly. If, over a given interval, the integrand is relatively smooth, the sampling rate is automatically reduced to a minimum. The algorithm is also capable of handling singularities. Davis and Rabinowitz report that an adaptive routine based on Simpson's rule has been used to successfully integrate $1/\sqrt{|x|}$ through zero. Hillstrom [28] has done some numerical experiments that indicate that if the

integrand is sharply peaked, or if great accuracy is desired, a high-order adaptive routine is most efficient.

Many variations of adaptive integration have been proposed in the literature. Rice, who is quoted by Davis and Rabinowitz, has studied the subject in detail and estimates that there are about a million adaptive quadrature algorithms which are potentially reasonable and interesting. While a complete discussion of the subject would be out of place here, the essential features of adaptive integration are embodied in the following example.

On a given interval, the function is first integrated using a previously-chosen fundamental integration rule. The interval is then halved and the same rule is applied to each of the two subintervals. If the result of integrating over the two subintervals is within a specified tolerance of the result for the total interval, the result of the two integrations is accepted, and a new interval is selected for the next iteration. If the result of the two integrations does not fall within the allowable tolerance, one of the two subintervals is selected as the total interval for the next iteration, and the process is repeated. For example, if NC_n is the result of applying an n-point Newton-Cotes integration rule over $[a,b]$, and $2 \times NC_n$ is the result of applying the same rule to each of the two subintervals, then, if

$$| 2 \times NC_n - NC_n | < \varepsilon | 2 \times NC_n | , \qquad (4.3)$$

the result $2 \times NC_n$ is accepted as the value of the integral over $[a,b]$. Otherwise, each of the subintervals is treated as the original interval using $\varepsilon/\sqrt{2}$ as the pro-rated error tolerance, since $\varepsilon/2$ is usually too strict in practice. The actual error is usually much less than ε.

The choice of an integration rule to be used as the basis for an adaptive algorithm depends on a number of considerations. The theory of approximate quadratures depends on replacing the integral $\int_a^b f(x)dx$ by another integral $\int_a^b \varphi(x)dx$, where $\varphi(x)$ can be determined in a simple way [29]. The function $\varphi(x)$ is expressed as a series of weighted orthogonal functions over $[a,b]$; then $\varphi(x)$ is integrated exactly to obtain an approximation to the desired integral. If the integrand is sampled at the $(n + 1)$ points $y_0, y_1, ..., y_n$, the result of the integration can be expressed in the form

$$\int_a^b \phi(x)\, dx = A_0 y_0 + A_1 y_1 + \ldots + A_n y_n , \qquad (4.4)$$

where the $(n + 1)$ constants A_m are independent of the $(n + 1)$ abscissas y_m. In the Newton-Cotes-type formulas, the points y_m are fixed. It follows that if $f(x)$ is a polynomial of degree $\leq n$, the error in integrating $\varphi(x)$ can be made to vanish by the proper choice of the A_m's. In Gauss's method, both the sample points y_m and weights A_m are determined in such a way that the difference between $\int f(x)dx$ and $\int \varphi(x)dx$ is a minimum. Since there are now $(2n + 2)$ available constants, an $(n + 1)$-point Gaussian-quadrature formula is capable of integrating exactly a polynomial of degree $\leq 2n + 1$. Thus, for the same relative accuracy, a Gaussian-quadrature formula requires fewer points, or, for a given number of sample points, a Gaussian-quadrature formula is more nearly exact than the corresponding Newton-Cotes formula.

Integration rules based on equally spaced abscissas, such as the Newton-Cotes-type formulas, have the advantage that as each interval is halved, only half of the function values need to be computed, since the other half is available from a previous iteration. Many high-order Newton-Cotes rules contain weights of opposite signs, which, because of finite word length, could result in a loss of accuracy. Newton-Cotes rules based on an even number of points have rarely been used in practice, since they are generally less accurate than the next lower order rule of the same type, which can be verified by examining the error expressions given by Abramowitz and Stegun [30]. A notable exception to this is the trapezoidal rule.

As stated before, Hillstrom has shown, by numerical experiment, that if the integrand is sharply peaked, or if great accuracy is desired, an adaptive high-order rule is most efficient. Hillstrom's experiments were repeated using the adaptive procedure outlined in this section. Adaptive algorithms ANC3, ANC7, and ANC11, based on 3, 7, and 11-point Newton-Cotes formulas, were applied to two different test integrals having sharply peaked or singular integrands. ANC3 is an adaptive Simpson's rule, which is the minimum-

degree rule used adaptively in practice. ANC7 is based on a 7-point Newton-Cotes rule, which is the highest-degree rule based on an odd number of points with all positive weights, and ANC11 is based on the highest-degree rule given by Abramowitz and Stegun [30].

Each of the routines was required to integrate the same function to the same relative accuracy ε, and each was limited to the same minimum sampling interval, which was chosen to be approximately $2/10^6$. If convergence had not been achieved at this point, the most accurate estimate was accepted as the value of the integral over that subinterval and the process was allowed to continue. An algorithm is considered most efficient if it requires the least number of functional evaluations to obtain the result.

The first integral is of the form $\int_{-1}^{1}(x^2 + p^2)^{-1} dx$, where p is a parameter. For small p, the integrand has a peak of height p^{-2} at the origin and is approximately equal to one at the endpoints. Table 4.2 shows the number of function evaluations required by each routine to achieve the same relative accuracy. Results are also provided for the popular ROMBERG integration method, to highlight the advantages of using adaptive integration for sharply peaked integrands.

Although the adaptive algorithms described here, and in particular the convergence criterion, are somewhat different from those implemented by Hillstrom, the results are very similar. The "best" integration rule to use in an adaptive scheme depends both on the desired accuracy and on the smoothness of the integrand. If extreme accuracy is desired, an adaptive routine built on a high-order rule is most efficient; but if two or three digits of accuracy is sufficient, for the range of the parameters tested, an adaptive routine built on a moderately high-order Newton-Cotes formula ANC7 is most efficient. The comparison with the results of the ROMBERG algorithm is striking.

Table 4.2. Comparison of several adaptive quadrature routines for integrating sharply-peaked functions of the form $(x^2 + p^2)^{-1}$.

$p = 10^{-2}$		$p = 10^{-3}$		$p = 10^{-4}$	
$\varepsilon = .01$		$\varepsilon = .01$		$\varepsilon = .01$	
ROMBERG	513	ROMBERG	8193	ROMBERG	65537
ANC3	129	ANC3	249	ANC3	401
ANC7	169	ANC7	265	ANC7	337
ANC11	241	ANC11	241	ANC11	521
$\varepsilon = .001$		$\varepsilon = .001$		$\varepsilon = .001$	
ROMBERG	1025	ROMBERG	8193	ROMBERG	65537
ANC3	273	ANC3	481	ANC3	769
ANC7	169	ANC7	265	ANC7	361
ANC11	241	ANC11	401	ANC11	561
$\varepsilon = 10^{-4}$		$\varepsilon = 10^{-4}$		$\varepsilon = 10^{-4}$	
ROMBERG	2049	ROMBERG	16385	ROMBERG	262145
ANC3	481	ANC3	929	ANC3	1449
ANC7	193	ANC7	385	ANC7	577
ANC11	281	ANC11	441	ANC11	561
$\varepsilon = 10^{-5}$		$\varepsilon = 10^{-5}$		$\varepsilon = 10^{-5}$	
ROMBERG	2049	ROMBERG	32769	ROMBERG	262145
ANC3	977	ANC3	1793	ANC3	2561
ANC7	361	ANC7	505	ANC7	793
ANC11	281	ANC11	441	ANC11	601
$\varepsilon = 10^{-6}$		$\varepsilon = 10^{-6}$		$\varepsilon = 10^{-6}$	
ROMBERG	4097	ROMBERG	65537	ROMBERG	524289
ANC3	1897	ANC3	3425	ANC3	4409
ANC7	409	ANC7	721	ANC7	1009
ANC11	321	ANC11	481	ANC11	721

A second type of difficulty encountered in the analysis of finite frequency selective surfaces is an integrable singularity of the type $1/\sqrt{x^2 - 1}$. This type of singularity is present in the transform-domain expression for the free-space Green's function, Eqs. (3.3) and (3.26). At the singular points, $x = \pm 1$, the magnitude of the integrand becomes unbounded, while the function reverses from real to imaginary and vice versa. This function can be integrated exactly to give

$$\int_{-L}^{L} \frac{dx}{\sqrt{x^2 - 1}} = 2 \ln\left(L + \sqrt{L^2 - 1}\right) - j\pi \quad (L \geq 1). \tag{4.5}$$

This integral was evaluated using the same adaptive quadrature schemes as before. The results are summarized in Table 4.3. Of the routines tested, for $0.01 \leq \varepsilon \leq 0.005$, the adaptive Simpson's rule was most efficient; for $0.002 \leq \varepsilon \leq 0.0001$, the adaptive 7-point rule was most efficient. As in the first example, for extremely tight error bounds, say $\varepsilon < 10^{-5}$, the higher-order rule ANC11 is expected to become more efficient than the lower-order rules ANC3 and ANC7.

These conclusions are based on the performance of integration rules with evenly-spaced abscissas. The question remains as to whether there is any advantage in using an integration rule with non-equally-spaced abscissas, such as the Gauss-type formulas. Chugh and Shafai, for example, report that an iterative nonadaptive algorithm built on an 11-point Gauss-Legendre integration rule was more accurate and more efficient than the popular ROMBERG integration method at handling a particular two-dimensional phase integral arising in electromagnetics [31].

The fact that the abscissas are unequally-spaced makes an adaptive Gaussian-quadrature algorithm particularly robust. When a given interval is bisected, since the abscissas are, for example, given by the zeros of Legendre polynomials, none of the sample points coincide with previous values, and subsequent integrals are based on entirely

Table 4.3. Comparison of several adaptive quadrature routines for integrating a singularity of the form $1/\sqrt{x^2 - 1}$.

$\varepsilon = .01$		$\varepsilon = .005$		$\varepsilon = .002$	
ROMBERG	8193	ROMBERG	131073	ROMBERG	524289
ANC3	497	ANC3	569	ANC3	721
ANC7	553	ANC7	625	ANC7	673
ANC11	681	ANC11	721	ANC11	841
$\varepsilon = .001$		$\varepsilon = .0005$		$\varepsilon = .0002$	
ROMBERG	524289	ROMBERG	1048577	ROMBERG	1048577
ANC3	881	ANC3	1009	ANC3	1225
ANC7	721	ANC7	769	ANC7	889
ANC11	881	ANC11	881	ANC11	921
$\varepsilon = .0001$					
ROMBERG	1048577				
ANC3	1457				
ANC7	889				
ANC11	1001				

different values of the function. If the convergence criterion is satisfied under these conditions, the result is especially reliable.

However, the source of all the advantages of using a Gaussian-quadrature formula in an adaptive routine is also the cause of its main disadvantage. Since, in general, no two abscissas coincide, all previous function evaluations are discarded in the next stage of refinement. The overall efficiency of an adaptive Gaussian-quadrature routine, relative to a comparable Newton-Cotes routine, will therefore depend on the relative importance of the following considerations: (1) the number of points used in actually evaluating the integral is expected to be somewhat less for an adaptive Gaussian-quadrature routine, but (2) the

cost of determining these points, which is equal to the cost of discarding all previous function values, may be prohibitive. Clearly, the second factor depends on the complexity of the particular integrand being considered. As the integrand becomes more difficult to compute, the added computation time due to calculating and then discarding previous function values will eventually outweigh, then overwhelm, the time saved in using a more accurate integration rule. Unfortunately, there is no way to determine the complexity of the integrand where this transition occurs.

A numerical experiment was conducted in order to determine the efficiency of an adaptive Gaussian-quadrature routine relative to a comparable Newton-Cotes routine for a particular integral arising in the analysis of the finite strip grating. Since Gaussian-quadrature formulas are open type, i.e., since the function is not evaluated at the endpoints of the interval, a 10-point Gauss-Legendre rule was compared to an 11-point Newton-Cotes rule. In order to integrate a function of this complexity, the adaptive Gaussian-quadrature routine required from two to three times as long as the comparable Newton-Cotes algorithm.

4.4 Symmetry

The input impedances Z_{in}^{TE} and Z_{in}^{TM} that are used in the derivation of the spectral-domain Green's function are functions of $\alpha^2 + \beta^2$ only, and are, therefore, even functions of both variables. According to Eqs. (3.19)-(3.21), $\tilde{G}_{xx}$ and $\tilde{G}_{yy}$ are, therefore, even functions of α and β, while $\tilde{G}_{xy}$ is an odd function of both variables. Since nearly all of the basis and testing functions used in practice are either even or odd, their Fourier transforms are either even or odd as well. In this section, we will investigate under what conditions symmetry can be used to reduce a two-dimensional summation or integration over the infinite α-β plane to a summation or integration over the half plane $\alpha \geq 0$ or the quarter plane $\alpha \geq 0$, $\beta \geq 0$, reducing the total number computations to one half or one quarter of its original value.

To take advantage of symmetry, the integrand or summand must be evaluated at symmetrical points $(\pm\alpha, \pm\beta)$. Referring to Fig. 4.2, it is clear that for the periodic FSS, the sample points of the summand are not symmetrical, in general, about either axis, and symmetry cannot be used except in special cases. If the skew angle Ω is equal to $90°$ and the incident angle φ is zero, then the sample points of $\widetilde{G}$, $\widetilde{j}_i$, and $\widetilde{j}_j$, $\beta_n = \frac{2\pi n}{T_y}$, $n = 0, \pm 1$, $\pm 2, ...,$ will be symmetrical with respect to the α axis, and the computation time in filling the moment matrix would be reduced by approximately one half. If, in addition, $\theta = 0$, then the sample points $\alpha_m = \frac{2\pi m}{T_x}$, $m = 0, \pm 1, \pm 2, ...,$ would also be symmetrical about the β axis, allowing the number of computations to be further reduced to approximately one fourth the original number. However, if the incident field is derived from the magnetic and electric vector potentials, Eqs. (2.1)-(2.2), the field for $(\theta, \varphi) = (0,0)$ is not defined.

On the other hand, if the problem of interest is a frequency selective surface of finite width, rather than summations at the discrete points (α_m, β_{mn}), the formulation calls for integrations along the diagonal lines $\beta_n = \frac{2\pi n}{T_{\eta 2}\sin\Omega} - (\alpha - k_x)\cot\Omega + k_y$, shown in Fig. 4.2. As in the periodic case, generally the integrands are not evaluated at symmetrical points and symmetry cannot be used. However, there are numerous practical situations, less restrictive than in the periodic case, where symmetry can be used. If $\Omega = 90°$, then the lines of integration, $\beta_n = \frac{2\pi n}{T_{\eta 2}} + k_y$, are horizontal, and the even/odd character of the integrands with respect to α can be used to decrease computation time by one half. This is true for the strip grating, for example, and for a large number of other geometries used in practice. If, in addition, $\varphi = 0$, then $k_y = 0$, and the lines of integration will be located symmetrically about the α axis, allowing another factor of two reduction in computation time.

For the finite-FSS problem, which requires a full two-dimensional integration over the infinte α-β plane, if the basis and testing functions are real and either even or odd, symmetry can always be used to reduce the region of integration to the quarter plane $\alpha \geq 0$, $\beta \geq 0$.

4.5 Translation, Reciprocity, and Parallel Matrix Fill

The analysis of finite frequency selective surfaces by the spectral-domain method of moments requires an enormous amount of computation time unless careful consideration is given to the efficient computation of the matrix elements. It has already been shown that a judicious choice of a numerical integration technique can mean an order of magnitude speedup in generating the moment matrix. Equally significant is the computation time saved by eliminating redundant calculations. If the current density on a finite-width FSS is discretized with entire-domain basis functions whose unshifted versions are real and either even or odd, then the matrix element Z_{ij} can be expressed in the form

$$Z_{ij} = \frac{-K_i^* K_j}{2\pi T_y} \sum_{n=-\infty}^{\infty} \int_{-\infty}^{\infty} \tilde{\mathbf{j}}_{i0}^T(\alpha,\beta_n) \, \tilde{\mathbf{G}}(\alpha,\beta_n) \, \tilde{\mathbf{j}}_{j0}(\alpha,\beta_n) \, e^{j\alpha x_{ij}} \, e^{j\beta_n y_{ij}} \, d\alpha \ ,$$

where K_i and K_j are complex constants, $\tilde{\mathbf{j}}_{i0}$ and $\tilde{\mathbf{j}}_{j0}$ are real, and (x_i, y_i) and (x_j, y_j) are the coordinates of the basis and testing functions relative to the origin. According to this equation, the interaction between basis function $\tilde{\mathbf{j}}_{j0}$ at position (x_j, y_j) and testing function $\tilde{\mathbf{j}}_{i0}$ at position (x_i, y_i) depends only on the distances $x_{ij} = (x_i - x_j)$ and $y_{ij} = (y_i - y_j)$. For example, if the current density on a finite-width frequency selective surface of thin linear dipoles is represented in terms of rooftop basis functions as shown in Fig. 4.4, and Galerkin's testing procedure is used, many of the interactions are identical: $Z_{11} = Z_{22}$, etc., $Z_{12} = Z_{23}$, etc., $Z_{13} = Z_{24}$, etc., $Z_{16} = Z_{27}$, etc., $Z_{17} = Z_{28}$, etc., $Z_{18} = Z_{29}$, etc.

If the basis functions are numbered as in Fig. 4.4 and arranged in a vector, the resulting matrix $\mathbf{Z}$ will have two levels of Toeplitz structure, as indicated in Fig. 4.5. The full matrix will be a block-Toeplitz matrix, and each Toeplitz block will itself be a Toeplitz matrix, i.e., the independent elements of $\mathbf{Z}$ lie in the first row and column of the blocks $\mathbf{B}_{kl}$, and the remaining elements are obtained by copying these elements parallel to the main diagonal. The result is that instead of computing $(NI_0)^2$ matrix elements, where N is the number of elements in a unit row and I_0 is the number of basis functions per element, it is

Figure 4.4. Rooftop approximation for the current on a finite-width array of thin dipoles.

$$
\begin{bmatrix}
\begin{bmatrix} Z_{1,1} & Z_{1,2} & Z_{1,3} & Z_{1,4} & Z_{1,5} \\ Z_{2,1} & & & & \\ Z_{3,1} & & & & \\ Z_{4,1} & & & & \\ Z_{5,1} & & & & \end{bmatrix}
& \begin{bmatrix} Z_{1,6} & Z_{1,7} & Z_{1,8} & Z_{1,9} & Z_{1,10} \\ Z_{2,6} & & & & \\ Z_{3,6} & & & & \\ Z_{4,6} & & & & \\ Z_{5,6} & & & & \end{bmatrix}
& \begin{bmatrix} Z_{1,11} & Z_{1,12} & Z_{1,13} & Z_{1,14} & Z_{1,15} \\ Z_{2,11} & & & & \\ Z_{3,11} & & & & \\ Z_{4,11} & & & \cdot & \\ Z_{5,11} & & & & \end{bmatrix} \\[3ex]
\begin{bmatrix} Z_{6,1} & Z_{6,2} & Z_{6,3} & Z_{6,4} & Z_{6,5} \\ Z_{7,1} & & & & \\ Z_{8,1} & & & & \\ Z_{9,1} & & & & \\ Z_{10,1} & & & & \end{bmatrix}
& \mathbf{B}_{11} & \mathbf{B}_{12} \\[3ex]
\begin{bmatrix} Z_{11,1} & Z_{11,2} & Z_{11,3} & Z_{11,4} & Z_{11,5} \\ Z_{12,1} & & & & \\ Z_{13,1} & & & & \\ Z_{14,1} & & & & \\ Z_{15,1} & & & & \end{bmatrix}
& \mathbf{B}_{21} & \mathbf{B}_{11}
\end{bmatrix}
$$

Figure 4.5. Independent elements of the moment matrix $\mathbf{Z}$ for the example of Fig. 4.4, showing two levels of Toeplitz structure.

only necessary to compute the $(2N - 1)(2I_0 - 1)$ independent interactions in the first row and column of each Toeplitz block. The actual amount of computation time saved will depend on the size of the matrix.

The translation property that produced the significant savings in this example is not dependent on the details of the example. The following general conclusion is valid: if a finite frequency selective surface consists of a uniform array of identical elements, and the unknown on each element is discretized with the same set of basis functions, which are ordered in the same way and grouped according to element, the matrix $\mathbf{Z}$ will be a block-Toeplitz matrix. The second level of Toeplitz structure in this example is due to the choice of subdomain basis functions; however, this type of structure can also arise with entire-domain basis functions in the analysis of frequency selective surfaces which are finite in two dimensions.

A different matrix structure and a different type of redundancy show up in the moment matrix when the current on a finite frequency selective surface is represented in terms of entire-domain basis functions with Galerkin testing. It is easily verified that the product $\widetilde{\mathbf{j}}_{i0}^{T}\widetilde{\mathbf{G}}\widetilde{\mathbf{j}}_{j0}$ is independent of the interchange of $\widetilde{\mathbf{j}}_{i0}$ and $\widetilde{\mathbf{j}}_{j0}$, i.e., $\widetilde{\mathbf{j}}_{i0}^{T}\widetilde{\mathbf{G}}\widetilde{\mathbf{j}}_{j0} = \widetilde{\mathbf{j}}_{j0}^{T}\widetilde{\mathbf{G}}\widetilde{\mathbf{j}}_{i0}$. This suggests that the inner product is unchanged if the functional forms of the basis and testing functions are interchanged, provided the source patch and test patch remain the same. For example, if the current on a finite array of thin horizontal dipoles is represented in terms of a trigonometric series as shown in Fig. 4.6, then $Z_{12} = Z_{21}$, $Z_{13} = Z_{31}$, $Z_{23} = Z_{32}$, etc., and $Z_{15} = Z_{24}$, $Z_{16} = Z_{34}$, $Z_{26} = Z_{35}$, etc.; i.e., each Toeplitz block is symmetrical with respect to its diagonal. This property is illustrated in Fig. 4.7.
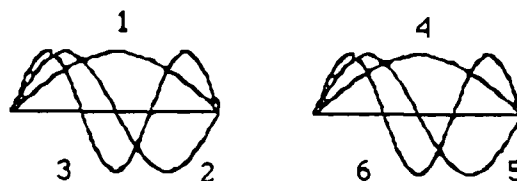
Figure 4.6. Trigonometric basis functions used in the expansion of the current on a three-element frequency selective surface of finite width.

$$\begin{bmatrix} Z_{11}Z_{12}Z_{13} \\ \cdot \ \ Z_{22}Z_{23} \\ \cdot \ \ \cdot \ \ Z_{33} \end{bmatrix} \begin{bmatrix} Z_{14}Z_{15}Z_{16} \\ \cdot \ \ Z_{25}Z_{26} \\ \cdot \ \ \cdot \ \ Z_{36} \end{bmatrix} \begin{bmatrix} Z_{17}Z_{18}Z_{19} \\ \cdot \ \ Z_{28}Z_{29} \\ \cdot \ \ \cdot \ \ Z_{39} \end{bmatrix}$$
$$\begin{bmatrix} Z_{41}Z_{42}Z_{43} \\ \cdot \ \ Z_{52}Z_{53} \\ \cdot \ \ \cdot \ \ Z_{63} \end{bmatrix} \begin{bmatrix} \cdot \ \ \cdot \ \ \cdot \\ \cdot \ \ \cdot \ \ \cdot \\ \cdot \ \ \cdot \ \ \cdot \end{bmatrix} \begin{bmatrix} \cdot \ \ \cdot \ \ \cdot \\ \cdot \ \ \cdot \ \ \cdot \\ \cdot \ \ \cdot \ \ \cdot \end{bmatrix}$$
$$\begin{bmatrix} Z_{71}Z_{72}Z_{73} \\ \cdot \ \ Z_{82}Z_{83} \\ \cdot \ \ \cdot \ \ Z_{93} \end{bmatrix} \begin{bmatrix} \cdot \ \ \cdot \ \ \cdot \\ \cdot \ \ \cdot \ \ \cdot \\ \cdot \ \ \cdot \ \ \cdot \end{bmatrix} \begin{bmatrix} \cdot \ \ \cdot \ \ \cdot \\ \cdot \ \ \cdot \ \ \cdot \\ \cdot \ \ \cdot \ \ \cdot \end{bmatrix}$$

Figure 4.7. Matrix structure for the example of Fig. 4.6, showing only the unique elements of the matrix (see text).

Under certain conditions, it is possible to make use of reciprocity. If the skew angle $\Omega = 90°$, such that the integrations in the previous example are performed along the horizontal lines $\beta_n = \frac{2\pi n}{T_{\eta 2}} + k_y$, then for the even-even interactions, Z_{13}, Z_{14}, Z_{16}, etc., K_i and K_j are real, and since $\tilde{G}_{xx}$ is an even function of α, then

$$Z_{ij} = \frac{-K_i^* K_j}{2\pi T_y} \sum_{n=-\infty}^{\infty} \int_{-\infty}^{\infty} \tilde{j}_{xi0}(\alpha,\beta_n) \ \tilde{G}_{xx}(\alpha,\beta_n) \ \tilde{j}_{xj0}(\alpha,\beta_n) \ e^{j\alpha x_{ij}} d\alpha \qquad (4.6a)$$

$$= \frac{-K_i K_j}{2\pi T_y} \sum_{n=-\infty}^{\infty} 2\int_{-\infty}^{\infty} \tilde{j}_{xi0} \ \tilde{G}_{xx} \ \tilde{j}_{xj0} \ \cos\alpha x_{ij} \ d\alpha \qquad (4.6b)$$

and, therefore, $Z_{ji} = Z_{ij}$. In this particular example, this is true regardless of the particular combination of basis and testing functions considered. Therefore, in addition to the previous reductions, it is only necessary to compute the elements above or below the main diagonal. The resultant matrix is shown in Fig. 4.8.

In addition to recognizing that many of the matrix elements are either identical or otherwise simply related, large reductions in computation time can be achieved by computing several matrix elements in parallel. Referring again to the expression for the matrix elements for a finite-width frequency selective surface,

$$\begin{bmatrix} Z_{11}Z_{12}Z_{13} \\ \cdot \ Z_{22}Z_{23} \\ \cdot \ \cdot \ Z_{33} \end{bmatrix} \begin{bmatrix} Z_{14}Z_{15}Z_{16} \\ \cdot \ Z_{25}Z_{26} \\ \cdot \ \cdot \ Z_{36} \end{bmatrix} \begin{bmatrix} Z_{17}Z_{18}Z_{19} \\ \cdot \ Z_{28}Z_{29} \\ \cdot \ \cdot \ Z_{39} \end{bmatrix}$$

$$\begin{bmatrix} \cdot \ \cdot \ \cdot \\ \cdot \ \cdot \ \cdot \\ \cdot \ \cdot \ \cdot \end{bmatrix} \begin{bmatrix} \cdot \ \cdot \ \cdot \\ \cdot \ \cdot \ \cdot \\ \cdot \ \cdot \ \cdot \end{bmatrix} \begin{bmatrix} \cdot \ \cdot \ \cdot \\ \cdot \ \cdot \ \cdot \\ \cdot \ \cdot \ \cdot \end{bmatrix}$$

$$\begin{bmatrix} \cdot \ \cdot \ \cdot \\ \cdot \ \cdot \ \cdot \\ \cdot \ \cdot \ \cdot \end{bmatrix} \begin{bmatrix} \cdot \ \cdot \ \cdot \\ \cdot \ \cdot \ \cdot \\ \cdot \ \cdot \ \cdot \end{bmatrix} \begin{bmatrix} \cdot \ \cdot \ \cdot \\ \cdot \ \cdot \ \cdot \\ \cdot \ \cdot \ \cdot \end{bmatrix}$$

Figure 4.8. Matrix structure for the example of Fig. 4.6, showing the unique elements of the matrix for $\Omega = 90°$ (see text).

$$Z_{ij} = \frac{-K_i^* K_j}{2\pi T_y} \sum_{n=-\infty}^{\infty} \int_{-\infty}^{\infty} \tilde{\mathbf{j}}_{i0}^T(\alpha,\beta_n) \ \tilde{\mathbf{G}}(\alpha,\beta_n) \ \tilde{\mathbf{j}}_{j0}(\alpha,\beta_n) \ e^{j\alpha x_{ij}} \ e^{j\beta_n y_{ij}} \, d\alpha \ ,$$

the idea is to consider the product $\tilde{\mathbf{j}}_{i0}^T \tilde{\mathbf{G}} \tilde{\mathbf{j}}_{j0}$ as a core integrand and compute all of the matrix elements at once for various values of $(x_i - x_j)$ and $(y_i - y_j)$. The evaluation of $\tilde{\mathbf{G}}$ at a single point (α, β) requires solving two N layer transmission-line problems (one TE and one TM), and, depending on the structure of the program, calculation of $\tilde{\mathbf{j}}_i$ and $\tilde{\mathbf{j}}_j$ could require several nested calls to several different function subprograms. By comparison, the calculation of $e^{j\alpha(x_i - x_j) + j\beta(y_i - y_j)}$ requires very little time. This strategy was described by Pozar [32] in a recent paper on spectral-domain analysis of a finite microstrip-patch array of thin conducting dipoles.

Unlike when the method of moments is applied in the space domain, the interactions between the most widely separated pairs of basis and testing functions are the most difficult to compute. This is due to the presence of the highly-oscillatory factor $e^{j\alpha(x_i - x_j) + j\beta(y_i - y_j)}$ in the integrand, whose rate of oscillation increases as the distances $(x_i - x_j)$ and $(y_i - y_j)$ increase. For the dominant self-terms of the matrix, this oscillatory phase factor is equal to one; therefore, calculating these terms requires the least amount of computational effort. If

the integrations are done in parallel, such that all of the integrands are sampled more heavily until each result satisfies the exit criterion, then the dominant self-terms will be the most accurate.

Another possible means of reducing the computation time to fill the matrix is based on the observation that the integral is of the form of an inverse Fourier transform. If the separations x_{ij} are all integral multiples of some value, then the FFT can be used to compute all the interactions for a given pair of basis and testing functions simultaneously. Since the FFT requires that the samples of the integrand be evenly spaced, this is equivalent to ignoring the singularity. This strategy has been used by Ko and Mittra [33]. For free-standing surfaces, the error involved in ignoring the singularity does not appear to be too great.

CHAPTER 5

NUMERICAL RESULTS

5.1 Reflection Coefficient for Periodic Surfaces

The parameter most widely used to characterize the scattering response of frequency selective surfaces is the reflection coefficient, which is a measure of the reflectivity of the surface. There are a few different ways of defining the reflection coefficient; therefore, it is necessary to be very precise in the definition to avoid confusion.

If the generalized periodic surface of Fig. 5.1 is illuminated by a plane wave, whose magnetic or electric vector potential is given by

$$\begin{Bmatrix} \mathbf{A} \\ \mathbf{F} \end{Bmatrix} = \hat{\mathbf{z}} e^{j(k_{xi}x + k_{yi}y) + \gamma_{00}z},$$

then the scattered electric field will be a discrete spectrum of plane waves of the form,

$$\mathbf{E}^s(z \geq z_t) = \sum_{p,q = -\infty}^{\infty} (\mathbf{e}_{pq} + \mathbf{e}_{00}^r \delta_{0p} \delta_{0q}) e^{j(\alpha_{pq}x + \beta_{pq}y) - \gamma_{pq}z}, \qquad (5.1)$$

where δ_{mn} is the Kroniker delta function. In this form, the scattered field can be recognized as being composed of two parts: (1) the scattered field associated with the vector constants $\mathbf{e}_{pq}$ is due to the induced current on the printed surface radiating in the presence of the dielect ic medium; and (2) the scattered field associated with $\mathbf{e}_{00}^r$ is the field reflected from the dielectric medium with the printed surface removed.

The field at the air-dielectric interface $z = z_t$ and the induced current are related by a spectral-domain Green's function, similar to the one derived in formulating the integral equation,

$$
\begin{bmatrix} \tilde{E}_x(z = z_t) \\ \\ \tilde{E}_y(z = z_t) \end{bmatrix} = \begin{bmatrix} \tilde{G}_{xx} & \tilde{G}_{xy} \\ \\ \tilde{G}_{yx} & \tilde{G}_{yy} \end{bmatrix} \begin{bmatrix} \tilde{J}_x(z = 0) \\ \\ \tilde{J}_y(z = 0) \end{bmatrix}, \tag{5.2}
$$

where **J** is now known (or an approximation to **J**) as a result of solving the discretized form of the integral equation. The derivation of the spectral Green's function is similar to the derivation in Sec. 3.1, and the details are omitted here.
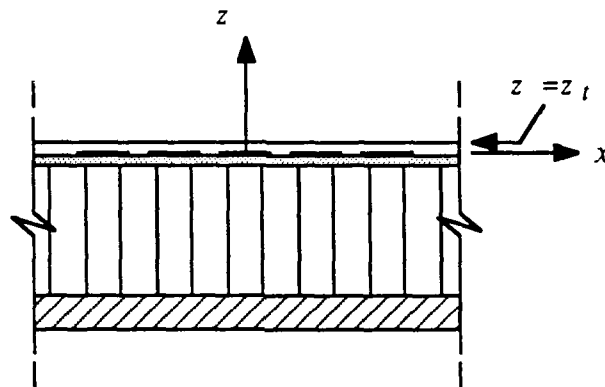
Figure 5.1. Arbitrary periodic surface surrounded by an N-layer dielectric medium.

To find the constants e_{pq}, the strategy is to take the Fourier transform of Eq. (5.1) and match the two representations (5.1) and (5.2) at $z = z_t$. Recall that the current density **J** is related to the current density on a single element $\mathbf{J}_0$ by the following relationship

$$
\tilde{\mathbf{J}}(\alpha,\beta) = \tilde{\mathbf{J}}_0(\alpha,\beta)\, \frac{2\pi}{T_{\eta_1}}\frac{2\pi}{T_{\eta_2}\sin\Omega} \sum_{p,q=-\infty}^{\infty} \delta(\alpha - \alpha_{pq})\,\delta(\beta - \beta_{pq}), \tag{5.3}
$$

where α_{pq} and β_{pq} are given by Eqs. (2.14). Performing the indicated operations leads to

$$
\sum_{p,q=-\infty}^{\infty} e_{pq} e^{-\gamma_{pq} z_t}\, 4\pi^2 \delta(\alpha - \alpha_{pq})\delta(\beta - \beta_{pq})
$$

$$
= \sum_{p,q=-\infty}^{\infty} \tilde{\mathbf{G}}(\alpha_{pq},\beta_{pq})\tilde{\mathbf{J}}_0(\alpha_{pq},\beta_{pq})\, \frac{2\pi}{T_{\eta_1}}\frac{2\pi}{T_{\eta_2}\sin\Omega}\, \delta(\alpha - \alpha_{pq})\delta(\beta - \beta_{pq}),
$$

or, equating the two series term for term,

$$\mathbf{e}_{pqt} = \frac{e^{\gamma_{pq} z_t}}{T_{\eta_1} T_{\eta_2} \sin\Omega} \, \bar{\mathbf{G}}(\alpha_{pq}, \beta_{pq}) \tilde{\mathbf{J}}_0(\alpha_{pq}, \beta_{pq}) , \tag{5.4}$$

where $\mathbf{e}_{pqt}$ is a vector of the transverse (i.e., x-y) components of $\mathbf{e}_{pq}$.

To separate the scattered field into its TE and TM components, the field is represented in terms of z-directed electric and magnetic vector potentials,

$$\mathbf{A}^s(z \geq z_t) = \hat{\mathbf{z}} \sum_{p,q=-\infty}^{\infty} R_{pq}^{TM} e^{j(\alpha_{pq} x + \beta_{pq} y) - \gamma_{pq} z} = \hat{\mathbf{z}} \sum_{p,q=-\infty}^{\infty} R_{pq}^{TM} \psi_{pq} \tag{5.5a}$$

$$\mathbf{F}^s(z \geq z_t) = \hat{\mathbf{z}} \sum_{p,q=-\infty}^{\infty} R_{pq}^{TE} e^{j(\alpha_{pq} x + \beta_{pq} y) - \gamma_{pq} z} = \hat{\mathbf{z}} \sum_{p,q=-\infty}^{\infty} R_{pq}^{TE} \psi_{pq} , \tag{5.5b}$$

where R_{pq}^{TE} and R_{pq}^{TM} are complex-valued scalar constants. An expression for the electric field is obtained by differentiating Eq. (5.5) according to,

$$\mathbf{E}^s = -\nabla \times \mathbf{F}^s - j\omega\mu \mathbf{A}^s + \frac{1}{j\omega\varepsilon_0}\nabla(\nabla\cdot\mathbf{A}^s) ,$$

or, expanding this in Cartesian coordinates,

$$E_x^s = \sum_{p,q}\left[-j\beta_{pq} R_{pq}^{TE} - \frac{j\alpha_{pq}\gamma_{pq}}{j\omega\varepsilon_0} R_{pq}^{TM} \right] \psi_{pq} \tag{5.6a}$$

$$E_y^s = \sum_{p,q}\left[+j\alpha_{pq} R_{pq}^{TE} - \frac{j\beta_{pq}\gamma_{pq}}{j\omega\varepsilon_0} R_{pq}^{TM} \right] \psi_{pq} \tag{5.6b}$$

$$E_z^s = \sum_{p,q}\left[\frac{\gamma_{pq}^2}{j\omega\varepsilon_0} - j\omega\mu \right] R_{pq}^{TM} \psi_{pq} . \tag{5.6c}$$

E_x^s and E_y^s are known quantities, given by Eqs. (5.1) and (5.4). Equations (5.6a)-(5.6b) are therefore a system of two equations in the two unknowns R_{pq}^{TE} and R_{pq}^{TM}. Solving for the unknowns, the result is

$$R_{pq}^{\text{TE}} = \frac{j[\beta_{pq}(e_{pqx} + e'_{00x}\delta_{0p}\delta_{0q}) - \alpha_{pq}(e_{pqy} + e'_{00y}\delta_{0p}\delta_{0q})]}{(\alpha_{pq}^2 + \beta_{pq}^2)} \qquad (5.7a)$$

$$R_{pq}^{\text{TM}} = \frac{j[\alpha_{pq}(e_{pqx} + e'_{00x}\delta_{0p}\delta_{0q}) + \beta_{pq}(e_{pqy} + e'_{00y}\delta_{0p}\delta_{0q})]}{(\alpha_{pq}^2 + \beta_{pq}^2)\frac{\gamma_{pq}}{j\omega\varepsilon_0}} . \qquad (5.7b)$$

The reflection coefficients are defined as R_{00}^{TE} for TE incidence and R_{00}^{TM} for TM incidence.

For a strip grating, the reflection coefficients are defined in the same way. The electric field is first expanded as a discrete spectrum of plane waves of the form,

$$\mathbf{E}^s(z \geq z_t) = \sum_{m=-\infty}^{\infty} (\mathbf{e}_m + \mathbf{e}'_0\delta_{0m})e^{j(\alpha_m x + k_{yi}y) - \gamma_m z}, \qquad (5.8)$$

where

$$\alpha_m = \frac{2\pi m}{b} + k_{xi} , \qquad (5.9a)$$

$$\gamma_m = \sqrt{\alpha_m^2 + k_{yi}^2 - k_0^2} . \qquad (5.9b)$$

At $z = z_t$, the tangential electric fields due to the induced current $\mathbf{J}$ are represented symbolically as

$$\begin{bmatrix} \tilde{E}_x(z = z_t) \\[2mm] \tilde{E}_y(z = z_t) \end{bmatrix} = \begin{bmatrix} \tilde{G}_{xx} & \tilde{G}_{xy} \\[2mm] \tilde{G}_{yx} & \tilde{G}_{yy} \end{bmatrix} \begin{bmatrix} \tilde{J}_x(z = 0) \\[2mm] \tilde{J}_y(z = 0) \end{bmatrix} , \qquad (5.10)$$

where

$$\tilde{\mathbf{J}}(\alpha,\beta) = \frac{4\pi^2}{b} \tilde{\mathbf{J}}_0(\alpha) \sum_{m=-\infty}^{\infty} \delta(\alpha - \alpha_m) \, \delta(\beta - k_{yi}) . \qquad (5.11)$$

Matching the two representations at $z = z_t$,

$$4\pi^2 \sum_{m=-\infty}^{\infty} \mathbf{e}_{mt}e^{-\gamma_m z_t} \, \delta(\alpha - \alpha_m)\delta(\beta - k_{yi})$$

$$= \frac{4\pi^2}{b} \sum_{m=-\infty}^{\infty} \tilde{\mathbf{G}}(\alpha_m, k_{yi})\tilde{\mathbf{J}}_0(\alpha_m)\delta(\alpha - \alpha_m)\delta(\beta - k_{yi}), \qquad (5.12)$$

from which it follows that

$$\mathbf{e}_{mt} = \frac{e^{\gamma_m z_t}}{b} \, \tilde{\mathbf{G}}(\alpha_m, k_{yi}) \tilde{\mathbf{J}}_0(\alpha_m) \; . \qquad (5.13)$$

If the scattered field is assumed to be composed of TE and TM-polarized plane-wave fields derived from $\mathbf{A}^s$ and $\mathbf{F}^s$, where

$$\mathbf{A}^s(z \geq z_t) = \hat{\mathbf{z}} \sum_{m=-\infty}^{\infty} R_m^{TM} e^{j(\alpha_m x + k_{yi} y) - \gamma_m z} = \hat{\mathbf{z}} \sum_{m=-\infty}^{\infty} R_m^{TM} \psi_m^r \qquad (5.14a)$$

$$\mathbf{F}^s(z \geq z_t) = \hat{\mathbf{z}} \sum_{m=-\infty}^{\infty} R_m^{TE} e^{j(\alpha_m x + k_{yi} y) - \gamma_m z} = \hat{\mathbf{z}} \sum_{m=-\infty}^{\infty} R_m^{TE} \psi_m^r \; , \qquad (5.14b)$$

then

$$R_m^{TE} = \frac{j[k_{yi}(e_{mx} + e_{0x}^r \delta_{0m}) - \alpha_m(e_{my} + e_{0y}^r \delta_{0m})]}{(\alpha_m^2 + k_{yi}^2)} \qquad (5.15a)$$

$$R_m^{TM} = \frac{j[\alpha_m(e_{mx} + e_{0x}^r \delta_{0m}) + k_{yi}(e_{my} + e_{0y}^r \delta_{0m})]}{(\alpha_m^2 + k_{yi}^2)\frac{\gamma_m}{j\omega\varepsilon_0}} \; . \qquad (5.15b)$$

As before, R_0^{TE} and R_0^{TM} are defined to be the reflection coefficients for TE and TM incidence, respectively.

If the incident field is derived from unit-amplitude vector potentials, the reflection coefficients defined here have the following properties:

1. The magnitudes of R_{pq}^{TE} and R_{pq}^{TM} may be greater than one, particularly for fields scattered from the TM polarization into the TE polarization.

2. However, conservation of power requires that

$$|R_{00}^{TE}| \leq 1, \text{ for TE incidence, and}$$
$$|R_{00}^{TM}| \leq 1, \text{ for TM incidence.}$$

3. The reflection coefficients for a free-standing perfectly-conducting plane at $z = 0$ are

$$R_{00}^{TE} = -1, \text{ for TE incidence, and}$$
$$R_{00}^{TM} = +1, \text{ for TM incidence.}$$

5.2 Reflection Coefficient for Finite Surfaces

The reflection coefficients defined for periodic surfaces were carefully chosen to be compatible with the definitions in this section. In the limit as the number of elements in a finite frequency selective surface approaches infinity, the reflection coefficient defined for the finite surface must be equivalent to the reflection coefficient defined for the periodic surface in order to make a direct comparison between the two.

Rather than attempt to justify each individual assumption, it is simpler to postulate a reasonable definition for the reflection coefficient and verify numerically that it has the desired properties. Since the reflection coefficient for a perfectly-conducting plane is equal to ± 1, then, except for a minus sign for the TE polarization, the reflection coefficient derived in the previous section can be interpreted as the complex amplitude of the plane-wave field scattered by the surface in the specular direction divided by the complex amplitude of the plane-wave field reflected from a perfectly-conducting plane. This is essentially the definition that will be used for the finite array, with the language modified to account for the finite nature of the scatterer.

The scattered field can be viewed as a superposition of two parts: $\mathbf{E}_d^s$, the field scattered from the surface of the dielectric medium with the printed surface removed, and $\mathbf{E}_c^s$, the field due to the conduction current on the printed surface, radiating in the presence of the dielectric medium. With the printed surface removed, the plane-wave field reflected from the infinite dielectric stratification $\mathbf{E}_d^s$ is of the form

$$\mathbf{E}_d^s(z \geq z_t) = \mathbf{e}_{00}^r e^{j(k_{xi}x + k_{yi}y) - \gamma_{00}z}, \tag{5.16}$$

where the vector constant $\mathbf{e}_{00}^r$ is computed by the transmission-line method using the techniques discussed in Chapter 3. For a finite-width frequency selective surface, this part of the scattered field is approximately proportional to the field produced by

$$\mathbf{E}_{dt}^s(x,y,z_t) = [\ \mathbf{e}_{00t}^r e^{-\gamma_{00}z_t}\ ]e^{j(k_{xi}x + k_{yi}y)} P_x\left(\frac{-N_e T_x}{2}, \frac{N_e T_x}{2}\right) P_y\left(\frac{-T_y}{2}, \frac{T_y}{2}\right), \tag{5.17}$$

which is a physical optics approximation to the tangential fields at the surface of the dielectric. N_e is the number of elements in a unit row across the finite dimension of the array; T_x and T_y are the x and y periodicities of the printed surface ($T_x = T_{\eta 1}$ and $T_y = T_{\eta 2}\sin\Omega.$). The truncation factors P_x and $P_y(a,b)$ are zero except on $[a,b]$ where they are equal to one. The far field radiated by this surface field is computed using standard techniques.

The remaining component of the scattered fields is due to the conduction current on the printed surface. To keep the proper proportionality with the first term, $\mathbf{E}_c^s$ is the field due to a unit row of elements radiating in the presence of the dielectric support and is given by a spectral-domain Green's function of the form,

$$
\begin{bmatrix} \tilde{E}_x(z = z_t) \\[2ex] \tilde{E}_y(z = z_t) \end{bmatrix} = \begin{bmatrix} \tilde{G}_{xx} & \tilde{G}_{xy} \\[2ex] \tilde{G}_{yx} & \tilde{G}_{yy} \end{bmatrix} \begin{bmatrix} \tilde{J}_x(z = 0) \\[2ex] \tilde{J}_y(z = 0) \end{bmatrix} .
\tag{5.18}
$$

The far fields produced by this equivalent magnetic current sheet are obtained by evaluating the Fourier transforms of the electric field at arguments which are determined by the observation angles (θ,φ). If the incident plane-wave field is incident from the direction (θ_i,φ_i), the reflection coefficient is defined as the total far-zone scattered field $\mathbf{E}_d^s + \mathbf{E}_c^s$ in the specular direction, $(-\theta_i,\varphi_i)$, normalized by $\mathbf{E}_p^s$, the far-zone physical optics field scattered by a perfectly-conducting plate of area $N_e T_x \times T_y$.

$$
R_{\phi\phi} = \frac{E_{d\phi}^s(-\theta_i, \phi_i) + E_{c\phi}^s(-\theta_i, \phi_i)}{E_{p\phi}^s(-\theta_i, \phi_i)}, \text{ TE incidence}
\tag{5.19a}
$$

$$
R_{\theta\theta} = \frac{E_{d\theta}^s(-\theta_i, \phi_i) + E_{c\theta}^s(-\theta_i, \phi_i)}{E_{p\theta}^s(-\theta_i, \phi_i)}, \text{ TM incidence.}
\tag{5.19b}
$$

It is easily verified that, for TE incidence, the physical optics approximation for the current on a perfectly-conducting plate produces a far-zone electric field that is entirely in the $\hat{\phi}$ direction, and for TM incidence, the far field is entirely in the $\hat{\theta}$ direction.

This definition is easily extended to surfaces which are finite in both dimensions, and the same definition can also be used for finite strip gratings, with the slight inconvenience of having to define an arbitrary period "T_y." In addition, the following properties have been verified numerically: if the induced current satisfies the periodic condition, i.e., if, instead of the current on a finite frequency selective surface, the current on a number of elements of a periodic surface is substituted for $J_0(x,y)$, then, (1) the reflection coefficient is independent of the number of elements N_e, and (2), except for a minus sign for the TE polarization, the value of the reflection coefficient is identical (to at least four significant figures in all our sample calculations) to the value obtained by using the plane-wave definition.

5.3 Finite Strip Grating

In Chapter 2, it was shown that for a finite planar strip grating illuminated by an arbitrary plane wave, the current density $\mathbf{J}$ on the infinite plane could be represented in terms of the current density $\mathbf{J}_0(x)$ along the cut $y = 0$. In the transform domain,

$$\tilde{\mathbf{J}}(\alpha,\beta) = 2\pi \, \tilde{\mathbf{J}}_0(\alpha)\delta(\beta - k_y) \ .$$

In Chapter 3, an integral equation for the fundamental unknown $\mathbf{J}_0(x)$ was derived, and the spectral-domain method of moments was applied to generate a matrix equation; i.e., if

$$\tilde{\mathbf{J}}_0(\alpha) = \sum_{j=1}^{I} c_j \, \tilde{j}_j(\alpha) \ ,$$

then

$$\frac{-1}{2\pi}\sum_{j=1}^{I} c_j \int_{-\infty}^{\infty} \tilde{j}_i^\dagger(\alpha) \, \tilde{G}(\alpha,k_y) \, \tilde{j}_j(\alpha)e^{jk_y y}d\alpha = \int_{x=-\infty}^{\infty} j_i^\dagger(x) \, E^{inc}(x,y) \, dx \ , \ i = 1, 2, ..., I \ .$$

In Chapter 4, the essential theoretical and numerical considerations were discussed that pertain to implementing the spectral-Galerkin equation efficiently and accurately on the computer. The only remaining steps involve choosing a linearly-independent basis $\{j_j\}$ for

expanding the unknown and solving the resultant system of equations for the coefficients $\{c_j\}$.

The transverse current J_{x0} is discretized using the trigonometric series

$$j_{xk}(x) = \sin\left[\frac{k\pi}{2h}\left((x - x_k) + h\right)\right]P_x(x_k - h, x_k + h), \quad k = 1, 2, \ldots, N_{sin} \quad (5.20)$$

and the parallel component of the current J_{y0} is represented by functions of the form,

$$j_{yk}(x) = \frac{T_{k-1}\left(\frac{(x-x_k)}{h}\right)}{\sqrt{1 - \left(\frac{(x-x_k)}{h}\right)^2}}P_x(x_k - h, x_k + h), \quad k = 1, 2, \ldots, N_{cheb}, \quad (5.21)$$

where $T_n(x)$ is the Chebychev polynomial of order n,

$$T_n(x) = \cos(n \cos^{-1}(x)),$$

h is the half-width of the strips ($h = a/2$), x_k is the position of the basis function relative to the origin, and the truncation factor P_x, which limits the extent of the functions to the surfaces of the conductors, is defined as

$$P_x(x_1, x_2) = \left\{\begin{array}{l} 1, x_1 \leq x \leq x_2 \\ 0, \text{ otherwise} \end{array}\right\}.$$

Note that each term in the expansion of J_{y0} has a built-in edge singularity to model the physical behavior of the current. The first few terms of this series are shown in Fig. 5.2. The Fourier transforms of the basis functions are [34]

$$\tilde{j}_{xk}(\alpha) = -jh\, e^{\left(\frac{k\pi}{2}\right)}\left\{ \text{sinc}\left(\frac{k\pi}{2} - \alpha h\right) - (-1)^k\text{sinc}\left(\frac{k\pi}{2} + \alpha h\right)\right\}e^{-j\alpha x_k} \quad (5.22)$$

$$\tilde{j}_{yk}(\alpha) = (-j)^{k-1}\pi h\, J_{(k-1)}(-\alpha h)\, e^{-j\alpha x_k}, \quad (5.23)$$

where $j = \sqrt{-1}$, $\text{sinc}(x) = \sin(x)/x$, and $J_n(x)$ is the nth-order Bessel function of the first kind.
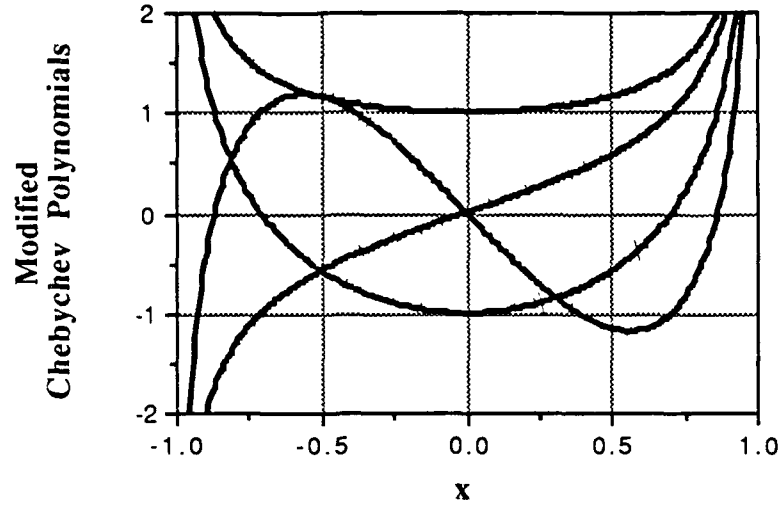
Figure 5.2. Chebychev polynomials modified to incorporate the edge singularity.

To verify that these basis and testing functions have sufficient smoothness to guarantee convergence of the inner products, the asymptotic behavior of the product $\tilde{\mathbf{j}}_i{}^\dagger(\alpha)\tilde{\mathbf{G}}(\alpha,k_{yi})\tilde{\mathbf{j}}_j(\alpha)$ is examined for each combination of basis and testing function, i.e.,

$$R_{xx}(\alpha) = \tilde{j}_{xk}(\alpha)\tilde{G}_{xx}(\alpha,k_y)\tilde{j}_{xk}(\alpha)$$

$$R_{xy}(\alpha) = \tilde{j}_{xk}(\alpha)\tilde{G}_{xy}(\alpha,k_y)\tilde{j}_{yk}(\alpha)$$

$$R_{yy}(\alpha) = \tilde{j}_{yk}(\alpha)\tilde{G}_{yy}(\alpha,k_y)\tilde{j}_{yk}(\alpha) \ .$$

The two $\sin(\alpha)/\alpha$ terms combine in such a way that the net convergence of $\tilde{j}_{xk}(\alpha)$ is not $1/\alpha$, but $1/\alpha^2$. This might have been expected, since the trigonometric basis functions have the same degree of differentiability as the triangular basis function, whose Fourier transform is $\dfrac{\sin^2(\alpha)}{\alpha^2}$, which is well known. The asymptotic expression for $J_n(x)$ is given by

$$J_n(x) \rightarrow \sqrt{\frac{2}{\pi x}}\ \cos\left(x - \frac{\pi}{4} - \frac{n\pi}{2}\right) .$$

If each term in the product $\tilde{\mathbf{j}}_i^\dagger(\alpha)\tilde{\mathbf{G}}(\alpha,k_{yi})\tilde{\mathbf{j}}_j(\alpha)$ is replaced by its asymptotic form, then, except for a constant, the asymptotic expressions for the integrands R_{xx}, R_{xy}, and R_{yy} are given by

$$R_{xx}(\alpha) \rightarrow \frac{1}{\alpha^2}\frac{\alpha^2}{\sqrt{\alpha^2 + k_y^2}}\frac{1}{\alpha^2} \rightarrow \frac{1}{\alpha^3} \tag{5.24a}$$

$$R_{xy}(\alpha) \rightarrow \frac{1}{\alpha^2}\frac{\alpha k_y}{\sqrt{\alpha^2 + k_y^2}}\frac{1}{\sqrt{\alpha}} \rightarrow \frac{1}{\alpha^2\sqrt{\alpha}} \tag{5.24b}$$

$$R_{yy}(\alpha)) \rightarrow \frac{1}{\sqrt{\alpha}}\frac{k_y^2}{\sqrt{\alpha^2 + k_y^2}}\frac{1}{\sqrt{\alpha}} \rightarrow \frac{1}{\alpha^2}. \tag{5.24c}$$

For this choice of basis and testing functions, the integrands and summands converge at least as fast as $1/\alpha^2$.

The inner products formed by applying the spectral-domain method of moments contain either infinite summations or integrals with infinite limits of integration. If no extrapolation techniques are used to predict the contribution of the tail regions [35], the summations or integrations are truncated to a finite area of the $\alpha-\beta$ plane. When truncating the spectrum, however, the limits of summation or integration must encircle the highest spectral component of the current; otherwise, the moment matrix will be ill-conditioned [36]. For the trigonometric series, the peak of the highest spectral component of the current occurs at $\alpha = \frac{\pi N_{sin}}{2h}$. Therefore, the first opportunity to truncate the spectrum is at the first zero beyond the peak or at $(N_{sin} + 2)\frac{\pi}{2h}$. By a similar argument, the spectral bandwidth of the Chebychev series is approximately $(N_{cheb} + 1)\frac{\pi}{2h}$. In all of the results in this section, the spectrum has been truncated at twice the maximum of these two numbers.

Electromagnetic scattering from a free-standing periodic strip grating has been solved exactly by Weinstein [10] using the generalized Wiener-Hopf technique. Figure 5.3 gives an idea of the accuracy of the numerical results by comparing the magnitude of the reflection coefficient computed by Weinstein's method with the results of applying this

theory to the same problem. The incident electric field, which is incident normally on the surface, is polarized either parallel or perpendicular to the axes of strips. The numerical results have been computed assuming four trigonometric basis functions and four modified Chebychev polynomials to represent the unknown. Since the incident angles $(\theta_i, \varphi_i) =$ (0,0) are not allowed when computing the incident field by the vector potential method, $(\theta_i, \varphi_i) = (0.1°, 0.1°)$ have been used for the numerical calculations. The worst-case deviation of the results is 4.3 percent.

To illustrate the effect of truncation, Figs. 5.4 and 5.5 show the frequency response of the periodic strip grating of Fig. 5.3, truncated to 3, 7, and 15 strips. This case was considered by Cwik and Mittra [9] using the equivalent of 64 subsectional basis functions per strip, for the two polarizations of the incident field. In the 15-strip example, this requires filling a 960 × 960 matrix. The results of Figs. 5.3 and 5.4, which are in excellent agreement with the results of Cwik and Mittra, were computed using 8 basis functions per strip, or by filling a 120 × 120 matrix. This underlines the importance of choosing a basis set that is capable of modeling the current in a minimum number of terms.

As pointed out by the previous investigators [9], the effect of finite dimensions is greater when the incident electric field is polarized parallel to the truncation boundary, i.e., when the dominant component of the induced current is flowing parallel to the edge of the finite array. In Fig. 5.4, where the incident electric field is polarized parallel to the truncation boundary, the fields scattered by a finite strip grating can be significantly different from the fields produced by an equal number of strips in an infinite array; this difference becomes less as the number of strips is increased. Conversely, when the incident electric field is polarized perpendicularly to the edge of the array over this frequency range, the difference between the periodic solution for the reflection coefficient and the finite solution is minimal, even for as few as 3 strips. Because of the properties of *the reflection coefficients mentioned in Sections 5.1 and 5.2, the close agreement in Fig.*

TE (Parallel) Polarization

(a)

TM (Perpendicular) Polarization

(b)
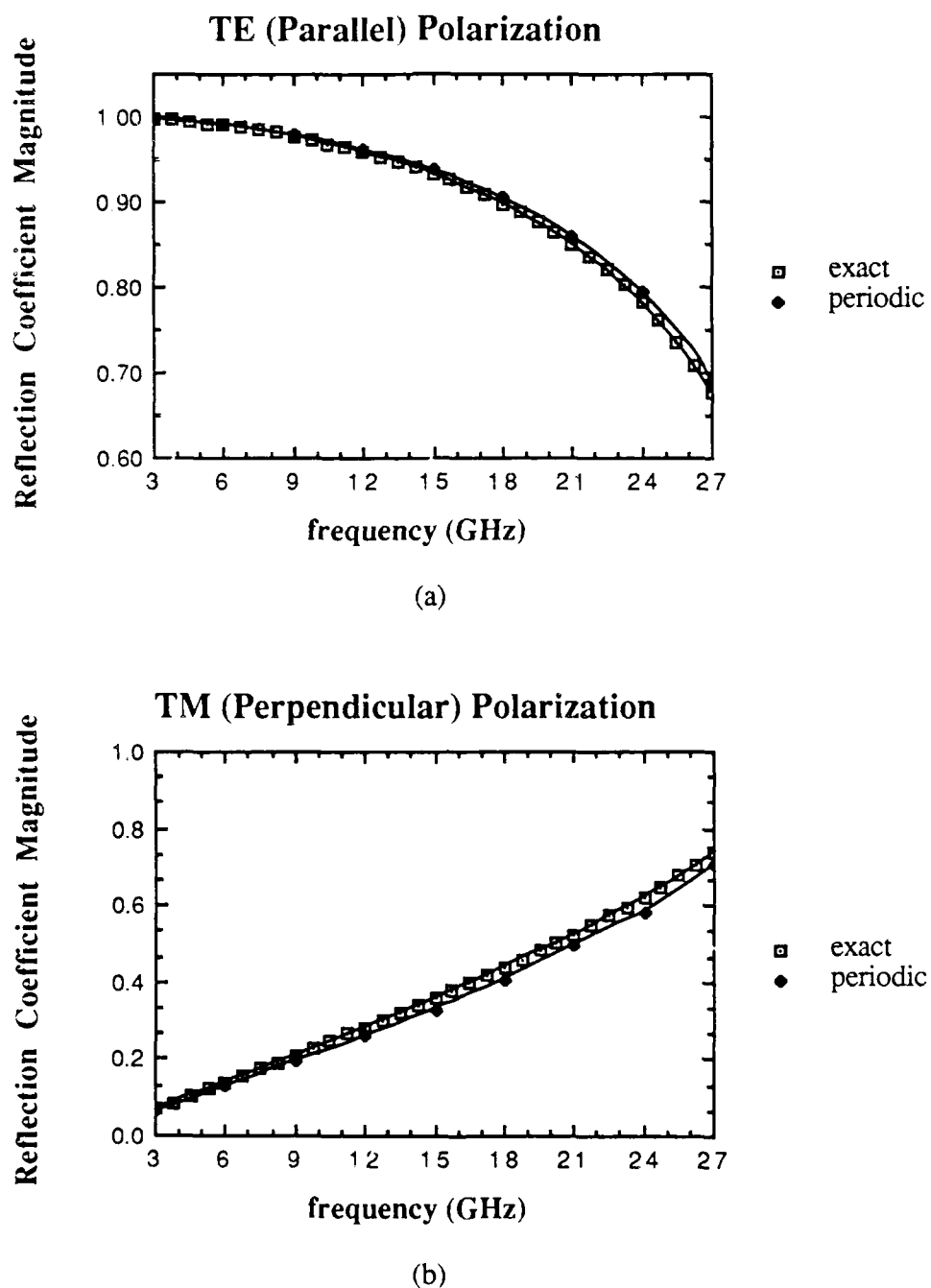
Figure 5.3. Comparison of numerical and exact reflection coefficients for a periodic strip grating: strip width $a = 0.5$ cm, periodicity $b = 1$ cm. (a) E^{inc} polarized parallel to the axis of the strips, (b) E^{inc} polarized perpendicular to the axis of the strips.
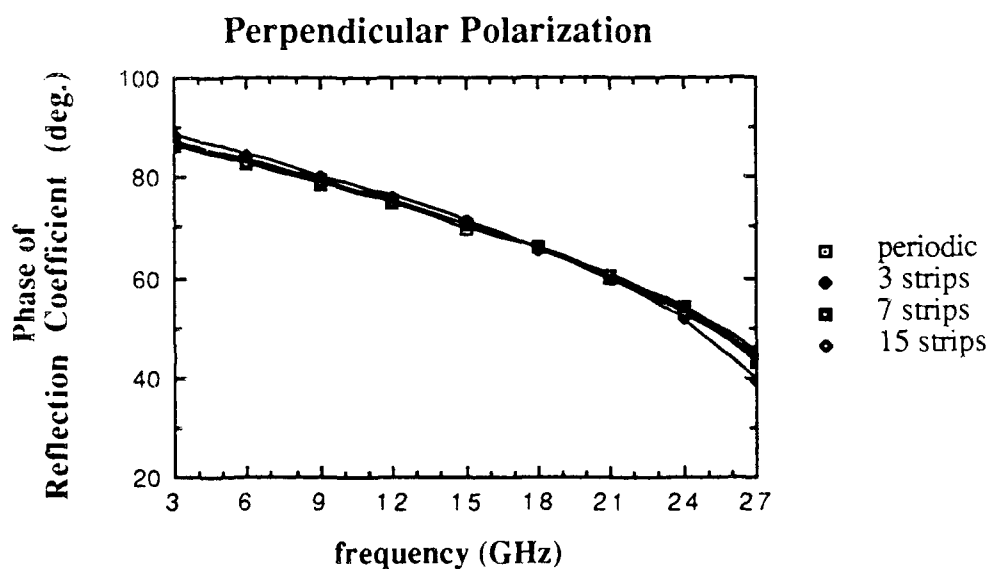
Parallel Polarization

(a)

Parallel Polarization

(b)
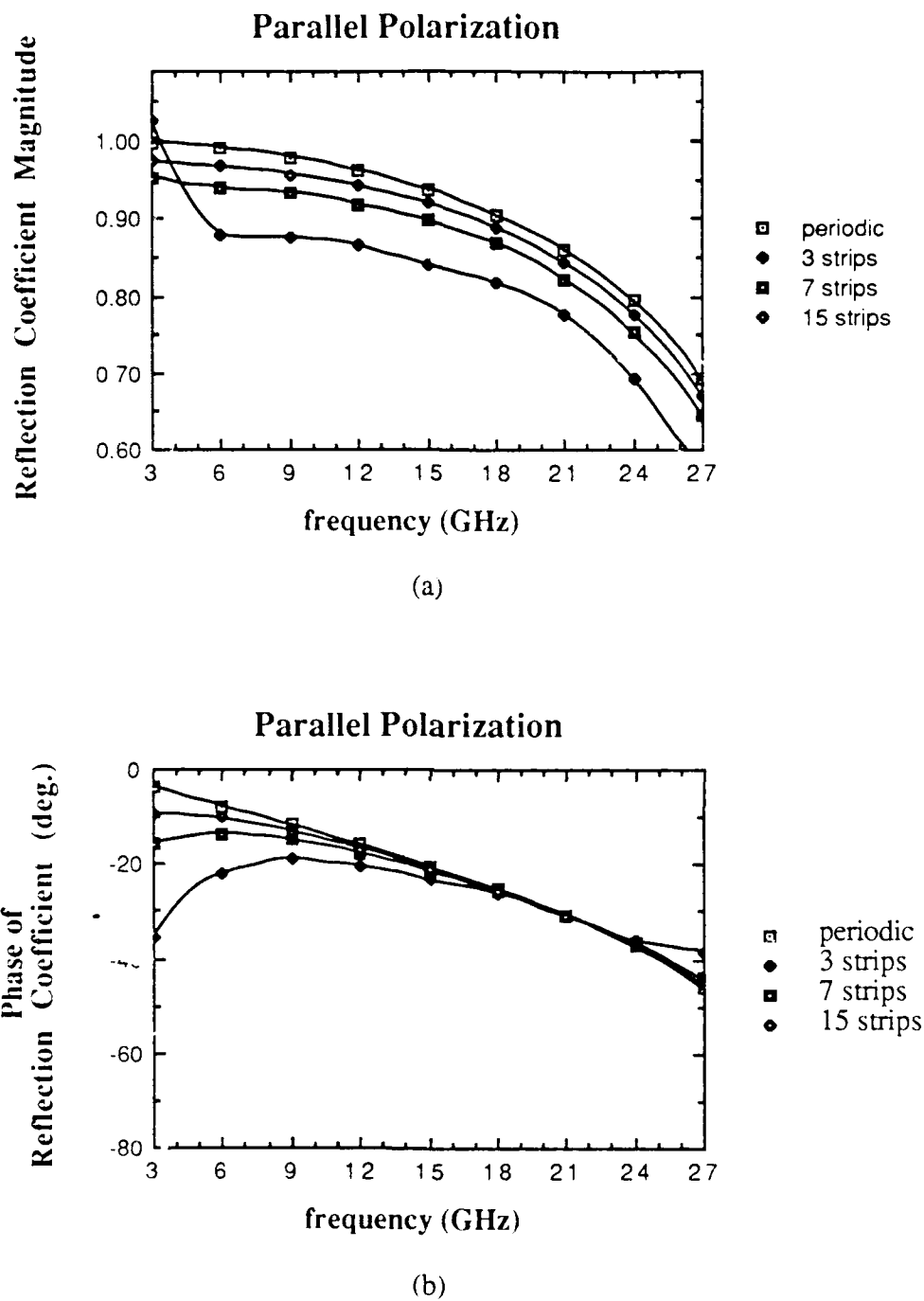
Figure 5.4. (a) Magnitude and (b) phase of the computed reflection coefficient for a plane wave incident on several free-standing strip gratings of 3, 7, and 15 strips, compared to the periodic result: TE polarization, strip width = 0.5 cm, periodicity = 1 cm, $(\theta_i, \varphi_i) = (0.1°, 0.1°)$.

Perpendicular Polarization

(a)

Perpendicular Polarization
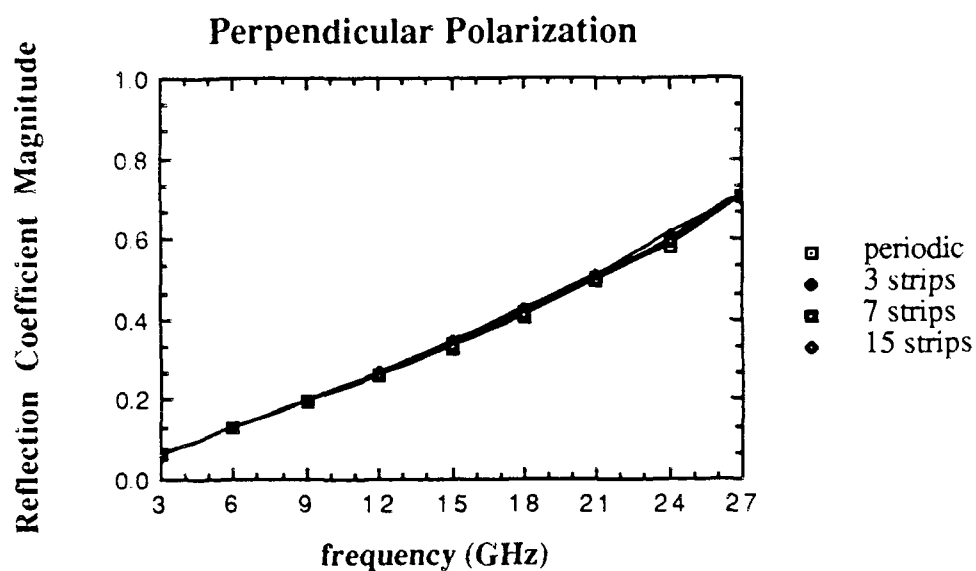
(b)

Figure 5.5. (a) Magnitude and (b) phase of the computed reflection
coefficient for a plane wave incident on several free-standing
strip gratings of 3, 7, and 15 strips, compared to the periodic
result: TM polarization, strip width = 0.5 cm, periodicity =
1 cm, $(\theta_i, \varphi_i) = (0.1°, 0.1°)$.

5.5 indicates that, for perpendicular polarization, the field scattered in the specular direction by a finite number of strips can be accurately approximated by the field produced by an equal number of strips whose currents have been obtained from a periodic model.

One of the reasons why the periodic approximation is valid for a finite array is that the edge effect is localized. This is illustrated in Figs. 5.6(a) and 5.6(b). A periodic surface is characterized by the fact that the induced current on any one cell differs from the current on any other cell only by the uniform progressive phase shift of the incident field. Therefore, the magnitudes of the current densities on a number of cells will be identical in both shape and amplitude. If the finite-array problem is solved using the same approximations that were used in the periodic problem, then any deviation in the behavior of the current from this uniform amplitude and shape is entirely due to the edge effect. A plot of the magnitude of the current density across a number of cells of a 15-element strip grating is shown in Fig. 5.6(a) for parallel polarization and Fig. 5.6(b) for perpendicular polarization. Only half of the cell currents are plotted since the incident field and geometry are symmetrical. Also shown are the corresponding currents on a periodic strip grating. From these results, it is evident that there is a locally-confined edge region that penetrates only about three strips into the interior of the array. As the array becomes larger, the edge region occupies a smaller proportion of the total area. The interior region, however, where the currents closely match those of the periodic array, occupies a larger proportion of the total area.

5.4 Crossed Dipole Element

The crossed dipole element was originally intended to be a simple extension of the linear dipole. It had been known for some time that for an incident plane-wave field of the proper polarization and frequency, a periodic array of thin conducting dipoles was capable of reflecting the field as though it were a sol'd sheet of perfectly conducting metal [37].

Parallel Polarization

(a)

Perpendicular Polarization
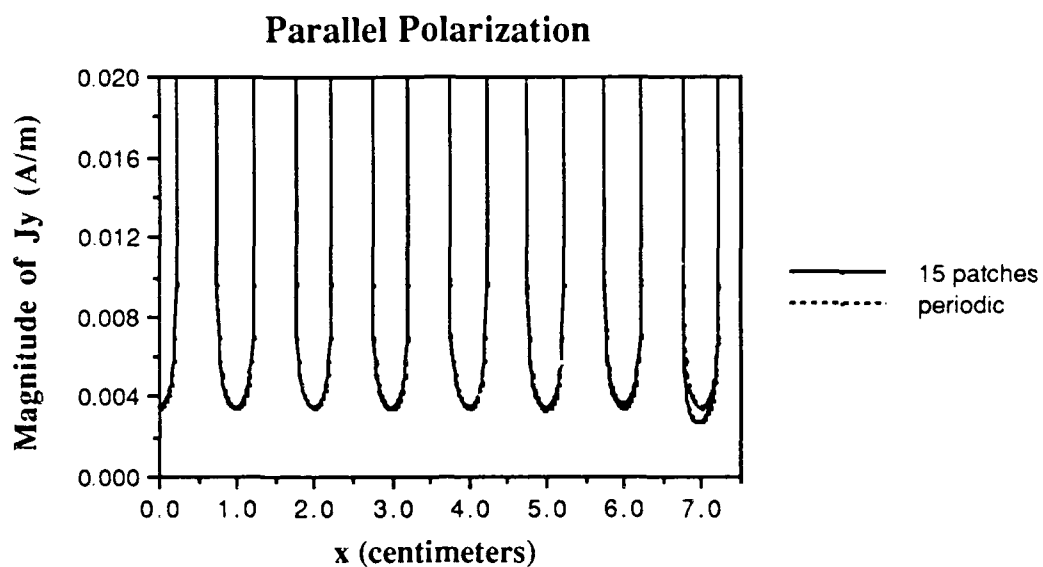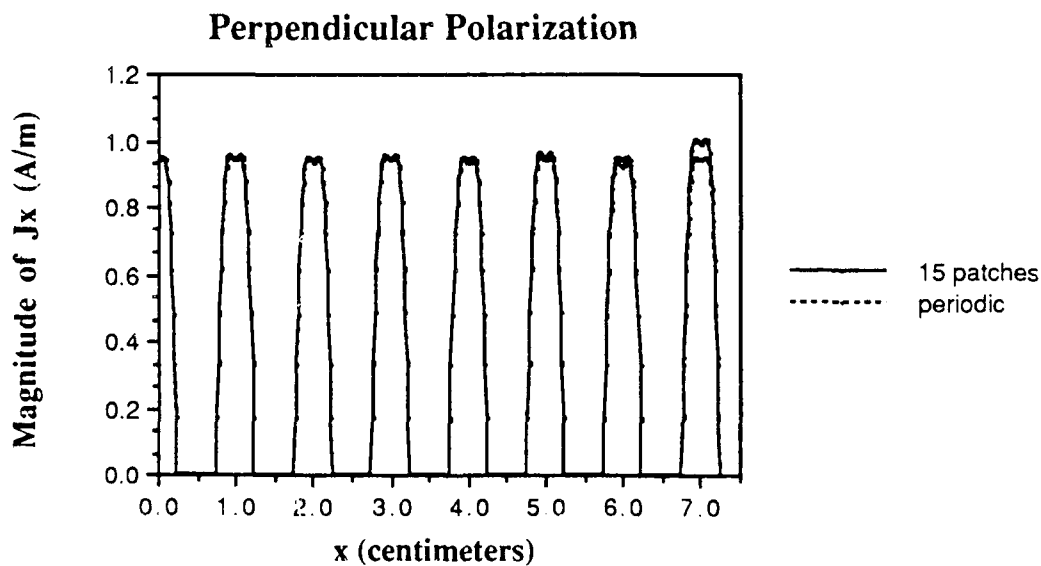
(b)

Figure 5.6. Dominant currents induced on a 15-element finite strip grating along the cut y = 0: (a) parallel polarization, (b) perpendicular polarization. Strip width = 0.5 cm, periodicity = 1 cm, $(\theta_i, \varphi_i) = (0.1°, 0.1°)$.

The crossed dipole was an attempt to make this effect independent of the polarization of the incident field.

The crossed dipole has been a popular choice in applications requiring circular polarization. For certain skew angles, the crossed dipole array has the property that at normal incidence, the surface looks the same to each of the two linear components of a circularly-polarized incident field. On reflection or transmission, the relative amplitudes and phases of the two components are preserved, and the scattered fields are circularly-polarized as well. Examples of other elements having the same property are Jerusalem crosses, square patches, and rings. But because of the ease of fabricating crossed dipole arrays and the apparent simplicity of modeling them analytically, most of the experimental and theoretical work has been conducted with crossed dipole arrays [8, 14, 17, 38-40].

However, the apparent simplicity of modeling periodic arrays of crossed dipoles was deceptive. This was due to the fact that the current induced on the two perpendicular arms of the cross was not simply the superposition of the currents on two isolated linear dipoles. In addition to these, another term was present, sometimes referred to as the "crooked mode," due to the mutual coupling between the two arms. In 1977, King published his solution for the zero-order currents on the cross [41], which included the new term, and soon afterward, Pelton and Munk showed that it was the presence of this term that caused the anomalous antiresonance that had been observed in the frequency response of crossed dipole arrays for oblique incidence [39].

The problem was later revisited by Tsao and Mittra [8], who incorporated the so-called "crooked mode" by using a special junction basis function. The basis functions used here are the same as those used by Tsao and Mittra in their treatment. Referring to Fig. 5.7, if L is the length and W is the width of each of the two dipole members, then the basis functions can be expressed in the form

$$j_{xk}(x,y) = \sin\left[\frac{k\pi}{L}\left(x + \frac{L}{2}\right)\right] P_x\left(\frac{-L}{2}, \frac{L}{2}\right) P_y\left(\frac{-W}{2}, \frac{W}{2}\right), \quad k = 1, 2, \ldots, N_{sin} \quad (5.25a)$$

$$j_{yk}(x,y) = \sin\left[\frac{k\pi}{L}\left(y + \frac{L}{2}\right)\right] P_x\left(\frac{-W}{2},\frac{W}{2}\right) P_y\left(\frac{-L}{2},\frac{L}{2}\right), \quad k = 1, 2, \ldots, N_{sin} \quad (5.25b)$$

$$\mathbf{j}_j(x,y) = \hat{\mathbf{x}} \, \text{sgn}(x) \cos\left(\frac{\pi x}{L}\right) P_x\left(\frac{-L}{2},\frac{L}{2}\right) P_y\left(\frac{-W}{2},\frac{W}{2}\right)$$

$$- \hat{\mathbf{y}} \, \text{sgn}(y) \cos\left(\frac{\pi y}{L}\right) P_x\left(\frac{-W}{2},\frac{W}{2}\right) P_y\left(\frac{-L}{2},\frac{L}{2}\right), \quad (5.25c)$$

where only the basis functions at the origin have been shown. The truncation factors $P_x(a,b)$ and $P_y(a,b)$ are defined to be zero except on the interval $[a,b]$, where they are equal to one.
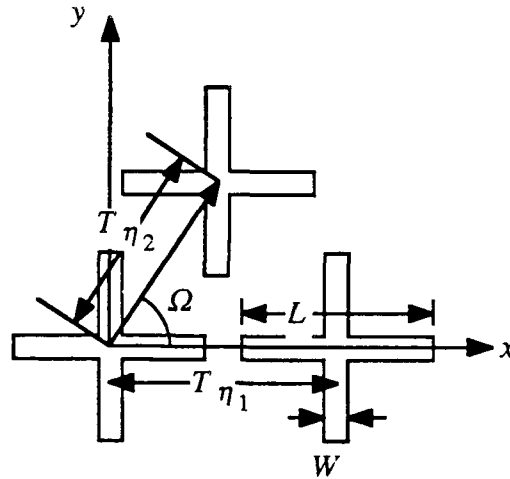
Figure 5.7. Geometry of the crossed-dipole array.

The Fourier transforms of the basis functions are

$$\bar{j}_{xk}(\alpha,\beta) = \frac{-jLW}{2} e^{j\left(\frac{k\pi}{2}\right)} \frac{\sin\left(\beta\frac{W}{2}\right)}{\left(\beta\frac{W}{2}\right)} \left\{ \frac{\sin\left(\frac{k\pi}{2} - \frac{\alpha L}{2}\right)}{\left(\frac{k\pi}{2} - \frac{\alpha L}{2}\right)} - (-1)^k \frac{\sin\left(\frac{k\pi}{2} + \frac{\alpha L}{2}\right)}{\left(\frac{k\pi}{2} + \frac{\alpha L}{2}\right)} \right\} \quad (5.26a)$$

$$\bar{j}_{yk}(\alpha,\beta) = \frac{-jLW}{2} e^{j\left(\frac{k\pi}{2}\right)} \frac{\sin\left(\alpha\frac{W}{2}\right)}{\left(\alpha\frac{W}{2}\right)} \left\{ \frac{\sin\left(\frac{k\pi}{2} - \frac{\beta L}{2}\right)}{\left(\frac{k\pi}{2} - \frac{\beta L}{2}\right)} - (-1)^k \frac{\sin\left(\frac{k\pi}{2} + \frac{\beta L}{2}\right)}{\left(\frac{k\pi}{2} + \frac{\beta L}{2}\right)} \right\} \quad (5.26b)$$

$$\tilde{\mathbf{j}}_j(\alpha,\beta) = \frac{jLW}{2} \left[\begin{array}{l} \hat{\mathbf{x}} \dfrac{\sin\left(\beta\dfrac{W}{2}\right)}{\left(\beta\dfrac{W}{2}\right)} \left\{ \dfrac{1-\cos\left(\dfrac{\pi}{2}-\dfrac{\alpha L}{2}\right)}{\left(\dfrac{\pi}{2}-\dfrac{\alpha L}{2}\right)} - \dfrac{1-\cos\left(\dfrac{\pi}{2}+\dfrac{\alpha L}{2}\right)}{\left(\dfrac{\pi}{2}+\dfrac{\alpha L}{2}\right)} \right\} \\ -\hat{\mathbf{y}} \dfrac{\sin\left(\alpha\dfrac{W}{2}\right)}{\left(\alpha\dfrac{W}{2}\right)} \left\{ \dfrac{1-\cos\left(\dfrac{\pi}{2}-\dfrac{\beta L}{2}\right)}{\left(\dfrac{\pi}{2}-\dfrac{\beta L}{2}\right)} - \dfrac{1-\cos\left(\dfrac{\pi}{2}+\dfrac{\beta L}{2}\right)}{\left(\dfrac{\pi}{2}+\dfrac{\beta L}{2}\right)} \right\} \end{array} \right]. \quad (5.26c)$$

The junction function is only included to provide a minimum-term representation for the current on the cross. Basis functions of either subdomain or entire-domain type are capable of modeling the current at a junction, provided the number of terms is sufficiently high. By using the junction function, the object is to reduce the number of unknowns from approximately 10 per wavelength to approximately 2.5 per wavelength.

These basis functions give the weakest form of convergence. Asymptotically, the Fourier transform of the junction basis function decays as $\dfrac{1}{\alpha}\dfrac{1}{\beta}$. Combining this with the asymptotic expression for the spectral Green's function, the product $\tilde{\mathbf{j}}_i{}^\dagger \tilde{\mathbf{G}} \tilde{\mathbf{j}}_j$ decays only as fast as $\dfrac{1}{\alpha}\dfrac{1}{\beta^3}$ for the junction-junction interaction. If β is held constant while an integration is performed over α, which is the procedure suggested by Eq. (3.47), the inner product will not converge. However, in polar coordinates [42], where $\alpha = k_\rho\cos\varphi$ and $\beta = k_\rho\sin\varphi$, the worst-case convergence rate is $1/k_\rho^2\sin^2\varphi$, i.e., except for along the radius $\varphi = 0$, the k_ρ integration converges.

Sample results using this basis set are shown in Fig. 5.8, for a geometry similar to one in the literature [15]. The geometry is a periodic array of cross-shaped conducting patches ($T_{\eta 1} = T_{\eta 2} = 1$ cm, $L = 0.6875$ cm, $W = 0.0625$ cm, $\Omega = 90$ deg) printed on a 3 mm dielectric substrate of relative permittivity $\varepsilon_r = 4 - j.02$. The frequency response has been computed twice, once using rooftop basis functions (12 per arm), and once using the entire-domain functions of Tsao and Mittra (2 per arm plus the junction function). The agreement between the results is quite good. It is interesting to note that the addition of a

small amount of loss in the dielectric region prevents the reflection characteristic from reaching a maximum of 1.0 at resonance.

If the same element and lattice are assumed for frequency selective surfaces of 3, 7, and 15 patches wide, most of the difference in the plot of the reflection coefficient occurs near the resonant frequency. Figures 5.9 and 5.10 show the variation in the reflection coefficient for different array sizes. As before, the greatest difference between the finite and periodic results occurs for the smallest number of elements, the difference becoming less as more elements are considered. When the dominant component of the current is flowing parallel to the edge of the array (TE polarization), the edge has more influence on the reflected fields; when the dominant current is flowing perpendicularly to the edge of the array, the edge effect is less significant.

As a second example, the free-standing surface of Pelton and Munk [39] is considered, which is periodic in skewed coordinates: $T_{\eta 1} = 2.44$ cm, $T_{\eta 2} = 1.725$ cm, $L = 1.51$ cm, $W = 0.044$ cm, $\Omega = 45$ deg. Figure 5.11 compares computed values of the reflection coefficient from a periodic surface and their measured results for oblique incidence ($\theta_i = 30°$), showing the characteristic antiresonance of the crossed-dipole array. For this example, two trigonometric basis functions per arm plus the junction function were used to approximate the current on the cross. The Floquet harmonics were summed out to a point which was twice the spectral bandwidth of the highest (trigonometric) component of the current. Four basis functions per arm reproduced their results exactly.

If the periodic surface of Fig. 5.11 is truncated to 15 elements wide, the effect on the reflection coefficient is shown in Fig 5.12. The reflection coefficient for the periodic surface is shown for comparison. Both results were computed using the same approximations: two trigonometric-type basis functions per arm plus the junction function, encircling that portion of the spectrum that was less than twice the spectral radius of the (trigonometric) basis functions.
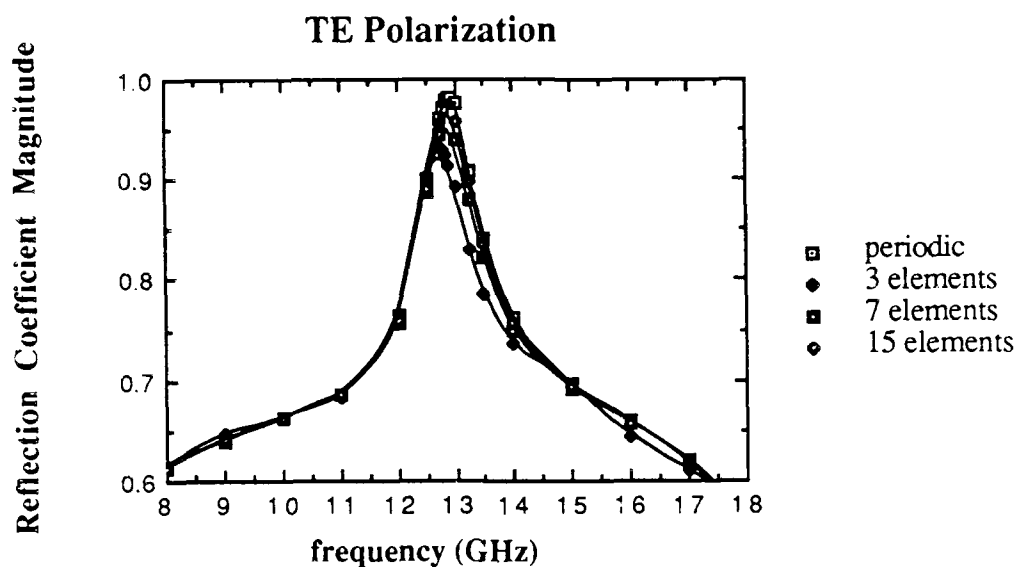
TE Polarization
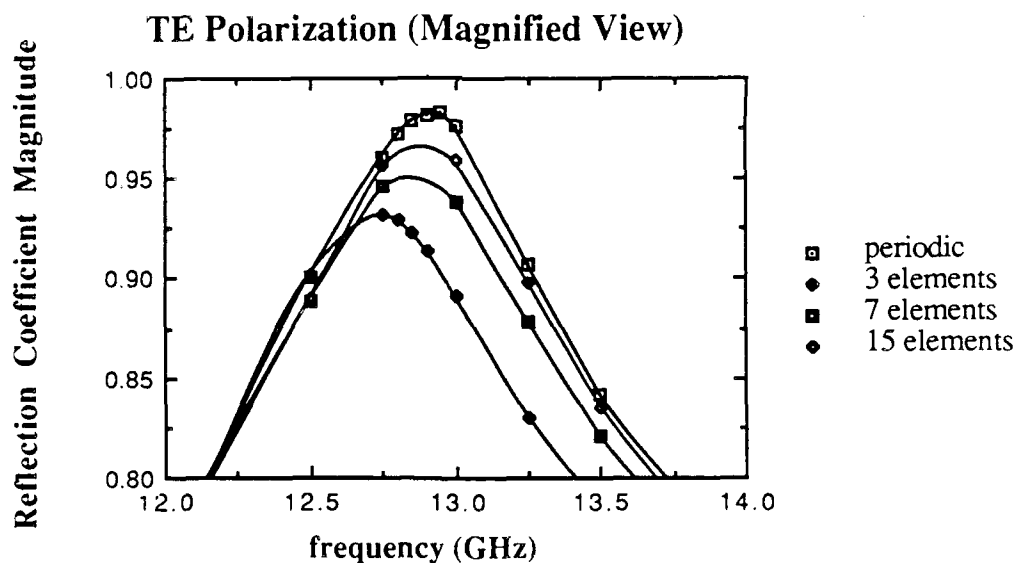

(a)

TE Polarization
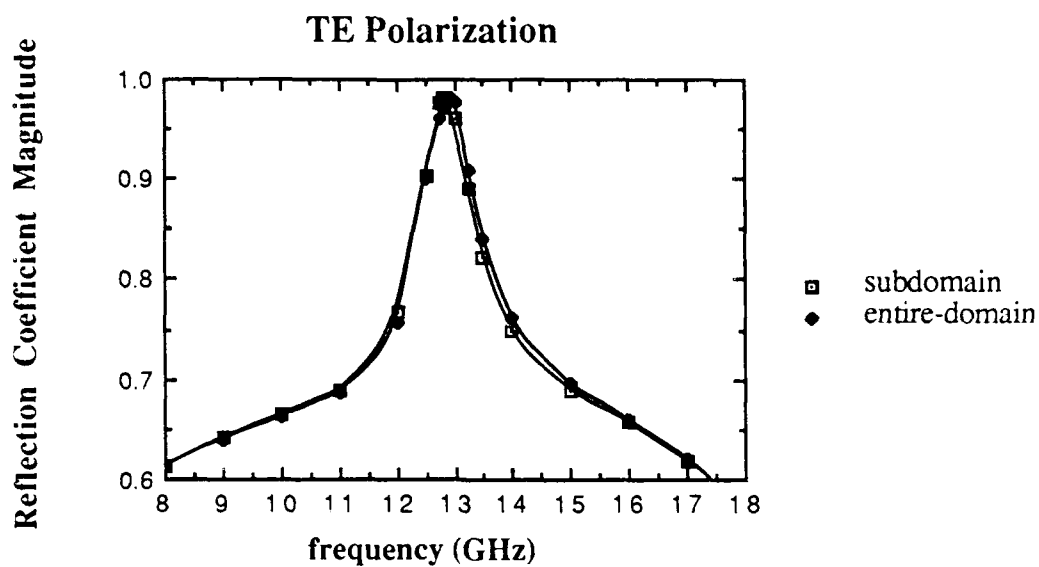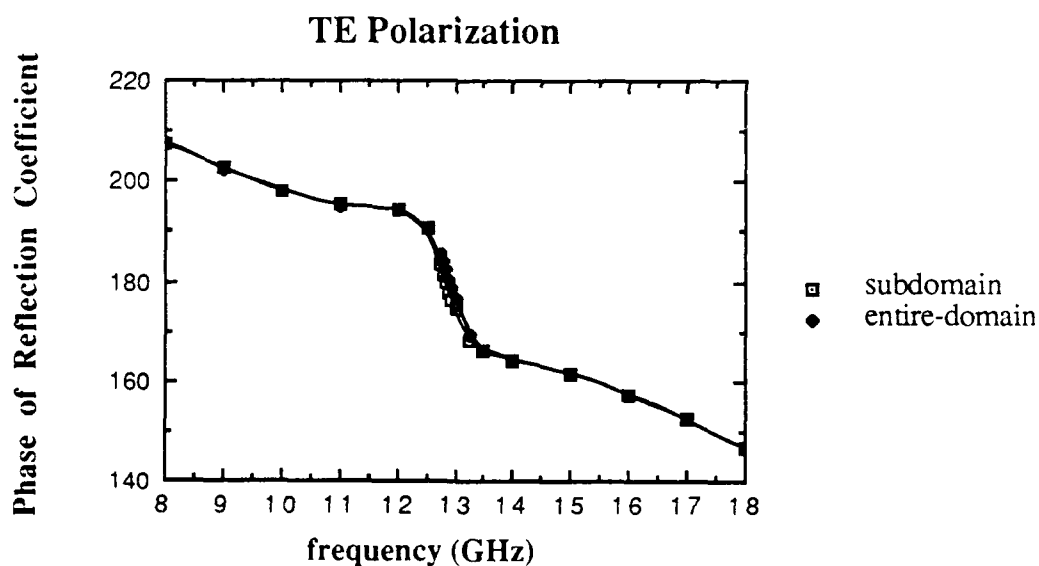
(b)

Figure 5.8. (a) Magnitude and (b) phase of the reflection coefficient for a periodic array of cross-shaped elements on a dielectric substrate, computed with two different sets of basis functions. $T_{\eta_1} = T_{\eta_2} = 1$ cm, $L = 0.6875$ cm, $W = 0.0625$ cm, $\Omega = 90$ deg, $(\theta_i, \varphi_i) = (0.1°, 0.1°)$.

TE Polarization


```
periodic
3 elements
7 elements
15 elements
```

(a)

TE Polarization (Magnified View)


```
periodic
3 elements
7 elements
15 elements
```

(b)

Figure 5.9. Computed values for the reflection coefficient for finite-width frequency selective surfaces of 3, 7, and 15 patches on a dielectric backing. Same element and lattice as in Fig. 5.8, TE polarization ($E^{inc} = \hat{y}E_y$), $(\theta_i, \varphi_i) = (0.1°, 0.1°)$: (a) frequency range 8-18 GHz, (b) 12-14 GHz.

TM Polarization

(a)

TM Polarization (Magnified View)

(b)
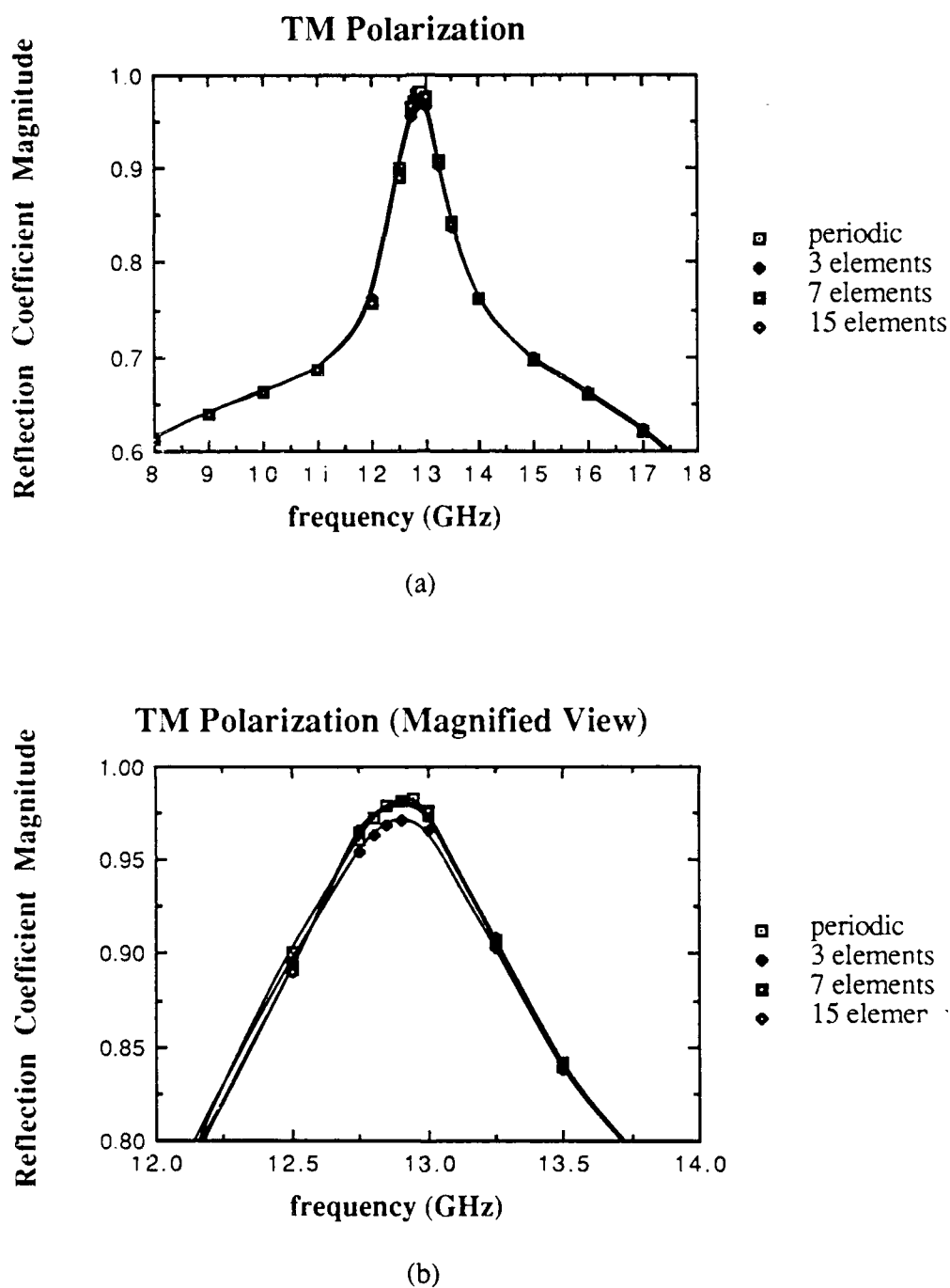
Figure 5.10. Computed v∼¹ues for the reflection coefficient for finite-width frequency selective surfaces of 3, 7, and 15 patches on a dielectric backing. Same element and lattice as in Fig. 5.8, TM polarization ($\mathbf{E}^{inc} = \hat{\mathbf{x}}E_x$), $(\theta_i, \varphi_i) = (0.1°, 0.1°)$: (a) frequency range 8-18 GHz, (b) 12-14 GHz.

TM Polarization
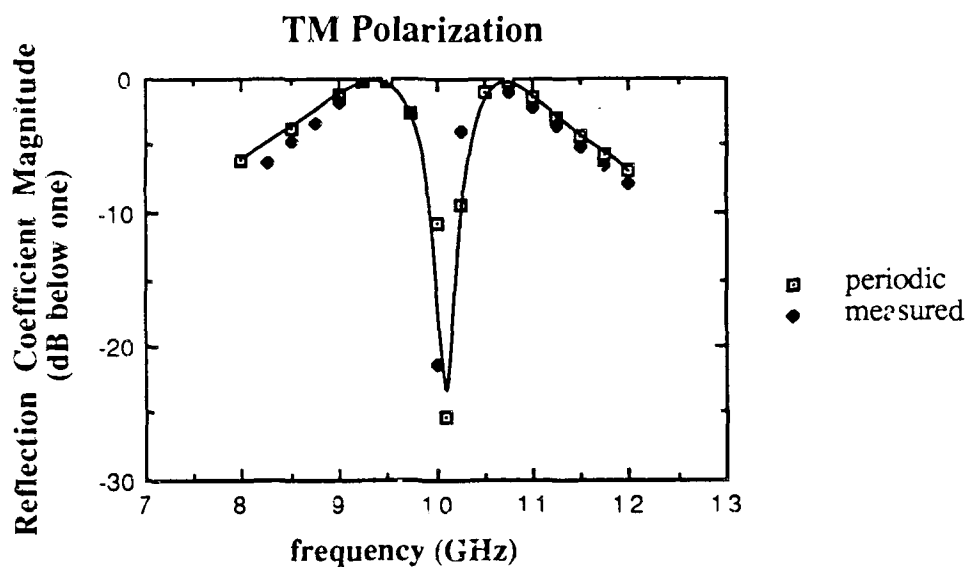
□ periodic
◆ measured

Figure 5.11. Comparison of computed and measured data for the frequency selective surface of Pelton and Munk [39]: periodic array, TM polarization ($\mathbf{E}^{inc} = \hat{\mathbf{x}}E_x$), ($\theta_i, \varphi_i$) = (30°, 0°).

TM Polarization

□ periodic
◆ 15 elements
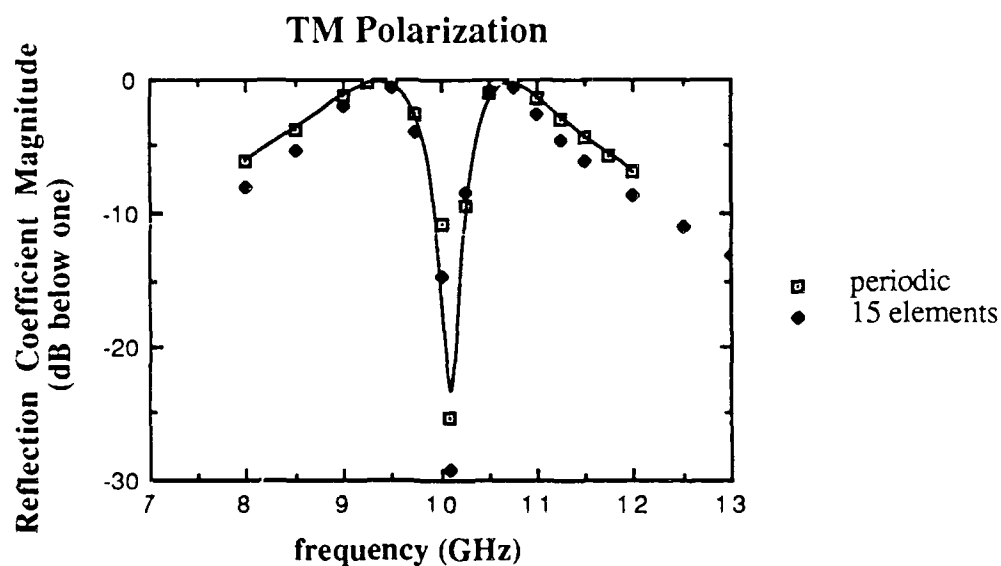
Figure 5.12. Computed reflection coefficients for a 15-element frequency selective surface of finite width and its periodic counterpart: TM polarization ($\mathbf{E}^{inc} = \hat{\mathbf{x}}E_x$), ($\theta_i, \varphi_i$) = (30°, 0°).

These results show the error in using the periodic approximation to predict electromagnetic scattering from a finite array of various sizes, when the frequency of the incident field is near the first resonance of the element. If a finite-width array is 15 patches wide, the error in the scattered field using the periodic approximation is on the order of two per cent. However, if the frequency is much lower than the first resonant frequency of the element, a low-frequency resonance can be excited on the array, as shown in Figs. 5.13 and 5.14, even when there is no direct electrical connection between the two edges. In both of these examples, the array is embedded between two identical dielectric layers of relative permittivity $4 - j.02$ and thickness $t = .5$ cm; In the first example, the array is exactly two wavelengths wide at the frequency of the incident field. The two-wavelength envelope is plainly visible in the magnitude plot. In the second example, the array is four wavelengths wide at the frequency of the incident field. Since the edge effect is not localized in this frequency range, approximating the fields from a periodic-array formulation would be significantly in error. Such models cannot predict the interaction of two edges, which is clearly present in Figs. 5.13 and 5.14.

None of the previous examples illustrate the versatility of the multilayer Green's function developed in Sec. 3.1. As a final example, sample results for a periodic surface embedded in a four-layer dielectric medium are presented. The geometry is shown in Fig. 5.15, which was described by Contu and Tascone [43]. The element is a crossed dipole, whose lattice and dimensions are given by $T_{\eta_1} = 0.65$ cm, $T_{\eta_2} = 0.46$ cm, $L = 0.555$ cm, $W = 0.015$ cm, $\Omega = 45$ deg, as defined in Fig. 5.7. The results are presented in terms of the magnitude of the reflection coefficient, which, for frequencies low enough that only one propagating mode exists in the free-space regions above and below the surface, can be accurately approximated by

$$|T_{00}^{TE}| = \sqrt{1 - (R_{00}^{TE})^2} \text{ , for TE incidence, and} \tag{5.27a}$$

$$|T_{00}^{TM}| = \sqrt{1 - (R_{00}^{TM})^2} \text{, for TM incidence.} \tag{5.27b}$$
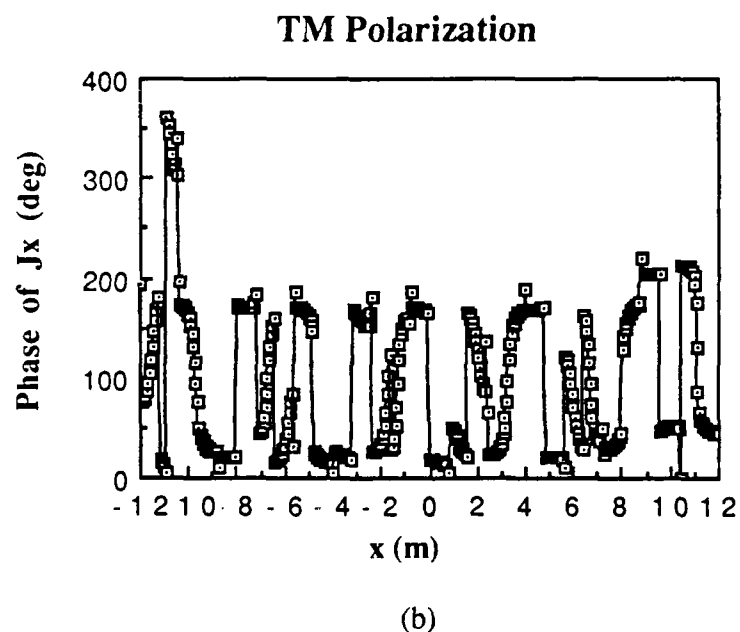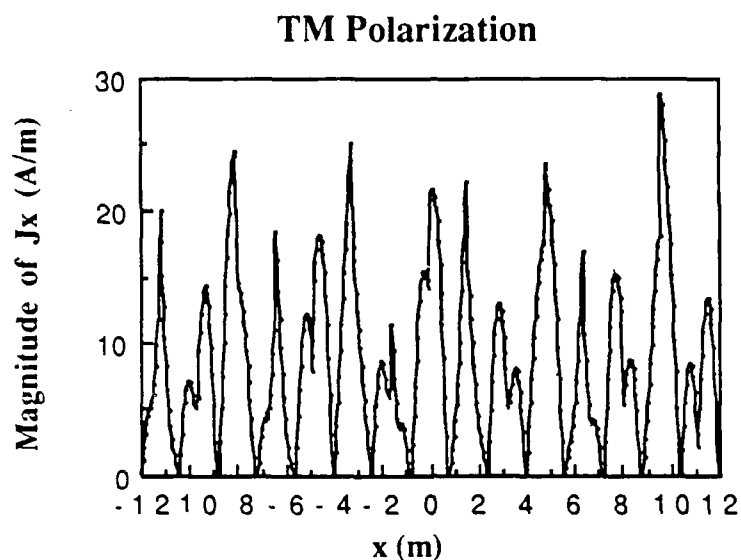
TM Polarization

(a)

TM Polarization
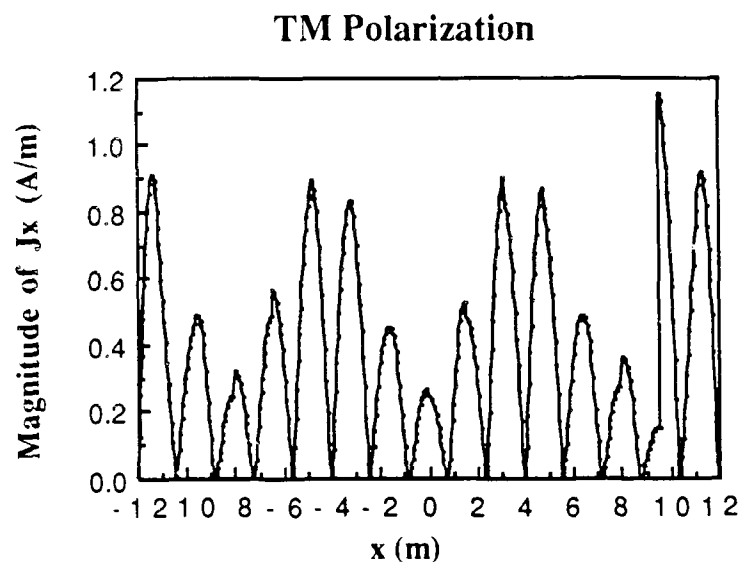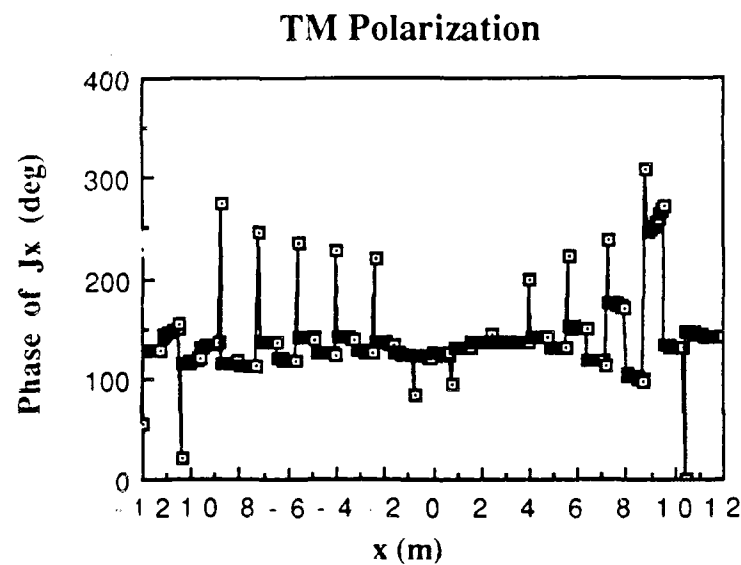
(b)

Figure 5.13. Low-frequency resonance on a finite array of 15 cross-shaped conducting patches embedded between two identical dielectric layers. $T_{\eta_1} = T_{\eta_2} = 1.6$ cm, $L = 1.51$ cm, $W = 0.044$ cm, $\Omega = 90$ deg, ε_{r_1}, $\varepsilon_{r_2} = 4 - j.02$, t_1, $t_2 = 0.5$ cm, frequency = 2.5 GHz, $(\theta_i, \varphi_i) = (1°, 1°)$: (a) magnitude, (b) phase.
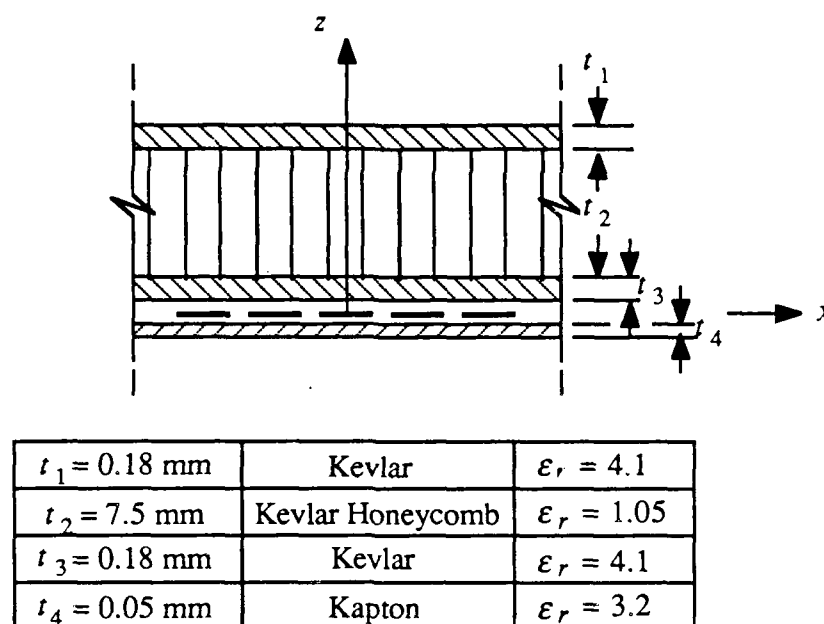
TM Polarization

(a)

TM Polarization

(b)

Figure 5.14. Low-frequency resonance on a finite array of 15 cross-shaped conducting patches embedded between two identical dielectric layers. $T_{\eta_1} = T_{\eta_2} = 1.6$ cm, $L = 1.51$ cm, $W = 0.044$ cm, Ω = 90 deg, ε_{r_1}, $\varepsilon_{r_2} = 4 - j.02$, t_1, $t_2 = 0.5$ cm, frequency = 5 GHz, $(\theta_i, \varphi_i) = (1°, 1°)$: (a) magnitude, (b) phase.

$t_1 = 0.18$ mm	Kevlar	$\varepsilon_r = 4.1$
$t_2 = 7.5$ mm	Kevlar Honeycomb	$\varepsilon_r = 1.05$
$t_3 = 0.18$ mm	Kevlar	$\varepsilon_r = 4.1$
$t_4 = 0.05$ mm	Kapton	$\varepsilon_r = 3.2$

Figure 5.15. Four-layer dielectric medium (Contu and Tascone [43]).

The numerical results of Fig. 5.16 were computed using four trigonometric-type basis functions on each of the two arms plus the junction function. For the interactions that do not involve the junction basis function, the inner products were evaluated by truncating the spectra at eight times the highest spectral bandwidth of the trigonometric basis functions. For those matrix elements that involve the junction basis function, the inner products were evaluated by summing out to sixteen times the highest spectral bandwidth of the trigonometric-type basis functions.

The discrepancy between the two results at higher frequencies can be reduced for the TE polarization by including more basis functions in the expansion of the unknown. However, this does not explain the discrepancy for the TM polarization, for which the addition of up to twenty basis functions per arm does not improve the agreement between the two results. The accuracy of these results has also been confirmed by an independent program using twenty rooftop basis functions per wavelength. The difference might be
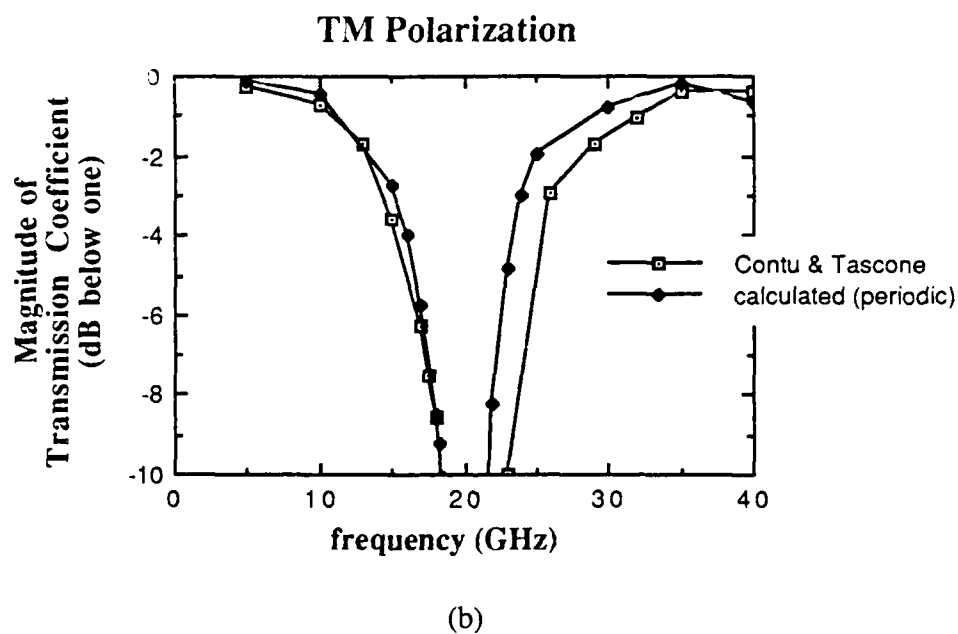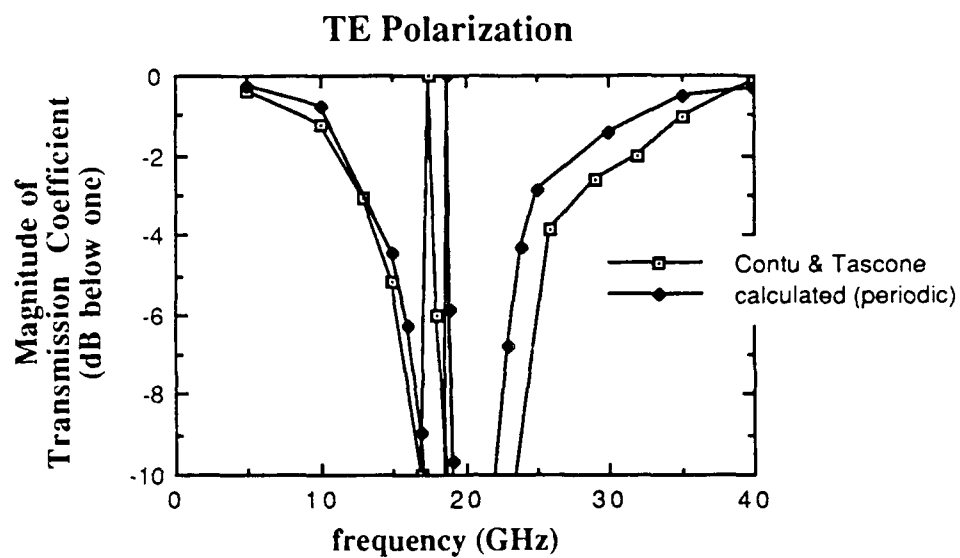
TE Polarization

(a)

TM Polarization

(b)

Figure 5.16. Computed values of the transmission coefficients for the geometry of Contu and Tascone [43]: $(\theta, \varphi) = (30°, 45°)$.

explained by one of the following facts. (1) Unlike the paper by Contu and Tascone, no attempt was made here to incorporate the edge singularity in the representation for the current. This is usually not a significant source of error for narrow elements. (2) Since Contu and Tascone have employed the scattering-matrix approach to incorporate the dielectric support, perhaps the difference can be blamed on the fact that typically a large number of Floquet space harmonics must be included in the scattering matrices as the layers become extremely thin, as they are in this example.

CHAPTER 6

ARBITRARY INCIDENCE AND NONUNiFORM ARRAYS

When a frequency selective surface is considered to be finite, the vector-Floquet nature of the fields vanishes, i.e., the scattered field is no longer a discrete spectrum of plane waves, regardless of the nature of the incident field. In this case, it is not necessary to restrict one's attention to plane-wave sources, or to truncated versions of periodic surfaces. Arbitrary incident fields can easily be treated in the context of finite arrays, and all of the tools that were developed to predict the currents on uniform finite arrays are directly applicable to nonuniform arrays. The designer is therefore capable of modeling the effects of varying the size and shape of the elements, as well as the array lattice, allowing more flexibility to achieve his design goals. The reasons for doing so will become apparent as we proceed.

For most of the unit cell geometries used in practice, the null frequencies in the reflection or transmission characteristics are very sensitive to the incident angles of the incident field. Since FSS structures are typically narrow band, it is essential that a surface be designed for the incident angles that exist in a given system. However, in numerous practical situations, the incident field is not a plane wave, and an entire range of incident angles exists at the surface of the array. This is the case, for example, when a frequency selective surface is in the Fresnel field of an electromagnetic horn. In this chapter, the effects of a non-plane-wave source will be modeled using a very simple and natural extension of the plane-wave situation, demonstrating that a serious degradation in performance results when a realistic source is used. A method is proposed to compensate

for the effects of non-plane-wave illumination by tapering the geometry of the surface across the array.

The problem that will be considered is a dichroic subreflector in an offset configuration. Because of their ease of manufacture and analytical treatment, planar, rather than hyperbolic, surfaces are often used in this application. In order to isolate the significant variables and to reduce the problem to a manageable size, the analysis is performed for a frequency selective surface of finite width, permitting the incident field to vary in a non-plane-wave fashion only along the finite dimension of the array. The x variation of the field is arbitrary, but the y variation is assumed to be the phase dependence associated with a uniform plane wave. The geometry is illustrated in Fig. 6.1. In this case, the source is close enough to the array that the incident field cannot be considered a plane wave.
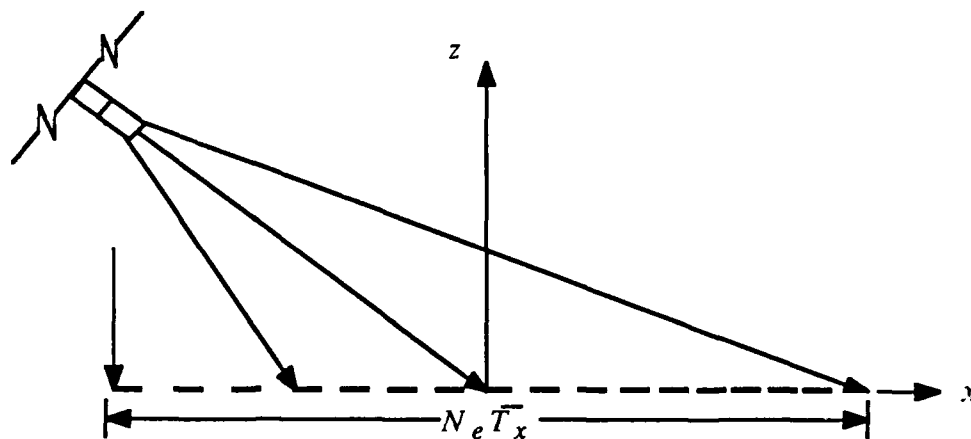
Figure 6.1. A finite-width, free-standing array of y-directed thin dipoles illuminated by an electromagnetic horn.

The application of the spectral-Galerkin technique results in a matrix equation of the form,

$$\frac{-1}{2\pi T_{\eta_2}\sin\Omega}\sum_{j=1}^{I}c_j\sum_{n=-\infty}^{\infty}\int_{-\infty}^{\infty}\tilde{j}_i^{\dagger}(\alpha,\beta_n)\,\tilde{G}(\alpha,\beta_n)\,\tilde{j}_j(\alpha,\beta_n)d\alpha$$

$$=\int_{-\infty}^{\infty}\int_{-\infty}^{\infty}j_i^{\dagger}(x,y)\,E^{inc}(x,y)\,dxdy\,,\quad i=1,2,...,I\,.\quad(6.1)$$

For plane-wave excitation, the kernel of the double integral on the right-hand side of Eq. (6.1) is of Fourier-transform type, which allows the integrations to be carried out analytically (cf. Sec. 3.5). This prompts us to write an arbitrary field in terms of a Fourier series, which, for the one-dimensional case of interest to us, takes the form

$$E_t^{inc}(x,y)=e^{jk_y y}\sum_{m=-M}^{M}e_m\,e^{jk_{xm}x},\quad k_{xm}=\frac{2\pi m}{N_e\overline{T}_x}\,,\quad(6.2)$$

where N_e is the number of elements, $\overline{T}_x$ is the average period along the x axis, and $N_e\overline{T}_x$ is the width of the array. The vector constants e_m are determined in the usual manner by multiplying both sides of Eq. (6.2) by the complex conjugate of the exponential term and integrating over the width, which may be done for all e_m in parallel via the fast Fourier transform. When this representation is substituted for the incident field, the two-dimensional integrations on the right can be done analytically, as before, resulting in a simple series expression for the right-hand side. It should be emphasized that the numerically-intensive process of filling the moment-method matrix is done only once, and the resultant system of equations is solved using a composite right-hand side.

In order to determine the effect of non-plane-wave incidence on the scattered field, the reflection coefficient is defined as the far-zone scattered electric field in the specular direction due to a unit row of dipoles, normalized with respect to the physical optics scattering of a perfectly conducting sheet of the same physical area. Since the incident field has been decomposed into a spectrum of plane waves according to Eq. (6.2), the calculation is easily performed. As in the periodic case, the magnitude of the reflection coefficient reaches a maximum of 1.0 at the element resonances.

As an example, the x variation of the incident field is assumed to be the H-plane cut of the far-field pattern of an E-plane sectoral horn. It is important that the reader realize that the far-field pattern was chosen only for convenience in order to give a realistic model for the magnitude and phase distribution of the incident field on the array. The horn model is described by Balanis [44], in which the magnitude distribution of the fields at the mouth of the horn is assumed to be the same as the distribution for the dominant TE_{10} mode in the feed waveguide, and the phase distribution is assumed to be the phase distribution of a cylindrical wave emanating from the apex of the horn (see Fig. 6.2). The far-field pattern of this aperture field is computed using standard techniques, where the integrals are evaluated in terms of cosine and sine Fresnel integrals.
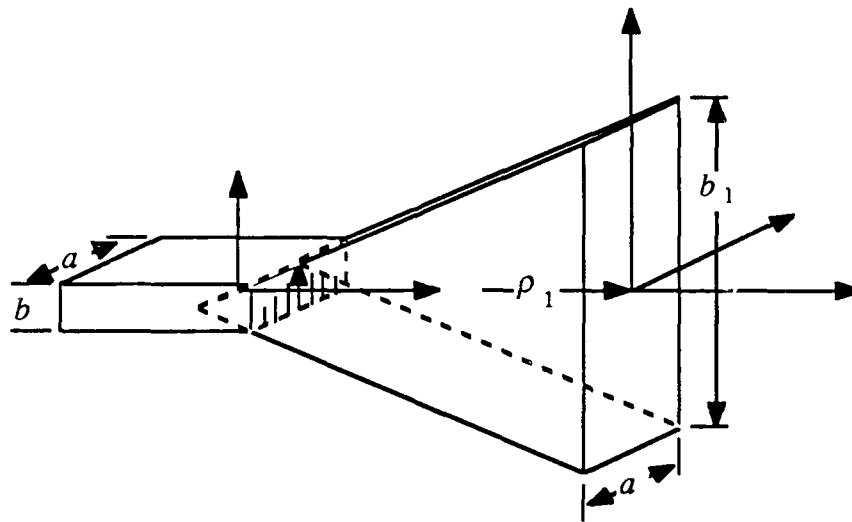

Figure 6.2. E-plane horn.

The frequency selective surface chosen for the numerical study is a finite-width version of the periodic surface described by Ott et al. [37]. The unit cell is defined in Fig. 6.3, where $T_x = T_y = 1.78$ cm, $L = 1.27$ cm, $W = 0.127$ cm, $\Omega = 90$ deg Fifteen y-directed thin dipoles are assembled along the x axis and then replicated in a periodic
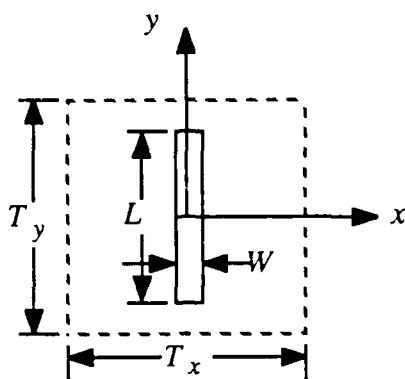
Figure 6.3. Unit cell in a dipole array.

fashion along the positive and negative y axes to generate the complete surface. The elements are assumed to be thin enough that the transverse current on each element (i.e., J_x) is negligible, as well as the x variation of J_y. As a result, the operator is discretized using rooftop basis functions and Galerkin testing.

The dimensions of the horn are $a = 0.5\lambda$, $b = 0.25\lambda$, $b_1 = 2.75\lambda$, $\rho_1 = 6.0\lambda$ at 10 GHz, which are held fixed as the frequency is varied. The phase center of the horn is located along the radial line $(\theta, \varphi) = (30°, 180°)$, at a range of 26.7 cm from the origin, as defined in Fig. 6.1, and is oriented so that the incident field is parallel to the elements. For these dimensions, the effective incident angles are $\theta = 0°$ at the left edge, $\theta = 30°$ at the origin, and $\theta = 49.1°$ at the extreme right edge of the array. A plot of the incident field distribution along the x axis (magnitude and phase) is shown in Fig. 6.4, at a frequency of 10 GHz, and assuming $k_y = 0$. The maximum field intensity occurs at a point which is midway between the left edge, where the horn is closest to the array, and the origin, which is along the maximum of the horn's field pattern. The change in slope of the phase plot is due to the change in effective incident angle on the array.

The power reflection coefficient for a 15-element array illuminated by this incident field is shown in Fig. 6.5. Also shown is the reflection curve for a periodic surface illuminated by a plane-wave field incident from $(\theta, \varphi) = (30°, 180°)$.

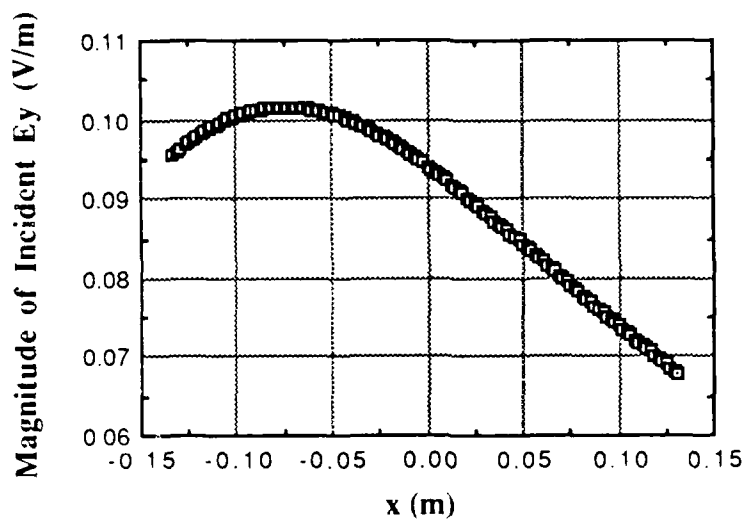Figure 6.4 (a). Magnitude distribution of the incident field on a finite-width array: frequency = 10 GHz, (θ,φ) = (30°, 180°), range = 26.7 cm, $k_y = 0$.
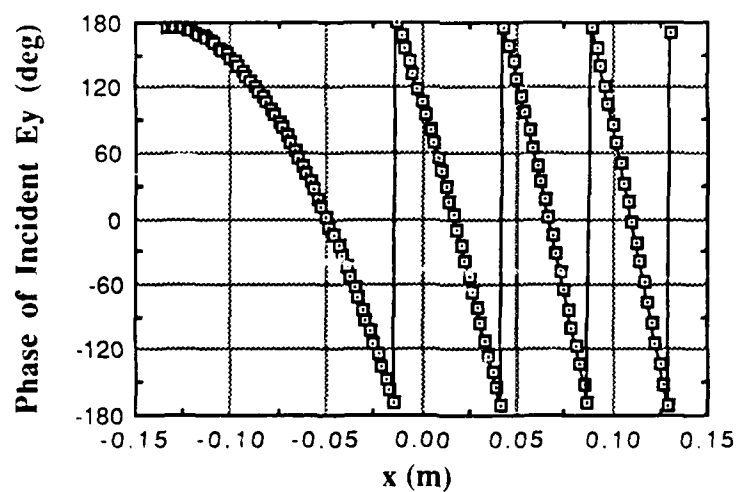

Figure 6.4 (b). Phase distribution of the incident field across a finite-width array: frequency = 10 GHz, (θ,φ) = (30°,180°), range = 26.7 cm, $k_y = 0$.
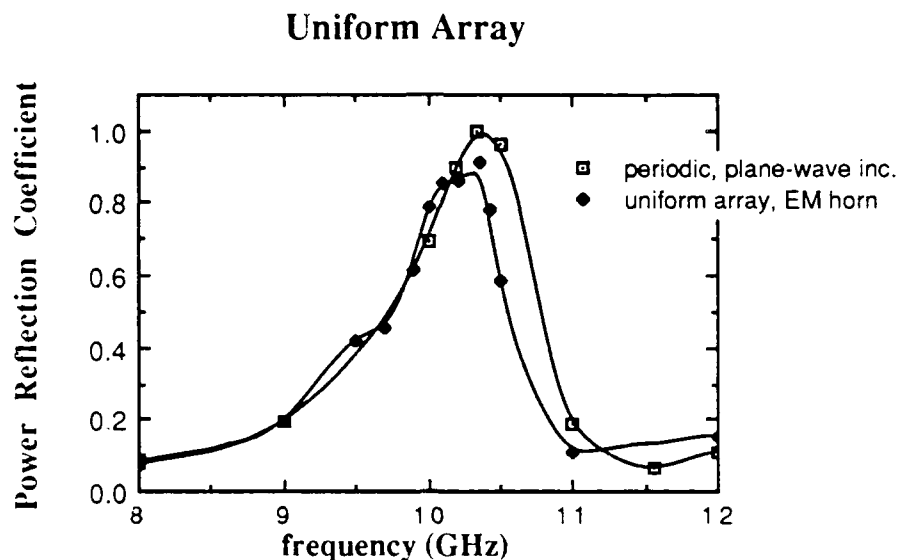
Uniform Array

Figure 6.5. Power reflection coefficient versus frequency: plane-wave
scattering from a periodic surface, and scattering from a
tapered finite-width FSS of 15 elements due to an incident
field that varies as the H-plane cut of an E-plane sectoral horn.

As is evident from the figure, non-plane-wave illumination of the surface causes significant
distortion in its reflection curve. About ten per cent of the available power is lost at
resonance and about 20 per cent of the bandwidth.

The source of the problem appears to be the change in effective illumination angle on
the array. Figure 6.6 is a plot of the resonant frequency versus incident angle for the
element used in this example. The resonant frequency shifts from 11.2 GHz at $\theta = 0°$ to
9.25 GHz at $\theta = 50°$. Since the half-power bandwidth of the stop band is 1 GHz at $\theta =$
30°, a 2-GHz shift in the resonant frequency over the range of incident angles on the array
causes serious distortion in the frequency response. Locally, each dipole is resonating at a
different frequency, due to the different effective incident angles at each point on the array.

As a remedy, the idea is to design each cell as though it were the unit cell of a periodic
surface illuminated by a plane wave at the effective incident angle seen by that particular
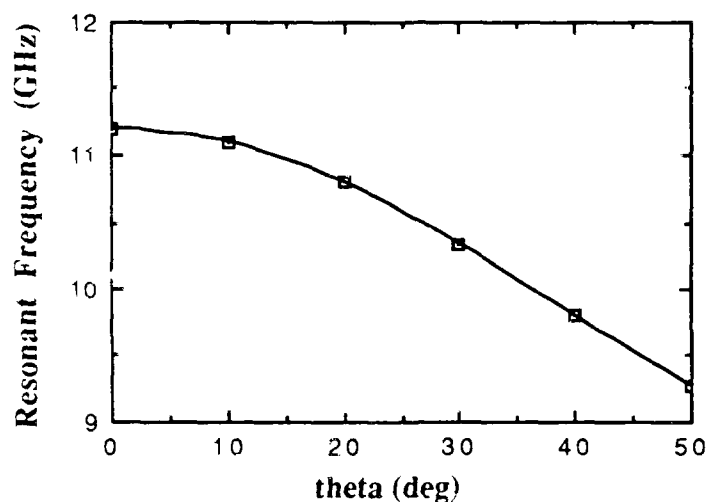
Figure 6.6. Shift in resonant frequency for the element of Ott et al. [37].

cell. In the 15-element example, unit cells are designed for 15 periodic surfaces illuminated by plane waves at 15 different incident angles, such that they all resonate at the same center frequency. The 15 unit cells obtained in this manner are assembled to construct the 15-element array, and the result is tested in a finite frequency selective surface. In the design stage, however, only the horizontal cell sizes and element lengths are permitted to vary, while the vertical cell size T_y and element width are held constant.

In designing the 15 cells that compose the finite array, two methods were used. A design frequency is chosen, at which all of the elements of the finite array were to become resonant. In the first method, both the lengths and spacings of the elements were scaled by the ratio of the design frequency and the resonant frequency at the dipole's effective illumination angle. In the second method, only the spacings between the elements were adjusted, according to the above ratio, leaving the lengths fixed. After assembling the 15 unit cells obtained in this manner and computing their frequency response in the finite array, the second method was found to give somewhat better performance than the first method, and its reflection curve is shown in Fig. 6.7. Hence, as a result of tapering the

surface geometry, all of the power is reflected at resonance as before, leaving only a slight

reduction in bandwidth, which may be recoverable through further optimization.
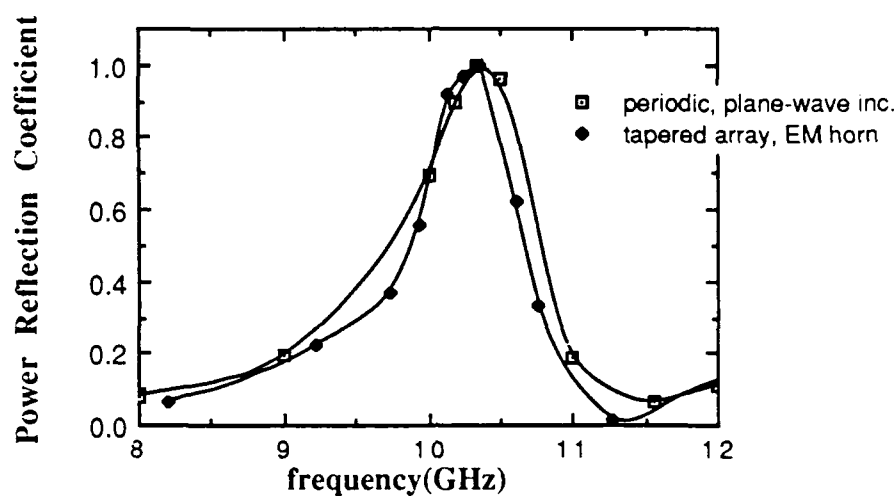
Nonuniform Array

Figure 6.7. Power reflection coefficient versus frequency: plane-wave
scattering from a periodic surface, and scattering from a
tapered finite-width FSS of 15 elements due to the
electromagnetic-horn incident field.

CHAPTER 7

CONCLUSIONS AND SUGGESTIONS FOR FUTURE WORK

The analysis of finite frequency selective surfaces is still in its infancy: this thesis is the result of one of the first attempts at modeling finite arrays. In it, the formulation of the scattering problem in the spectral domain has been presented, the essential considerations involved in implementing the spectral-Galerkin equation have been discussed, and a few selected geometries have been analyzed to illustrate the conclusions. Motivated by existing applications, numerical modeling of generalized sources and nonuniform frequency selective surfaces has also been done.

The effects of finite dimensions on the performance of frequency selective surfaces have been classified into two frequency regimes. At frequencies near the first resonance of the element, the edge effect is localized and extends from three to seven cells toward the center of the array. Sample calculations show that the component of the current flowing perpendicularly to the polarization of the incident field is significantly enhanced near the edges; however, for more than 15 elements, the periodic approximation gives about two per cent accuracy in the scattered fields. At lower frequencies, an edge-to-edge resonance can be excited on the array, even when there is no direct electrical connection between the two edges. In this regime, the edge effect is obviously not localized, and it would be impossible to accurately predict the scattered fields from such a surface using infinite models.

In Chapter 6, it was shown that the use of a realistic source model, such as the near field of an electromagnetic horn, caused serious degradation in the frequency response of a particular finite frequency selective surface. Since the resonant frequency of most

frequency selective surfaces is strongly influenced by incident angles, it was postulated that the poor performance was due to the presence of a wide range of effective incident angles on the array. A method was therefore suggested to continuously vary the lattice of the array in order to force all of the elements to resonate simultaneously at a given frequency. Based on this theory, a nonuniform frequency selective surface was designed and modeled in the presence of the horn, and it was shown that continuously varying the surface geometry was an effective means of alleviating the distortion.

Looking ahead to possible areas of research in frequency selective surfaces, it is appropriate to mention first of all that this is not the last word in finite frequency selective surfaces. Because of the large amounts of computer time required for some geometries and limitations in computer storage, the two-dimensional examples were limited to certain thin-patch geometries that could be analyzed with a small number of unknowns. The next generation of computers will make many of the assumptions used here unnecessary. Furthermore, all of the results presented in the thesis were generated with special-purpose routines. A general-purpose program capable of modeling arbitrary finite frequency selective surfaces with arbitrary incident fields would be a valuable contribution.

The simplifications and restrictions imposed at the beginning suggest other possible areas of research. Many applications that require wider frequency bandwidths will need to incorporate two or more printed surfaces to meet those requirements. While this problem has been solved satisfactorily for periodic surfaces, numerical modeling of multiple layers of finite frequency selective surfaces has never been attempted. Computation time and storage requirements increase in proportion to the number of layers squared, if the multilayered problem is solved at once. However, a procedure analogous to the scattering matrix approach for periodic surfaces would reduce the demands on computer resources.

A second area of research is suggested by the fact that in this work, only the printed surface was assumed to be finite in some sense, while the surrounding medium was assumed to be an infinite medium of uniform homogeneous dielectric layers. This made it

possible to derive the analytical Green's functions. If the guided modes in the dielectric wave guide carry sufficient energy, particularly for oblique incidence, then truncating the dielectric may have a significant effect on the scattered fields. How much effect, or under what conditions this effect may be substantial, is not known. Incorporating the effects of a finite dielectric slab will involve the equivalent of discretizing the polarization current in the dielectric medium and solving simultaneously for this current and the conduction current on the printed surface. Some of this work has already begun at the University of Illinois by considering a finite number of infinite strips embedded in an infinite dielectric cylinder of rectangular cross section.

A third area of research is that of curved surfaces. A natural starting place would be the development of a formal notation capable of describing the shape, position, orientation, and curvature of an element in three-dimensional space, much like the notation used in the geometrical theory of diffraction. Such a formalism might also be applied to other deterministic scattering problems as well.

Finally, a fourth area of research that could be carried out in the context of periodic surfaces is the development of a systematic design procedure. Most, if not all, of the programs used in practice are analysis tools. The designer is given a set of specifications, and then, based on his experience, he analyzes tens or hundreds of cases to find one that comes close to meeting the specifications. Depending on his level of expertise, this process could be very time-consuming – and the intuition he gains is not easily passed on to his colleagues.

The alternative would be to automate this procedure in an optimization program. The inputs to the program would be the design specifications: resonant frequency, bandwidth, polarization of the field (linear or circular), etc. Beginning at an initial design, the program would be designed to incrementally vary the adjustable parameters of the surface until the design goals were achieved. The output of the program would be the number of

conducting layers, the lattice, the shapes and sizes of the elements, and the thicknesses and permittivities of the dielectric layers.

Predicting the future is a tricky business, but the problems discussed here are potentially interesting and are motivated by real applications in existing or proposed systems.

LIST OF REFERENCES

[1] D. Rittenhouse, "An optical problem, proposed by Mr. Hopkinson, and solved by Mr Rittenhouse," *Trans. Amer. Phil. Soc.,* vol. 2, pp. 201-206, 1786.

[2] T. A. Cwik, "Scattering from general periodic screens," Ph.D. dissertation, University of Illinois, Urbana, Illinois, 1986.

[3] T. Larson, "A survey of the theory of wire grids," *IRE Trans. Microwave Theory Tech.,* pp. 191-201, May 1962.

[4] R. Mittra, C. H. Chan, and T. A. Cwik, "Techniques for analyzing frequency selective surfaces–A review," *Proc. IEEE,* vol. 76, no. 12, pp. 1593-1615, December 1988.

[5] J. P. Montgomery, "Scattering by an infinite periodic array of thin conductors on a dielectric sheet," *IEEE Trans. Antennas Propag.,* vol. AP-23, no. 1, pp. 70-75, January 1975.

[6] C. C. Chen, "Scattering by a two-dimensional periodic array of conducting plates," *IEEE Trans. Antennas Propag.,* vol. AP-18, no. 5, pp. 660-665, September 1970.

[7] C. C. Chen, "Transmission through a conducting screen perforated periodically with apertures," *IEEE Trans. Microwave Theory Tech.,* vol. MTT-18, no. 9, pp. 627-632, September 1970.

[8] C. H. Tsao and R. Mittra, "Spectral-domain analysis of frequency selective surfaces comprised of periodic arrays of cross dipoled and Jerusalem crosses," *IEEE Trans. Antennas Propag.,* vol. AP-32, no. 5, pp. 478-486, May 1984.

[9] T. A. Cwik and R. Mittra, "The effects of the truncation and curvature of periodic surfaces: A strip grating," *IEEE Trans. Antennas Propag.,* vol. AP-36, no. 5, pp. 612-622, May 1988.

[10] L. A. Weinstein, *The Theory of Diffraction and the Factorization Method.* Boulder, CO: Golem Press, 1969, pp. 267-281.

[11] T. K. Wu, "Analysis and application of multilayered periodic strips," *AEU,* vol. 33, no. 4, pp. 144-148, 1979.

[12] R. C. Hall and R. Mittra, "Scattering from a periodic array of resistive strips," *IEEE Trans. Antennas Propag.,* vol. AP-33, no. 9, pp. 1009-1011, September 1985.

[13] A. Papoulis, *The Fourier Integral and Its Applications.* New York: McGraw-Hill, 1962, pp. 42-48, 278.

[14] P. Bielli, S. Contu, D. Savini, A. Saitto, and R. Tascone, "Design and measurement of frequency selective surfaces," *CSELT Rapporti Tecnici,* vol. xi, no. 5, pp. 327-331, October 1983.

[15] T. A. Cwik and R. Mittra, "The cascade connection of planar periodic surfaces and lossy dielectric layers to form an arbitrary periodic screen," *IEEE Trans. Antennas Propag.*, vol. AP-35. no. 12, pp. 1397-1405, December 1987. Correction, *IEEE Trans. Antennas Propag.*, vol. AP-36. no. 9, September 1988.

[16] S. Contu and R. Tascone, "Scattering matrix of passive arrays in a stratified dielectric," *CSELT Rapporti Tecnici*, vol. xi, no. 6, pp. 361-364, December 1983.

[17] V. D. Agrawal and W. A. Imbriale, "Design of a dichroic Cassegrain subreflector," *IEEE Trans. Antennas Propag.*, vol. AP-27, no. 4, pp. 466-473, July 1979.

[18] T. Itoh, "Spectral domain immitance approach for dispersion characteristics of generalized printed transmission lines," *IEEE Trans. Microwave Theory Tech.*, vol. MTT-28, no. 7, pp. 733-736, July 1980.

[19] Y. T. Lo, unpublished class notes, University of Illinois, Urbana, IL.

[20] D. R. Tanner, "Numerical methods for the electromagnetic modeling of microstrip antennas and feed systems," Ph.D. dissertation, University of Illinois, Urbana, Illinois, 1988.

[21] R. Orta, R. Tascone, and R. Zich, "A unified formulation for the analysis of general frequency selective surfaces," *Electromagnetics*, vol. 5, pp. 307-329, 1985.

[22] R. F. Harrington, *Field Computation by Moment Methods*. Malabar, FL: Krieger, 1968, pp. 2-9.

[23] N. Amitay and V. Galindo, "On energy conservation and the method of moments in scattering problems," *IEEE Trans. Antennas Propag.*, vol. AP-17, no. 6, pp. 747-751, November 1969.

[24] R. F. Harrington, *Time-Harmonic Electromagnetic Fields*. New York: McGraw-Hill, 1961, pp. 129-132.

[25] W. C. Chew, private communication.

[26] J. A. Kong and L. C. Shen, "Field of an antenna submerged in a dissipative dielectric medium," *IEEE Trans. Antennas Propag.*, vol. AP-25, no. 6, pp. 887-889, November 1977.

[27] P. J. Davis and P. Rabinowitz, *Methods of Numerical Integration*. New York: Academic Press, 1975, pp. 144-146, 315-344.

[28] K. E. Hillstrom, "Comparison of several adaptive Newton-Cotes quadrature routines in evaluating definite integrals with peaked integrands," *CACM*, vol. 13, no. 6, pp. 362-365, June 1970.

[29] H. Margenau and G. M. Murphy, *The Mathematics of Physics and Chemistry*, *2nd ed.* Princeton, NJ: Van Nostrand, 1956, pp. 473-482.

[30] M. Abramowitz and I. A. Stegun, *Handbook of Mathematical Functions*. Washington, DC: National Bureau of Standards, second printing, 1964, pp. 885-888, 916-919.

[31] R. K. Chugh and L. Shafai, "Comparison of Romberg and Gauss methods for numerical evaluation of two-dimensional phase integrals," *IEEE Trans. Antennas Propag.*, vol. AP-25, no. 4, pp. 581-583, July 1977.

[32] D. M. Pozar, "Analysis of finite phased arrays of printed dipoles," *IEEE Trans Antennas Propag.*, vol. AP-33, no. 5, pp. 1045-1053, October 1985.

[33] W. L. Ko and R. Mittra, "Scattering by a truncated periodic array," *IEEE Trans. Antennas Propag.*, vol. AP-36, no. 2, pp. 496-503, April 1988.

[34] W. Magnus, F. Oberhettinger, and R. P. Soni, *Formulas and Theorems for the Special Functions of Mathematical Physics*. New York: Springer-Verlag, 1966, pp. 429-435.

[35] C. C. Liu, J. Shmoys, A. Hessel, J. D. Hanfling, and J. M. Usoff, "Plane wave reflection from microstrip-patch arrays – theory and experiment," *IEEE Trans. Antennas Propag.*, vol. AP-33, no. 4, pp. 426-435, April 1985.

[36] N. Shuley, "A note on relative convergence for moment-method solutions of integral equations of the first kind as applied to dichroic problems," *Electron. Lett.*, vol. 21, no. 3, pp. 95-97, 1985.

[37] R. H. Ott, R. G. Kouyoumjian, and L. Peters, Jr., "Scattering by a two-dimensional periodic array of narrow plates," *Radio Sci.*, vol. 2, no. 11, pp. 1347-1359, November, 1967

[38] G. H. Schennum, "Frequency-selective surfaces for multiple-frequency antennas," *Microwave J.*, pp. 55-57, May 1973.

[39] E. L. Pelton and B. A. Munk, "Scattering from periodic arrays of crossed dipoles," *IEEE Trans. Antennas Propag.*, vol. AP-27, no. 3, pp. 323-330, May 1979.

[40] M. P. Hurst, "A method for analyzing frequency selective surfaces with elements of arbitrary shape," *1985 AP-S Int. Symposium Digest,* Vancouver, vol. II, pp. 655-657, June 1985.

[41] R. W. P. King, "Currents induced in a wire cross by a plane wave incident at an angle," *IEEE Trans. Antennas Propag.*, vol. AP-25, no. 6, pp. 775-781, November 1977.

[42] R. Jorgenson, private communication.

[43] S. Contu and R. Tascone, "Scattering from passive arrays in plane stratified regions," *Electromagnetics,* vol. 5, pp. 285-306, 1985.

[44] C. A. Balanis, *Antenna Theory: Analysis and Design*. New York: Harper & Row, 1982, pp. 532-550.